Chapter 1
Planet Formation: Key Mechanisms and Global Models

Sean N. Raymond and Alessandro Morbidelli

Abstract Models of planet formation are built on underlying physical processes. In order to make sense of the origin of the planets we must first understand the origin of their building blocks. This review comes in two parts. The first part presents a detailed description of six key mechanisms of planet formation:

- The structure and evolution of protoplanetary disks
- The formation of planetesimals
- Accretion of protoplanets
- Orbital migration of growing planets
- Gas accretion and giant planet migration
- Resonance trapping during planet migration.

While this is not a comprehensive list, it includes processes for which our understanding has changed in recent years or for which key uncertainties remain. The second part of this review shows how global models are built out of planet formation processes. We present global models to explain different populations of known planetary systems, including close-in small/low-mass planets (i.e., *super-Earths*), giant exoplanets, and the Solar System's planets. We discuss the different sources of water on rocky exoplanets, and use cosmochemical measurements to constrain the origin of Earth's water. We point out the successes and failings of different models and how they may be falsified. Finally, we lay out a path for the future trajectory of planet formation studies.

S. N. Raymond (✉)
Laboratoire d'Astrophysique de Bordeaux, CNRS and Université de Bordeaux, Pessac, France

A. Morbidelli
Laboratoire Lagrange, Observatoire de la Cote d'Azur, Nice, France
e-mail: morby@oca.eu

K. Biazzo et al. (eds.), *Demographics of Exoplanetary Systems*,
Astrophysics and Space Science Library 466,
https://doi.org/10.1007/978-3-030-88124-5_1

1.1 Observational Constraints on Planet Formation Models

If planet building is akin to cooking, then a review of planet formation is a cookbook. Planetary systems—like dishes—come in many shapes and sizes. Just as one cooking method cannot produce all foods, a single growth history cannot explain all planets. While the diversity of dishes reflects a range of cooking techniques and tools, they are all drawn from a common set of cooking methods. Likewise, the diversity of planetary systems can be explained by different combinations of processes drawn from a common set of physical mechanisms. Our goal in this review is first to describe the key processes of planet formation and then to show how they may be combined to generate global models, or recipes, for different types of planetary systems.

To illustrate the processes involved, Fig. 1.1 shows a cartoon picture of our current vision for the growth of Earth and Jupiter. Both planets are thought to have formed from planetesimals in different parts of the Solar System. In our current understanding, the growth tracks of these planets diverge during the pebble accretion process, which is likely to be much more efficient past the snow line (Lambrechts and Johansen 2014; Morbidelli et al. 2015). There exists a much larger diversity of planets than just Jupiter and Earth, and many vital processes are not included in the figure, yet it serves to illustrate how divergent formation pathways can contribute to planetary diversity.

We start this review by summarizing the key constraints on planet formation models. Constraints come from Solar System measurements (e.g., meteorites), observations of other planetary systems (e.g., exoplanets and protoplanetary disks), as well as laboratory measurements (e.g., to measure the sticking properties of small grains).

Solar System Constraints

Centuries of human observation have generated a census of the Solar System, albeit one that is still not 100% complete. The most important constraints for planet formation include our system's orbital architecture as well as compositional and timing information gleaned from in-situ measurements. An important but challenging exercise is to distill the multitude of existing constraints into just a few large-scale factors to which resolution-limited models can be compared.

The central Solar System constraints are:

- **The masses and orbits of the terrestrial planets**.[1]. The key quantities include their number, their absolute masses and mass ratios, and their low-eccentricity, low-inclination orbits. These have been quantified in studies that attempted to match their orbital distribution. For example the normalized angular momentum deficit AMD is defined as (Laskar 1997; Chambers 2001):

$$AMD = \frac{\sum_j m_j \sqrt{a_j} \left(1 - \cos(i_j)\sqrt{1 - e_j^2}\right)}{\sum_j m_j \sqrt{a_j}}, \tag{1.1}$$

[1] The terms "terrestrial" and "rocky" planet are interchangeable: the Solar System community generally uses the term *terrestrial* and the exoplanet community uses *rocky* We use both terminologies in this review to represent planets with solid surfaces that are dominated (by mass) by rock and iron

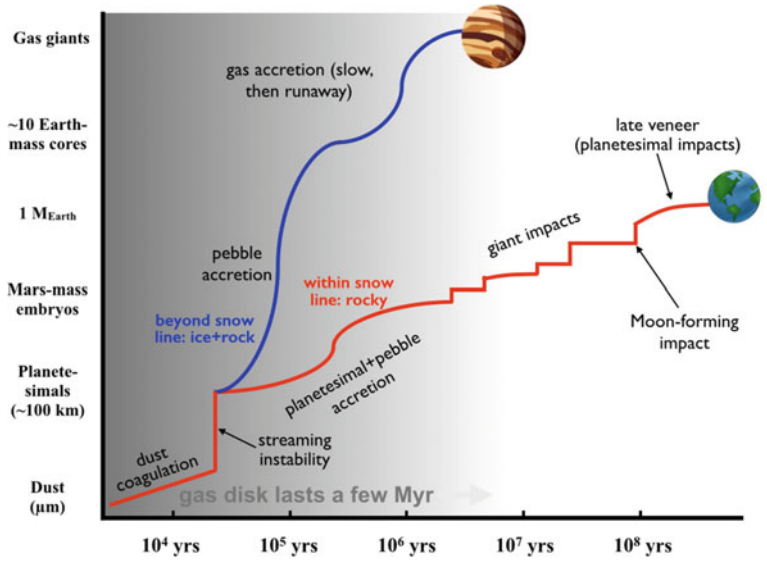

Fig. 1.1 Schematic view of some of the processes involved in forming Jupiter and Earth. This diagram is designed to present a broad view of the relevant mechanisms but still does not show a number of important effects. For instance, we know from the age distribution of primitive meteorites that planetesimals in the Solar System formed in many generations, not all at the same time. In addition, this diagram does not depict the large-scale migration thought to be ubiquitous among any planets more massive than roughly an Earth-mass (see discussion in text). Adapted from Meech and Raymond (2019)

where a_j, e_j, i_j, and m_j correspond to planet j's semimajor axis, eccentricity, orbital inclination, and mass. The Solar System's terrestrial planets have an AMD of 0.0018.

The radial mass concentration statistic RMC (called S_c by Chambers 2001) is a measure of the radial mass profile of the planets. It is defined as:

$$RMC = \max\left(\frac{\sum m_j}{\sum m_j[\log_{10}(a/a_j)]^2}\right). \tag{1.2}$$

The function in brackets is calculated sweeping a across all radii, and the RMC represents the maximum. For a one-planet system RMC is infinite. The RMC is higher when the planets' masses are concentrated in narrow radial zones (as is the case in the terrestrial planets, with two large central planets and two small exterior ones). The RMC becomes smaller for systems that are more spread out and systems in which all planets have similar masses. The Solar System's terrestrial planets' RMC is 89.9.

Confronting distributions of simulated planets with these empirical statistics (as well as other ones) has become a powerful and commonly-used discriminant of

terrestrial planet formation models (Chambers 2001; O'Brien et al. 2006; Raymond et al. 2006a, 2009b, 2014; Clement et al. 2018; Lykawka and Ito 2019).

- **The masses and orbits of the giant planets**. As for the terrestrial planets, the number (two gas giant, two ice giant), masses and orbits of the giant planets are the central constraints. The orbital spacing of the planets is also important, for instance the fact that no pair of giant planets is located in mean motion resonance. An important, overarching factor is simply that the Solar System's giant planets are located far from the Sun, well exterior to the orbits of the terrestrial planets.
- **The orbital and compositional structure of the asteroid belt**. While spread over a huge area, the asteroid belt contains only $\sim 4.5 \times 10^{-4}\, M_\oplus$ in total mass (Krasinsky et al. 2002; Kruijer and Folkner 2013; DeMeo and Carry 2013), orders of magnitude less than would be inferred from models of planet-forming disks such as the very simplistic minimum-mass solar nebula model (Weidenschilling 1977a; Hayashi 1981). The orbits of the asteroids are excited, with eccentricities that are roughly evenly distribution from zero to 0.3 and inclinations evenly spread from zero to more than 20° (a rough stability limit given the orbits of the planets). While there are a number of compositional groups within the belt, the general trend is that the inner main belt is dominated by S-types and the outer main belt by C-types (Gradie and Tedesco 1982; DeMeo and Carry 2013, 2014). S-type asteroids are associated with ordinary chondrites, which are quite dry (with water contents less than 0.1% by mass), and C-types are linked with carbonaceous chondrites, some of which (CI, CM meteorites) contain ~10% water by mass (Robert et al. 1977; Kerridge 1985; Alexander et al. 2018).
- **The cosmochemically-constrained growth histories of rocky bodies in the inner Solar System**. Isotopic chronometers have been used to constrain the accretion timescales of different solid bodies in the Solar System. Ages are generally measured with respect to CAIs (Calcium and Aluminum-rich Inclusions), mm-sized inclusions in chondritic meteorites that are dated to be 4.568 Gyr old (Bouvier and Wadhwa 2010). Cosmochemical measurements indicate that chondrules, which are similar in size to CAIs, started to form at roughly the same time (Connelly et al. 2008; Nyquist et al. 2009). Age dating of iron meteorites suggests that differentiated bodies—large planetesimals or planetary embryos—were formed in the inner Solar System within 1 Myr of CAIs (Halliday and Kleine 2006; Kruijer et al. 2014; Schiller et al. 2015). Isotopic analyses of Martian meteorites show that Mars was fully formed within 5−10 Myr after CAIs (Nimmo and Kleine 2007; Dauphas and Pourmand 2011), whereas similar analyses of Earth rocks suggest that Earth's accretion did not finish until much later, roughly 100 Myr after CAIs (Touboul et al. 2007; Kleine et al. 2009).

  There is evidence that two populations of isotopically-distinct chondritic meteorites—the so-called carbonaceous and non-carbonaceous meteorites—have similar age distributions (Kruijer et al. 2017). Given that chondrules are expected to undergo very fast radial drift within the disk (Weidenschilling 1977b; Lambrechts and Johansen 2012), this suggests that the two populations were kept apart and radially segregated, perhaps by the early growth of Jupiter's core (Kruijer et al. 2017).

Constraints from Observations of Planet-Forming Disks Around Other Stars

Gas-dominated protoplanetary disks are the birthplaces of planets. Disks' structure and evolution plays a central role in numerous processes such as how dust drifts (Birnstiel et al. 2016), where planetesimals form (Drążkowska et al. 2016; Drążkowska and Alibert 2017), and what direction and how fast planets migrate (Bitsch et al. 2015a).

We briefly summarize the main observational constraints from protoplanetary disks for planet formation models (see also dedicated reviews: Williams and Cieza 2011; Armitage 2011; Alexander et al. 2014):

- **Disk lifetime**. In young clusters, virtually all stars have detectable hot dust, which is used as a tracer for the presence of gaseous disks (Haisch et al. 2001; Briceño et al. 2001). However, in old clusters very few stars have detectable disks. Analyses of a large number of clusters of different ages indicate that the typical timescale for disks to dissipate is a few Myr (Haisch et al. 2001; Briceño et al. 2001; Hillenbrand et al. 2008; Mamajek 2009). Figure 1.2 shows this trend, with the fraction of stars with disks decreasing as a function of cluster age. It is worth noting that observational biases are at play, as the selection of stars that are members of clusters can affect the interpreted disk dissipation timescale (Pfalzner et al. 2014).

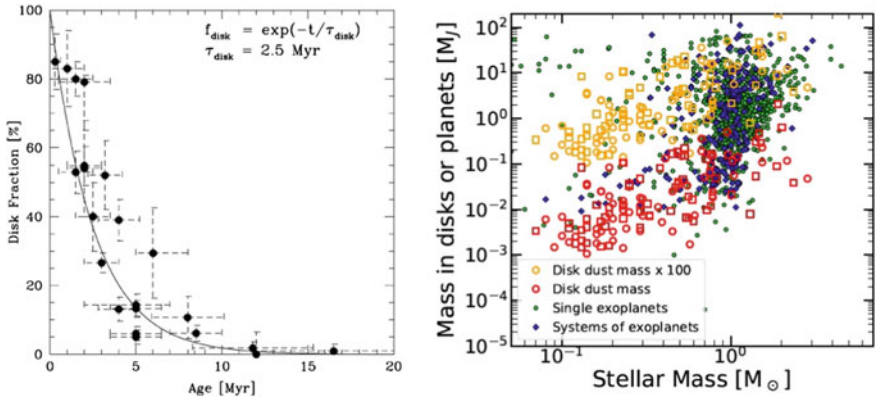

Fig. 1.2 Two observational constraints on planet-forming disks. *Left-hand panel:* The fraction of stars that have detectable disks in clusters of different ages. This suggests that the typical gaseous planet-forming disk only lasts a few Myr (Haisch et al. 2001; Briceño et al. 2001; Hillenbrand et al. 2008). Figure courtesy of Eric Mamajek, from Mamajek (2009). *Right-hand panel:* A comparison between inferred disk masses and the mass in planets in different systems, as a function of host star mass. The dust mass (red) is measured using sub-mm observations (and making the assumption that the emission is optically thin), and the gas mass is inferred by imposing a 100:1 gas to dust ratio. There is considerable tension, as the population of disks does not appear massive enough to act as the precursors of the population of known planets. The solution to this problem is not immediately obvious. Perhaps disk masses are systematically underestimated (Greaves and Rice 2011), or perhaps disks are continuously re-supplied with material from within their birth clusters via Bondi-Hoyle accretion (Throop and Bally 2008; Moeckel and Throop 2009). Figure courtesy of Carlo Felice Manara, from Manara et al. (2018)

- **Disk masses**. Most masses of protoplanetary disks are measured using sub-mm observations of the outer parts of the disk in which the emission is thought to be optically thin (Williams and Cieza 2011). Disk masses are commonly found to be roughly equivalent to 1% of the stellar mass, albeit with a 1–2 order of magnitude spread (Eisner and Carpenter 2003; Andrews and Williams 2005, 2007a; Andrews et al. 2010; Williams and Cieza 2011). It has recently been pointed out that there is tension between the inferred disk masses and the masses of exoplanet systems, as a large fraction of disks do not appear to contain enough mass to produce exoplanet systems (Manara et al. 2018; Mulders et al. 2018), even assuming a very high efficiency of planet formation (see Fig. 1.2).
- **Disk structure and evolution**. ALMA observations suggest that disks are typically 10–100 au in scale (Barenfeld et al. 2017), similar to the expected dimensions of the Sun's protoplanetary disk (Hayashi 1981; Gomes et al. 2004; Kretke and Lin 2012). Sub-mm observations at different radii indicate that the surface density of dust Σ in the outer parts of disks follows a roughly $\Sigma \sim r^{-1}$ radial surface density slope (Mulders et al. 2000; Looney et al. 2003; Andrews and Williams 2007b; Andrews et al. 2009), consistent with simple models for accretion disks. Many disks observed with ALMA show ringed substructure (ALMA Partnership 2015; Andrews et al. 2016, 2018). Disks are thought to evolve by accreting onto their host stars, and the accretion rate itself has been measured to vary as a function of time; indeed, the accretion rate is often used as a proxy for disk age (Hartmann et al. 1998; Armitage 2011). As disks age, they evaporate from the inside-out by radiation from the central star (Alexander and Armitage 2006; Owen et al. 2011; Alexander et al. 2014) and, depending on the stellar environment, may also evaporate from the outside-in due to external irradiation (Hollenbach et al. 1994; Adams et al. 2004).
- **Dust around older stars**. Older stars with no more gas disks often have observable dust, called *debris disks* (recent reviews: Matthews et al., 2014; Hughes et al., 2018). Roughly 20% of Sun-like stars are found to have dust at mid-infrared wavelengths (Bryden et al. 2006; Trilling et al. 2008; Montesinos et al. 2016). This dust is thought to be associated with the slow collisional evolution of outer planetesimal belts akin to our Kuiper belt, but generally containing much more mass (Wyatt 2008; Krivov 2010). The occurrence rate of dust is observed to decrease with the stellar age (Meyer et al. 2008; Carpenter et al. 2009). More [less] massive stars have significantly higher [lower] occurrence of debris disks (Su et al. 2006; Lega et al. 2012). There is no clear observed correlation between debris disks and planets (Moro-Martín et al. 2007, 2015; Marshall et al. 2014). A significant fraction of old stars have been found to have warm or hot *exo-zodiacal* dust (Absil et al. 2010; Ertel et al. 2014; Kral et al. 2017). The origin of this dust remains mysterious as there is no clear correlation between the presence of cold and hot dust (Ertel et al. 2014).

Constraints from Extra-Solar Planets

With a catalog of thousands of known exoplanets, the constraints from planets around other stars are extremely rich and constantly being improved. Figure 1.3 shows the

orbital architecture of a (non-representative) selection of known exoplanet systems. While there exist biases in the detection methods used to find exoplanets (Winn and Fabrycky 2015), their sheer number form the basis of a statistical framework with which to confront planet formation theories.

We can grossly summarize the exoplanet constraints as follows:

- **Occurrence and demographics**. Over the past few decades it has been shown using multiple techniques that exoplanets are essentially ubiquitous (Mayor et al. 2011; Cassan et al. 2012; Batalha et al. 2013). Despite the observational biases, a huge diversity of planetary systems has been discovered. Yet when drawing analogies with the Solar System, it is worth noting that, if our Sun were to have been observed with present-day technology, Jupiter is the only planet that could have been detected (Morbidelli and Raymond 2016; Raymond et al. 2018d). This makes the Solar System unusual at roughly the 1% level. In addition, the Solar System is borderline unusual in *not* containing any close-in low-mass planets (Martin and Livio 2015; Mulders et al. 2018). For the purposes of this review we focus on two categories of planets: gas giants and close-in low-mass planets, made up of high-density 'super-Earths' and puffy 'mini-Neptunes'.
- **Gas giant planets: occurrence and orbital distribution**. Radial velocity surveys have found giant planets to exist around roughly 10% of Sun-like stars (Cumming et al. 2008; Mayor et al. 2011). Roughly one percent of Sun-like stars have *hot Jupiters* on very short-period orbits (Howard et al. 2010; Wright et al. 2011), very few have *warm Jupiters* with orbital radii of up to $0.5-1$ au (Butler et al. 2006; Udry et al. 2007), and the occurrence of giant planets increases strongly and plateaus between 1 to several au, and there are hints that it decreases again farther out (Mayor et al. 2011; Fernandes et al. 2019); see Fig. 1.16. Direct imaging surveys have found a dearth of giant planets on wide-period orbits, although only massive young planets tend to be detectable (Bowler and Nielsen 2018). Microlensing surveys find a similar overall abundance of gas giants as radial velocity surveys and have shown that ice giant-mass planets appear to be far more common than their gas giant counterparts (Gould et al. 2010; Suzuki et al. 2016b). Giant planet occurrence has also been shown to be a strong function of stellar metallicity, with higher metallicity stars hosting many more giant planets (Gonzalez et al. 1997; Santos et al. 2001; Laws et al. 2003; Fischer and Valenti 2005; Dawson and Murray-Clay 2013). More in-depth discussions of the above trends in giant planet demographics at short, intermediate, and wide separations are presented in Chap. 3 and 4.
- **Close-in low-mass planets: occurrence and orbital distribution**. Perhaps the most striking exoplanet discovery of the past decade was the amazing abundance of close-in small planets. Planets between roughly Earth and Neptune in size or mass with orbital periods shorter than 100 days have been shown to exist around roughly $30-50\%$ of all main sequence stars (Mayor et al. 2011; Howard et al. 2012; Fressin et al. 2013; Dong and Zhu 2013; Petigura et al. 2013; Winn and Fabrycky 2015). Both the masses and radii have been measured for a subset of planets (Marcy et al. 2014) and analyses have shown that the smaller planets tend to have high

densities and the larger ones have low densities, which has been interpreted as a transition between rocky 'super-Earths' and gas-rich 'mini-Neptunes' with a transition size or mass of roughly $1.5-2\,R_\oplus$ or $\sim 3-5\,M_\oplus$ (Weiss et al. 2013; Weiss and Marcy 2014; Rogers 2015; Wolfgang et al. 2016; Chen and Kipping 2017). For the purposes of this review we generally lump together all close-in planets smaller than Neptune and call them *super-Earths* for simplicity. The super-Earth population has a number of intriguing characteristics that constrain planet formation models. While they span a range of sizes, within a given system super-Earths tens to have very similar sizes (Millholland et al. 2017; Weiss et al. 2018). Their period ratios form a broad distribution and do not cluster at mean motion resonances (Lissauer et al. 2011; Fabrycky et al. 2014). Finally, in the Kepler survey the majority of super-Earth systems only contain a single super-Earth (Batalha et al. 2013; Rowe et al. 2014), which contrasts with the high-multiplicity rate found in radial velocity surveys (Mayor et al. 2011). For detailed reviews and discussions on the demographics of close-in small planets we refer the reader to Chap. 3.

Outline of This Review

The rest of this chapter is structured as follows.

In Sect. 1.2 we will describe six essential mechanisms of planet formation. These are:

- The structure and evolution of protoplanetary disks (Sect. 1.2.1)
- The formation of planetesimals (Sect. 1.2.2)
- Accretion of protoplanets (Sect. 1.2.3)
- Orbital migration of growing planets (Sect. 1.2.4)
- Gas accretion and giant planet migration (Sect. 1.2.5)
- Resonance trapping during planet migration (Sect. 1.2.6).

This list does not include every process related to planet formation. These processes have been selected because they are both important and are areas of active study.

Next we will build global models of planet formation from these processes (Sect. 1.3). We will first focus on models to match the intriguing population of close-in small/low-mass planets: the *super-Earths* (Sect. 1.3.1). Next we will turn our attention to the population of giant planets, using the population of known giant exoplanets to guide our thinking about the formation of our Solar System's giant planets (Sect. 1.3.2). Next we will turn our attention to matching the Solar System itself (Sect. 1.3.3), starting from the classical model of terrestrial planet formation (Sect. 1.3.3.1) and then discussing newer ideas: the Grand Tack (Sect. 1.3.3.2), Low-mass Asteroid belt (Sect. 1.3.3.3) and Early Instability (Sect. 1.3.3.4) models. Then we will discuss the different sources of water on rocky exoplanets, and use cosmochemical measurements to constrain the origin of Earth's water (Sect. 1.3.4). Finally, in Sect. 1.4 we will lay out a path for the future trajectory of planet formation studies.

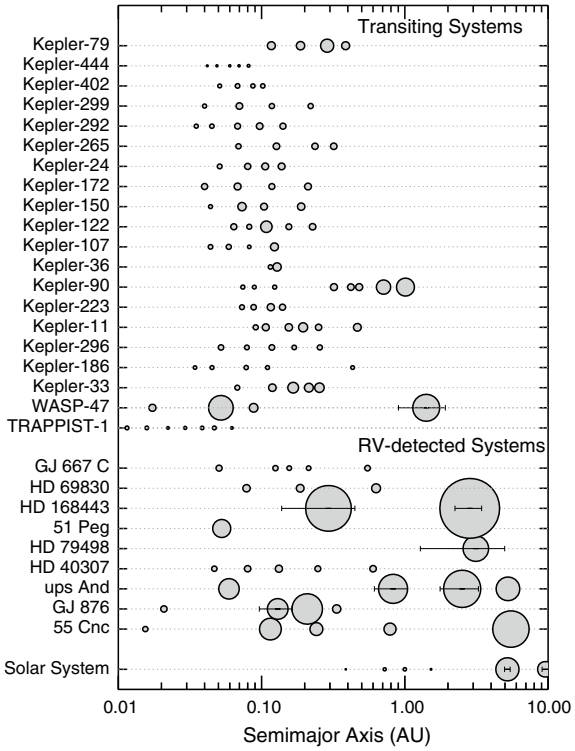

Fig. 1.3 A sample of exoplanet systems selected by hand to illustrate their diversity (adapted from Raymond et al., 2018d). The systems at the top were discovered by the transit method and the bottom systems by radial velocity (RV). Of course, some planets are detected in both transit and RV (e.g. 55 Cnc e; Demory et al., 2011). The planet's size is proportional to its actual size (but is not to scale on the x-axis). For RV planets without transit detections we used the $M \sin i \propto R^{2.06}$ scaling law derived by Lissauer et al. (2011). For giant planets ($M > 50\,M_{\oplus}$) on eccentric orbits ($e > 0.1$; also for Jupiter and Saturn), the horizontal error bar represents the planet's pericenter to apocenter orbital excursion. The central stars vary in mass and luminosity; e.g., TRAPPIST-1 is an ultracool dwarf star with mass of only $0.09\,M_{\odot}$ (Gillon et al. 2017). A handful of systems have ~Earth-sized planets in their star's habitable zones, such as Kepler-186 (Quintana et al. 2014), TRAPPIST-1 (Gillon et al. 2017), and GJ 667 C (Anglada-Escudé et al. 2013). Some planetary systems—for example, 55 Cancri (Fischer et al. 2008)—are found in multiple star systems

1.2 Key Processes in Planet Formation

In this section we review basic properties that affect the disk's structure, planetesimals and planet formation as well as dynamical evolution. These processes build the skeleton of our understanding of how planetary systems are formed. As pieces of a puzzle, they will then be put together to develop models on the origin of the different observed structures of planetary systems in Sect. 1.3.

1.2.1 Protoplanetary Disks: Structure and Evolution

Planet formation takes place in gas-dominated disks around young stars. These disks were inferred by Laplace (1822) from the near-perfect coplanarity of the orbits of the planets of the Solar System and of angular momentum conservation during the process of contraction of gas towards the central star. Disks are now routinely observed (imaged directly or deduced through the infrared excess in the spectral energy distribution) around young stars. The largest among protoplanetary disks are now resolved by the ALMA mm-interferometer (Andrews et al. 2018). Here we briefly review the viscous-disk model and the wind-dominated model. For more in depth reading we recommend Armitage (2011) and Turner et al. (2014).

1.2.1.1 Viscous-Disk Model(s)

The simplest model of a protoplanetary disk is a donut of gas and dust in rotation around the central star evolving under the effect of its internal viscosity. This is hereafter dubbed the *viscous-disk model*. Because of Keplerian shear, different rings of the disk rotate with different angular velocities, depending on their distance from the star. Consequently, friction is exerted between adjacent rings. The inner ring, rotating faster, tends to accelerate the outer ring (i.e. it exerts a positive torque) and the outer ring tends to decelerate the inner ring (i.e. exerting a negative torque of equal absolute strength). It can be demonstrated (see for instance Hahn 2009) that such a torque is

$$T = 3\pi\Sigma\nu r^2\Omega, \tag{1.3}$$

where Σ is the surface density of the disk at the boundary between the two rings, ν is the viscosity, and Ω is the rotational frequency at the distance r from the star.

A fundamental assumption of a viscous-disk model is that it is in steady state, which means the the mass flow of gas $\dot{M}$ is the same at any distance r. Under this assumption it can be demonstrated that the gas flows inwards with a radial speed

$$v_r = -\frac{3}{2}\frac{\nu}{r} \tag{1.4}$$

and that the product $\nu\Sigma$ is independent of r. That is, the radial dependence of Σ is the inverse of the radial dependence of ν. Of course the steady-state assumption is valid only in an infinite disk. In a more realistic disk with a finite size, this assumption is good only in the inner part of the disk, whereas the outer part expands into the vacuum under the effect of the viscous torque (Lynden-Bell and Pringle 1974).

If viscosity rules the radial structure of the disk, pressure rules the vertical structure. At steady state, the disk has to be in hydrostatic equilibrium, which means that the vertical component of the gravitational force exerted by the star has to be equal and opposite to the pressure force, i.e.:

$$\frac{GM_\star}{r^3}z = -\frac{1}{\rho}\frac{\mathrm{d}P}{\mathrm{d}z}, \tag{1.5}$$

where $M_\star$ is the mass of the star, z is the height over the disk's midplane, ρ is the volume density of the disk and P is its pressure. Using the perfect gas law $P = \mathcal{R}\rho T/\mu$ (where $\mathcal{R}$ is the gas constant, μ is the molecular weight of the gas and T is the temperature) and assuming that the gas is vertically isothermal (i.e. T is a function of r only), Eq. (1.5) gives the solution:

$$\rho(z) = \rho(0)\exp\left(-\frac{z^2}{2H^2}\right), \tag{1.6}$$

where $H = \sqrt{\mathcal{R}r^3T/\mu}$ is called the *pressure scale-height* of the disk (the gas extends to several scale-heights, with exponentially vanishing density).

We now need to compute $T(r)$. The simplest way is to assume that the disk is solely heated by the radiation from the central star (passive disk assumption, see Chiang and Goldreich 1997). Most of the disk is opaque to radiation, so the star can illuminate and deposit heat only on the surface layer of the disk, here defined as the layer where the integrated optical depth along a stellar ray reaches unity. For simplicity, we assume that the stellar radiation hits a hard surface, whose height over the midplane is proportional to the pressure scale-height H. Then, the energy deposited on this surface between r and $r + \delta r$ from the star is:

$$E_+^{Irr} = \left(\frac{L_\star}{4\pi r^2}\right)(2\pi r)(r\delta h), \tag{1.7}$$

where δh is the change in aspect ratio H/r over the range δr, namely $\mathrm{d}(H/r)/\mathrm{d}r\,\delta r$; the parentheses have been put in (1.7) to regroup the terms corresponding respectively to (1) stellar brightness $L_\star$ at distance r, (2) circumference of the ring and (3) projection of $H(r+\delta r) - H(r)$ on the direction orthogonal to the stellar ray hitting the surface. On the other had, the same surface will cool by black-body radiation in space at a rate

$$E_-^{Irr} = 2\pi r\delta r\sigma T^4, \tag{1.8}$$

where σ is Boltzmann's constant. Equating (1.7) and (1.8) and remembering the definition of H as a function of r and T leads to

$$T(r) \propto r^{-3/7} \text{ and } \quad H/r \propto r^{2/7}. \tag{1.9}$$

The positive exponent in the dependence of the aspect ratio H/r on r implies that the disk is *flared*. Notice that neither quantities in Eq. (1.9) depend on disk's surface density, opacity or viscosity.

However, because we are dealing with a viscous disk, we cannot neglect the heat released by viscous dissipation, i.e. in the friction between adjacent rings rotating at different speeds. Over a radial width δr, this friction dissipates energy at a rate

(Armitage 2011)

$$E_{+}^{Visc} = \frac{9}{8}\Sigma\nu\Omega^2 2\pi r\delta r. \tag{1.10}$$

This heat is dissipated mostly close to the midplane, where the disk's volume density is highest. This changes the cooling with respect to Eq. (1.8). The energy cannot be freely irradiated in space; it has first to be transported from the midplane through the disk, which is opaque to radiation, to the "surface" boundary with the optically thin layer. Thus the cooling term in Eq. (1.8) has to be divided by $\kappa\Sigma$, where κ is the disk's opacity. Again, by balancing heating and cooling and the definition of H we find:

$$H/r \propto (\dot{M}^2\kappa/\nu r)^{1/8}, \tag{1.11}$$

where we have used that $\dot{M} = 2\pi r v_r \Sigma = -3\pi\nu\Sigma$.

To know the actual radial dependence of this expression, we need to know the radial dependences of κ and ν (remember that $\dot{M}$ is assumed to be independent of r). The opacity depends on temperature, hence on r in a complicated manner, with abrupt transitions when the main chemical species (notably water) condense (Bell and Lin 1994). Let's ignore this for the moment. Concerning $\nu(r)$, Shakura and Sunyaev (1973) proposed from dimensional analysis that the viscosity is proportional to the square of the characteristic length of the system and is inversely proportional to the characteristic timescale. At a distance r from the star, the characteristic length of a disk is $H(r)$ and the characteristic timescale is the inverse of the orbital frequency Ω. Thus they postulated $\nu = \alpha H^2\Omega$, where α is an unknown coefficient of proportionality. If one adopts this prescription for the viscosity, the viscous-disk model is qualified as an *α-disk model*. Injecting this definition of ν into Eq. (1.11), one obtains

$$H/r \propto \left(\frac{\kappa\dot{M}^2}{\alpha}\right)^{1/10} r^{1/20}. \tag{1.12}$$

This result implies that the aspect ratio of a viscously heated disk is basically independent of r (and $T \propto 1/r$), in sharp contrast with the aspect ratio of a passive disk. Because the disk is both heated by viscosity and illuminated by the star, its aspect ratio at each r will be the maximum between Eqs. (1.12) and (1.9): it will be flat in the inner part and flared in the outer part. Because Eq. (1.12) depends on opacity, accretion rate and α, the transition from the flat disk and the flared disk will depend on these quantities. In particular, given that $\dot{M}$ decreases with time as the disk is consumed by accretion of gas onto the star (Hartmann et al. 1998), this transition moves towards the star as time progresses (Bitsch et al. 2015a). The effects of non-constant opacity introduce wiggles of H/r over this general trend (Bitsch et al. 2015a).

The viscous disk model is simple and neat, but its limitation is in the understanding of the origin of the disk's viscosity. The molecular viscosity of the gas is by orders of magnitude insufficient to deliver the observed accretion rate $\dot{M}$ onto the central star (Hartmann et al. 1998) given a reasonable disk's density, comparable to that of the Minimum Mass Solar Nebula model (MMSN: Weidenschilling 1977a; Hayashi

1981). It was thought that the main source of viscosity is turbulence and that turbulence was generated by the magneto-rotational instability (see Balbus and Hawley 1998). But this instability requires a relatively high ionization of the gas, which is prevented when grains condense in abundance, at a temperature below $\sim$1000 K (Desch and Turner 2015). Thus, only the very inner part of the disk is expected to be turbulent and have a high viscosity. Beyond the condensation line of silicates, the viscosity should be much lower. Remembering that $\nu\Sigma$ has to be constant with radius, the drop of ν at the silicate line implies an abrupt increase of Σ. As we will see, this property has an important role in the drift of dust and the migration of planets. It was expected that near the surface of the disk, where the gas is optically thin and radiation from the star can efficiently penetrate, enough ionization may be produced to sustain the Magneto Rotational Instability (MRI; Stone et al. 1998). However, these low-density regions are also prone to other effects of non-ideal magneto-hydrodynamics (MHD), like ambipolar diffusion and the Hall effect (Bai and Stone 2013), which are expected to quench turbulence. Thus, turbulent viscosity does not seem to be large enough beyond the silicate condensation line to explain the stellar accretion rates that are observed. This has promoted an alternative model of disk structure and evolution, dominated by the existence of disk winds, as we review next.

1.2.1.2 Wind-Dominated Disk Models

Unlike viscous disk models, which can be treated with simple analytic formulae, the emergence of disk winds and their effects are consequence of non-ideal MHD. Thus their mathematical treatment is complicated and the results can be unveiled only through numerical simulations. Therefore, this section will remain at a phenomenological level. For an in-depth study, we refer the reader to Bai and Stone (2013), Turner et al. (2014) and Bai (2017).

As we have seen above, the ionized regions of the disk have necessarily a low density. If the disk is crossed by a magnetic field, the ions atoms in these low-density regions can travel along the magnetic field lines without suffering collision with neutral molecules. This is the essence of *ambipolar diffusion*.

Consider a frame co-rotating with the disk at radius r_0 from the central star. In this frame, fluid parcels feel an effective potential combining the gravitational and centrifugal potentials. If poloidal (r, z) magnetic field lines act as rigid wires for fluid parcels (which happens as long as the poloidal flow is slower than the local Alfvén speed[2].), then a parcel initially at rest at $r = r_0$ can undergo a runaway if the field line to which it is attached is more inclined than a critical angle. Along such a field line, the effective potential decreases with distance, leading to an acceleration of magnetocentrifugal origin. This yields the inclination angle criterion $\theta > 30°$ for the

[2] The Alfvén speed is defined as the ratio between the magnetic field intensity B and $\sqrt{\mu_0 \rho}$, where μ_0 is the permeability of vacuum and ρ is the total mass density of the charged plasma particles. Apart from relativity effects, the Alfvén speed is the phase speed of the Alfvén wave, which is a magnetohydrodynamic wave in which ions oscillate in response to a restoring force provided by an effective tension on the magnetic field lines.

disk-surface poloidal field with respect to the vertical direction. Here fluid parcels rotate at constant angular velocity and so increase their specific angular momentum. Angular momentum is thus extracted from the disk and transferred to the ejected material. As the disk loses angular momentum, some material has to be transferred towards the central star, driving the stellar accretion. The efficiency of this process is directly connected to the disk's magnetic field strength, with a stronger field leading to faster accretion.

In wind-dominated disk models the viscosity can be very low and the disk's density can be of the order of that of the MMSN. The observed accretion rate onto the central star is not due to viscosity (the small value of $\nu\Sigma$ provides only a minor contribution) but is provided by the radial, fast advection of a small amount of gas, typically at 3-4 pressure scale heights H above the disk's midplane (Gressel et al. 2015). The global structure of the disk can be symmetric (top panel of Fig. 1.4) or asymmetric (bottom panel of Fig. 1.4) depending on simulation parameters and the inclusion of different physical effects (e.g. the Hall effect). The origin of the asymmetry is not fully understood. In some cases, the magnetic field lines can be concentrated in narrow radial bands that can fragment the disk into concentric rings (Béthune 2017; see bottom panel of Fig. 1.4). This effect is intriguing in light of the recent ALMA observations of the ringed structure of protoplanetary disks (ALMA Partnership 2015; Andrews et al. 2016, 2018). It should be stressed, however, that there is currently no consensus on the origin of the observed rings. An alternative possibility is that they are the consequence of planet formation (Zhang 2018) or of other disk instabilities (Tominaga et al. 2019). Understanding whether ring formation in protoplanetary disks is a prerequisite for, or a consequence of, planet formation is an essential goal of current research.

Depending on assumptions on the radial gradient of the magnetic field, and hence of the strength of the wind, the gas density of the disk may be partially depleted in its inner part (Suzuki et al. 2016a) or preserve a global power-law structure similar to that of viscous-disk models (Bai 2016) (see Fig. 1.5). A positive surface density gradient, as in Suzuki et al. (2016a), has implication for the radial drift of dust and planetesimals (Ogihara et al. 2018a) and for the migration of protoplanets (Ogihara et al. 2018b). In addition, in Suzuki et al. (2016a) the maximum of the surface density (where dust and migrating planets tend to accumulate) moves outwards as time progresses and the disk evolves.

Disk winds do not generate an appreciable amount of heat. In wind-dominated models, the disk temperature is close to that of a passive disk (Mori et al. 2019; Chambers 2006b), which has a snowline inward of 1 au (Bitsch et al. 2015a). The deficit of water in inner solar system bodies (the terrestrial planets and the parent bodies of enstatite and ordinary chondrites) demonstrates that the protoplanetary solar disk inwards of 2–3 au was warm, at least initially (Morbidelli et al. 2016). This implies that either the viscosity of the disk was quite high or another form of heating—for instance the adiabatic compression of gas as it fell onto the disk from the interstellar medium—was operating early on.

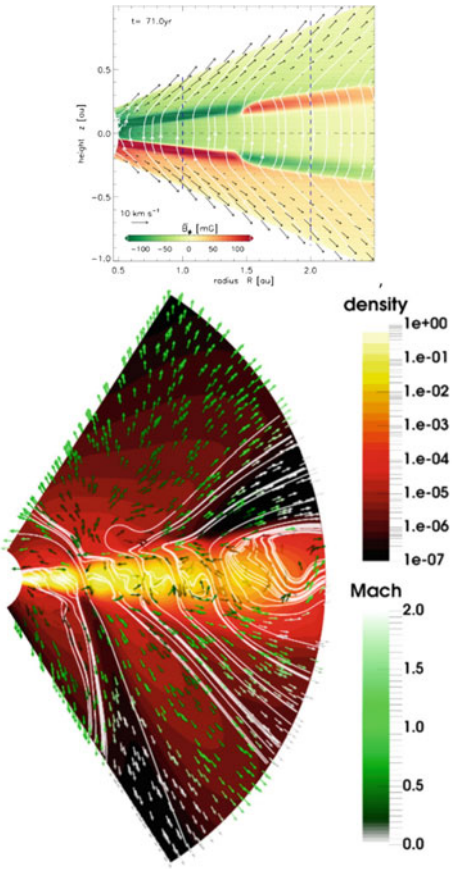

Fig. 1.4 Disk structure in two different wind-dominated disk global models. The top panel (figure courtesy of Oliver Gressel) from Gressel et al. (2015), shows the intensity and polarity of the magnetic field, the field lines and the velocity vectors of the wind. This disk model is symmetric relative to the mid-plane (anti-symmetric in polarity). The bottom panel (figure courtesy of William Béthune) from Béthune et al. (2017), shows the gas density, the magnetic field lines and the wind velocity vectors. This model has no symmetry relative to the midplane. Moreover, the disk is fragmented in rings by the accumulation of magnetic field lines in specific radial intervals

1.2.1.3 Dust Dynamics

The dynamics of dust particles is largely driven by gas drag. Any time that there is a difference in velocity between the gas and the particle, a drag force is exerted on the particle which tends to erase the velocity difference. The *friction time* t_f is defined as the coefficient that relates the accelerations felt by the particle to the gas-particle velocity difference, namely:

$$\dot{\mathbf{v}} = -\frac{1}{t_f}(\mathbf{v} - \mathbf{u}), \tag{1.13}$$

where $\mathbf{v}$ is the particle velocity vector and $\mathbf{u}$ is the gas velocity vector, while $\dot{\mathbf{v}}$ is the particle's acceleration. The smaller a dust particle the shorter its t_f. In the Epstein regime, where the particle size is smaller than the mean free path of a gas molecule, t_f is linearly proportional to the particle's size R. In the Stokes regime the particle size is larger than the mean free path of a gas molecule and $t_f \propto \sqrt{R}$. It is convenient

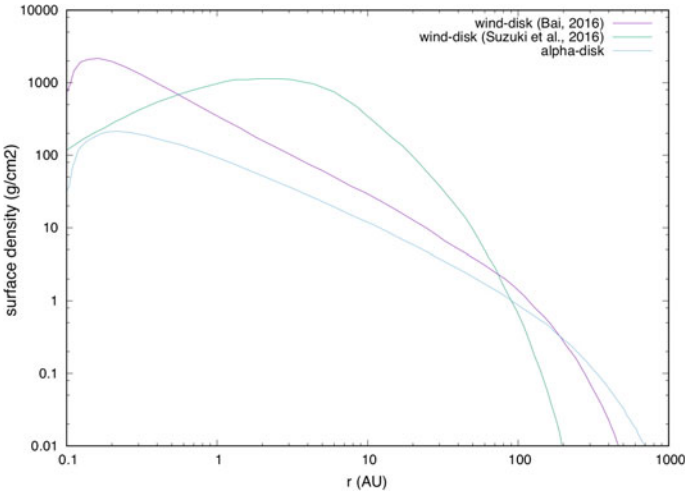

Fig. 1.5 Comparison between the radial surface density distribution of the wind-dominated disk models of Suzuki et al. (2016a), Bai (2016) and an α-disk model

to introduce a dimensionless number, called the *Stokes number*, defined as $\tau_s = \Omega t_f$, which represents the ratio between the friction time and the orbital timescale.

The effects of gas drag are mainly the sedimentation of dust towards the midplane and its radial drift towards pressure maxima.

To describe an orbiting particle as it settles in a disk, cylindrical coordinates are the natural choice. The stellar gravitational force can be decomposed into a radial and a vertical component. The radial component is canceled by the centrifugal force due to the orbital motion. The vertical component, $F_{g,z} = -m\Omega^2 z$, where m is the mass of the particle and z its vertical coordinate, instead accelerates the particle towards the midplane, until its velocity $v_{\rm settle}$ is such that the gas drag force $F_D = m v_{\rm settle}/t_f$ cancels $F_{g,z}$. This sets $v_{\rm settle} = \Omega^2 z t_f$ and gives a settling time $T_{\rm settle} = z/v_{\rm settle} = 1/(\Omega^2 t_f) = 1/(\Omega\tau_s)$. Thus, for a particle with Stokes number $\tau_s = 1$, the settling time is the orbital timescale. However, turbulence in the disk stirs up the particle layer, which therefore has a finite thickness. Assuming an α-disk model, the scale height of the particle layer is (Chiang and Youdin 2010):

$$H_p = \frac{H}{\sqrt{1 + \tau_s/\alpha}}. \tag{1.14}$$

Dust particles undergo radial drift due to a small difference of their orbital velocity relative to the gas. The gas feels the gravity of the central star and its own pressure. The pressure radial gradient exerts a force $F_r = -(1/\rho)\mathrm{d}P/\mathrm{d}r$ which can oppose or enhance the gravitational force. As we saw above, $P \propto \rho T$, and $\rho \sim \Sigma/H$. Because Σ and T in general decrease with r, $\mathrm{d}P/\mathrm{d}r < 0$. The pressure force opposes to the gravity force, diminishing it. Consequently, the gas parcels orbit the star at a speed that is slightly slower than the Keplerian speed at the same location. The difference between the Keplerian speed v_k and the gas orbital speed is $\eta\, v_K$, where

$$\eta = -\frac{1}{2}\left(\frac{H}{r}\right)^2 \frac{\mathrm{d}\log P}{\mathrm{d}\log r}. \tag{1.15}$$

The radial velocity of a particle is then:

$$v_r = -2\eta v_K \tau_s/(\tau_s^2 - 1) + u_r/(\tau_s^2 - 1), \tag{1.16}$$

where u_r is the radial component of the gas velocity. Except for extreme cases, u_r is very small and hence the second term in the right-hand side of Eq. (1.16) is negligible relative to the first term. Consequently, the direction of the radial drift of dust depends on the sign of η, i.e., from Eq. (1.15), on the sign of the pressure gradient. If the gradient is negative as in most parts of the disk, the drift is inwards. But in the special regions where the pressure gradient is positive, the particle's drift is outwards. Consequently, dust tends to accumulate at pressure maxima in the disk. We have seen above that the MHD dynamics in the disk can create a sequence of rings and gaps, where the density is alternatively maximal and minimal (bottom panel of Fig. 1.4). Each of these rings therefore features a pressure maximum along a circle. In absence of diffusive motion, the dust would form an infinitely thin ring at the pressure maximum. Turbulence produces diffusion of the dust particles in the radial direction, as it does in the vertical direction. Thus, as dust sedimentation produces a layer with thickness given by Eq. (1.14), dust migration produces a ring with radial thickness $w_p = w/\sqrt{1 + \tau_s/\alpha}$ around the pressure maximum, where w is the width of the gas ring assuming that it has a Gaussian profile (Dullemond et al. 2018).

Consequently, observations of the dust distribution in protoplanetary disks can provide information on the turbulence in the disk. The fact that the width of the gaps in the disk of HL Tau appears to be independent of the azimuth despite the fact that the disk is viewed with an angle smaller than 90°, suggests that the vertical diffusion of dust is very limited such that α in Eq. (1.14) must be be 10^{-4} or less (Pinte et al. 2016). In contrast, the observation that dust is quite broadly distributed in each ring of the disks, suggest that α could be as large as 10^{-3}, depending on the particles Stokes number τ_s, which is not precisely known (Dullemond et al. 2018). These observations therefore suggest that turbulence in the disks is such that the vertical diffusion it produces is weaker than the radial diffusion. It is yet unclear which mechanism could generate turbulence with this property.

1.2.2 Planetesimal Formation

Dust particles orbiting within a disk often collide. If collisions are sufficiently gentle, they stick through electrostatic forces, forming larger particles (Blum and Wurm 2008). One could imagine that this process continues indefinitely, eventually forming macroscopic bodies called planetesimals. However, as we have seen above, particles drift through the disk at different speeds depending on their size (or Stokes number). Thus, there is a minimum speed at which particles of different sizes can collide.

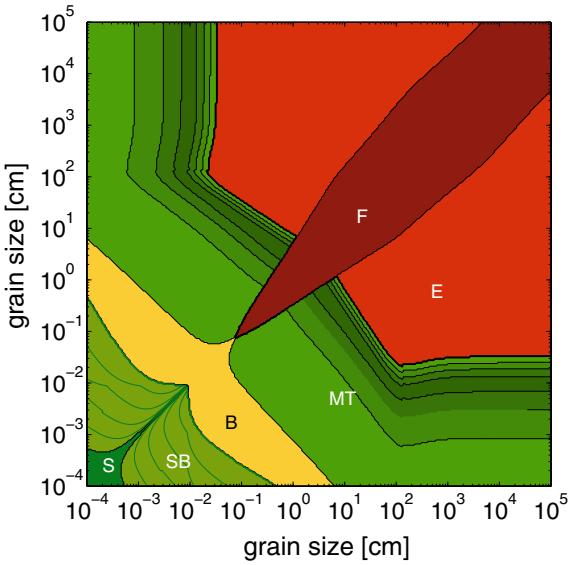

Fig. 1.6 Map of collisional outcome in the disk (figure courtesy of Fredrik Windmark, from Windmark et al., 2012). The sizes of colliding particles are reported on the axes. The colours denote the result of each pair-wise collision. Green denotes growth, red denotes erosion and yellow denotes neither of the above (i.e. a bounce). The label S stands for sticking, SB for stick and bounce, B for bounce, MT for mass transfer, E for erosion and F for fragmentation. This map is computed for compact (silicate) particles, at 3 au

Particles of equal size also have a distribution of impact velocities due to turbulent diffusion.

Figure 1.6 shows a map of the outcome of dust collisions within a simple disk model, from Windmark et al. (2012). Using laboratory experiments on the fate of collisions as a function of particle sizes and mutual velocities, and considering a disk with turbulent diffusion $\alpha = 10^{-3}$ and drift velocities as in a MMSN disk, Windmark et al. (2012) computed the growth/disruption maps for different heliocentric distances. The one from Fig. 1.6 is for a distance of 3 au. The figure shows that, in the inner part of the disk, particles cannot easily grow beyond a millimeter in size. A bouncing barrier prevents particles to grow beyond this limit. If a particle somehow managed to grow to $\sim$10 cm, its growth could potentially resume by accreting tiny particles. But as soon as particles of comparable sizes hit each other, erosion or catastrophic fragmentation occurs, thus preventing the formation of planetesimal-size objects.

The situation is no better in the outer parts of the disk. In the colder regions, due to the lower velocities and the sticking effect of water ice, particles can grow to larger sizes. But this size is nevertheless limited to a few centimeters due to the so-called *drift barrier* (i.e. large enough particles start drifting faster than they grow: Birnstiel et al. 2016). It has been proposed that if particles are very porous, they could absorb better the collisional energy, thus continuing to grow without bouncing or breaking (Okuzumi et al. 2012). Very porous planetesimals could in principle

form this way and their low densities would make them drift very slowly through the disk. But eventually these planetesimals would become compact under the effect of their own gravity and of the ram pressure of the flowing gas (Kataoka et al. 2013). This formation mechanism for planetesimals is still not generally accepted in the community. At best, it could work only in the outer part of the disk, where icy monomers have the tendency to form very porous structures, but not in the inner part of the disk, dominated by silicate particles. Moreover, meteorites show that the interior structure of asteroids is made mostly of compact particles of 100 microns to a millimeter in size, called chondrules, which is not consistent with the porous formation mode.

A mechanism called the *streaming instability* (Youdin and Goodman 2005) can bypass these growth bottlenecks to form planetesimals. Although originally found to be a linear instability (see Jacquet et al. 2011), this instability raises even more powerful effects, which can be qualitatively explained as follows. This instability arises from the speed difference between gas and solid particles. As the differential makes particles feel drag, the friction exerted from the particles back onto the gas accelerates the gas toward the local Keplerian speed. If there is a small overdensity of particles, the local gas is in a less sub-Keplerian rotation than elsewhere; this in turn reduces the local headwind on the particles, which therefore drift more slowly towards the star. Consequently, an isolated particle located farther away in the disc, feeling a stronger headwind and drifting faster towards the star, eventually joins this overdense region. This enhances the local density of particles and reduces further its radial drift. This process drives a positive feedback, i.e. an instability, whereby the local density of particles increases exponentially with time.

Particle clumps generated by the streaming instability can become self-gravitating and contract to form planetesimals. Numerical simulations of the streaming instability process (Johansen et al. 2015; Simon et al. 2016, 2017; Schäfer et al. 2017; Abod et al. 2019) show that planetesimals of a variety of sizes are produced, but those that carry most of the final total mass are those of $\sim$100 km in size. This size is indeed prominent in the observed size-frequency distributions of both asteroids and Kuiper-belt objects. Thus, these models suggest that planetesimals form (at least preferentially) big, in stark contrast with the collisional coagulation model, in which planetesimals would grow progressively from pair wise collisions. If the amount of solid mass in small particles is large enough, even Ceres-size planetesimals can be directly produced from particle clumps (Fig. 1.7).

While Fig. 1.7 shows that the streaming instability can clearly form planetesimals, a concern arises from the initial conditions of such simulations. Simulations find that quite large particles are needed for optimal concentration, corresponding to at least decimeters in size when applied to the asteroid belt. Chondrules—a ubiquitous component of primitive meteorites—typically have sizes from 0.1 to 1 mm but such small particles are hard to concentrate in vortices or through the streaming instability. High-resolution numerical simulations (Carrera et al. 2015; Yang et al. 2017) show that chondrule-size particles can trigger the streaming instability only if the initial mass ratio between these particles and the gas is larger than about 4%. The initial solid/gas ratio of the Solar-System disk is thought to have been $\sim$1%. At face value,

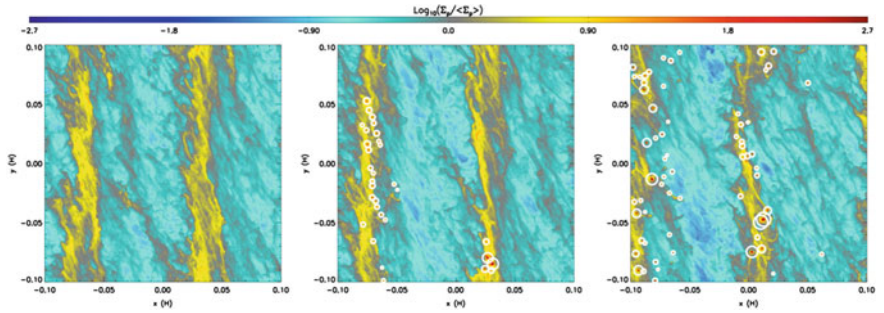

Fig. 1.7 Snapshots in time of a simulation of the streaming instability (figure courtesy of Jacob B. Simon, from Simon et al. 2016). The color scale shows the vertically integrated particle surface density normalized to the average particle surface density (log scale). Time increases from left to right. The left panel shows the clumping due to the streaming instability in the absence of self-gravity, but right before self-gravity is activated ($t = 110\,\Omega^{-1}$). The middle panel corresponds to a point shortly after self-gravity was activated ($t = 112.5\,\Omega^{-1}$), and the right panel corresponds to a time in which most of the planetesimals have formed ($t = 117.6\,\Omega^{-1}$). In the middle and right panel, each planetesimal is marked via a circle of the size of the Hill sphere

planetesimals should not have formed as agglomerates of chondrules. A possibility is that future simulations with even-higher resolution and run on longer timescales will show that the instability can occur for a smaller solid/gas ratio, approaching the value measured in the Sun.

Certain locations within the disk may act as preferred sites of planetesimal formation. Drifting particles may first accumulate at distinct radii in the disc where their radial speed is slowest and then, thanks to the locally enhanced particle/gas ratio, locally trigger the streaming instability. Two locations have been identified for this preliminary radial pile-up. One is in the vicinity of the snowline, where water transitions from vapor to solid form (Ida and Guillot 2016; Armitage et al. 2016; Schoonenberg and Ormel 2017). The other is in the vicinity of 1 au (Drążkowska et al. 2016). These could be the two locations where planetesimals could form very early in the protoplanetary disk (Drążkowska and Dullemond 2018). Elsewhere in the disk, the conditions for planetesimal formation via the streaming instability would only be met later on, when gas was substantially depleted by photo-evaporation from the central star, provided that the solids remained abundant (Throop and Bally 2008; Carrera et al. 2017).

At least at the qualitative level, this picture is consistent with available data for the Solar System. The meteorite record reveals that some planetesimals formed very early, in the first few 10^5 yr (Kleine et al. 2009; Kruijer et al. 2014; Schiller et al. 2015). Because of the large abundance of short-lived radioactive elements present at the early time (Grimm and McSween 1993; Monteux et al. 2018), these first planetesimals melted and differentiated, and are today the parent bodies of iron meteorites. But a second population of planetesimals formed 2 to 4 Myr later (Villeneuve et al. 2009). These planetesimals did not melt and are the parent bodies of the primitive meteorites called the chondrites. We can speculate that differentiated planetesimals formed at

the two particle pile-up locations mentioned above, whereas the undifferentiated planetesimals formed elsewhere, for instance in the asteroid belt while the gas density was declining. Yet these preferred locations were certainly themselves evolving in time (Drążkowska and Dullemond 2018).

Strong support for the streaming instability model comes from Kuiper belt binaries. These binaries are typically made of objects of similar size and identical colors (see Noll et al. 2008). It has been shown (Nesvorný et al. 2010) that the formation of a binary is the natural outcome of the gravitational collapse of the clump of pebbles formed in the streaming instability, if the angular momentum of the clump is large. Simulations of this process can reproduce the typical semi-major axes, eccentricities and size ratios of the observed binaries. The color match between the two components is a natural consequence of the fact that both are made of the same material. This is a big strength of the model because such color identity cannot be explained in any capture or collisional scenario, given the observed intrinsic difference in colors between any random pair of Kuiper belt objects (KBOs—this statement holds even restricting the analysis to the cold population, which is the most homogeneous component of the Kuiper belt population). Additional evidence for the formation of equal-size KBO binaries by streaming instability is provided by the spatial orientation of binary orbits. Observations (Noll et al. 2008) show a broad distribution of binary inclinations with $\simeq$80% of prograde orbits ($i_\mathrm{b} < 90°$) and $\simeq$20% of retrograde orbits ($i_\mathrm{b} > 90°$). To explain these observations, Nesvorný et al. (2019) analyzed high-resolution simulations and determined the angular momentum vector of the gravitationally bound clumps produced by the streaming instability. Because the orientation of the angular momentum vector is approximately conserved during collapse, the distribution obtained from these simulations can be compared with known binary inclinations. The comparison shows that the model and observed distributions are indistinguishable. This clinches an argument in favor of the planetesimal formation by the streaming instability and binary formation by gravitational collapse. No other planetesimal formation mechanism has been able so far to reproduce the statistics of orbital plane orientations of the observed binaries.

1.2.3 Accretion of Protoplanets

Once planetesimals appear in the disk they continue to grow by mutual collisions. Gravity plays an important role by bending the trajectories of the colliding objects, which effectively increases their collisional cross-section by a factor

$$F_g = 1 + V_\mathrm{esc}^2 / V_\mathrm{rel}^2, \tag{1.17}$$

where V_esc is the mutual escape velocity defined as $V_\mathrm{esc} = [2G(M_1 + M_2)/(R_1 + R_2)]^{1/2}$, M_1, M_2, R_1, R_2 are the masses and radii of the colliding bodies, V_rel is their relative velocity before the encounter and G is the gravitational constant. F_g is called the gravitational focusing factor (Safronov 1972).

The mass accretion rate of an object becomes

$$\frac{\mathrm{d}M}{\mathrm{d}t} \propto R^2 F_g \propto M^{2/3} F_g \,, \tag{1.18}$$

where the bulk density of planetesimals is assumed to be independent of their mass, so that the planetesimal physical radius $R \propto M^{1/3}$. These equations imply two distinct growth modes called runaway and oligarchic growth.

1.2.3.1 Runaway Growth

If one planetesimal (of mass M) grows quickly, then its escape velocity $V_{\rm esc}$ becomes much larger than its relative velocity $V_{\rm rel}$ with respect to the rest of the planetesimal population. Then, one can approximate F_g as $V_{\rm esc}^2 / V_{\rm rel}^2$. Notice that the approximation $R \propto M^{1/3}$ makes $V_{\rm esc}^2 \propto M^{2/3}$.

Substituting this expression into Eq. (1.18) leads to:

$$\frac{\mathrm{d}M}{\mathrm{d}t} \propto \frac{M^{4/3}}{V_{\rm rel}^2}, \tag{1.19}$$

or, equivalently:

$$\frac{1}{M}\frac{\mathrm{d}M}{\mathrm{d}t} \propto \frac{M^{1/3}}{V_{\rm rel}^2}. \tag{1.20}$$

This means that the relative mass-growth rate is a growing function of the body's mass. In other words, small initial differences in mass among planetesimals are rapidly magnified, in an exponential manner. This growth mode is called *runaway growth* (Greenberg et al. 1978; Wetherill and Stewart 1989, 1993; Kokubo and Ida 1996, 1998).

Runaway growth occurs as long as there are objects in the disk for which $V_{\rm esc} \gg V_{\rm rel}$. While $V_{\rm esc}$ is a simple function of the largest planetesimals' masses, $V_{\rm rel}$ is affected by other processes. There are two dynamical damping effects that act to decrease the relative velocities of planetesimals. The first is gas drag. Gas drag not only causes the drift of bodies towards the central star, as seen above, but it also tends to circularize the orbits, thus reducing their relative velocities $V_{\rm rel}$. Whereas orbital drift vanishes for planetesimals larger than about 1 km in size, eccentricity damping continues to influence bodies up to several tens of kilometers across. However, in a turbulent disk gas drag cannot damp $V_{\rm rel}$ down to zero: in presence of turbulence the relative velocity evolves towards a size-dependent equilibrium value (Ida and Lin 2008). The second damping effect is that of collisions. Particles bouncing off each other tend to acquire parallel velocity vectors, reducing their relative velocity to zero. For a given total mass of the planetesimal population, this effect has a strong dependence on the planetesimal size, roughly $1/r^4$ (Wetherill and Stewart 1993).

Meanwhile, relative velocities are excited by the largest growing planetesimals by gravitational scattering, whose strength depends on those bodies' escape velocities. A planetesimal that experiences a near-miss with the largest body has its trajectory permanently perturbed and will have a relative velocity $V_{\rm rel} \sim V_{\rm esc}$ upon the next return. Thus, the planetesimals tend to acquire relative velocities of the order of the escape velocity from the most massive bodies, and when this happens runaway growth is shut off (see below).

To have an extended phase of runaway growth in a planetesimal disk, it is essential that the bulk of the solid mass is in small planetesimals, so that the damping effects are important. Because small planetesimals collide with each other frequently and either erode into small pieces or grow by coagulation, this condition may not hold for long. Moreover, if planetesimals really form with a preferential size of ∼100 km, as in the streaming instability scenario, the population of small planetesimals would have been insignificant and therefore runaway growth would have only lasted a short time if it happened at all.

1.2.3.2 Oligarchic Growth

When the velocity dispersion of planetesimals becomes of the order of the escape velocity from the largest bodies, the gravitational focusing factor (Eq. 1.17) becomes of order unity. Consequently the mass growth equation (Eq. 1.18) becomes

$$\frac{1}{M}\frac{{\rm d}M}{{\rm d}t} \propto \frac{M^{-1/3}}{V_{\rm rel}^2}. \tag{1.21}$$

In these conditions, the relative growth rate of the large bodies slows with the bodies' growth. Thus, the mass ratios among the large bodies tend to converge to unity.

In principle, one could expect that the small bodies also narrow down their mass difference with the large bodies. But in reality, the large value of $V_{\rm rel}$ prevents the small bodies from accreting each other. Small bodies only contribute to the growth of the large bodies (i.e. those whose escape velocity is of the order of $V_{\rm rel}$). This phase is called *oligarchic growth* (Kokubo and Ida 1998, 2000).

In practice, oligarchic growth leads to the formation of a group of objects of roughly equal masses, embedded in the disk of planetesimals. The mass gap between oligarchs and planetesimals is typically of a few orders of magnitude. Because of dynamical friction—an equipartition of orbital excitation energy (Chandrasekhar 1943)—planetesimals have orbits that are much more eccentric than the oligarchs. The orbital separation among the oligarchs is of the order of 5 to 10 mutual Hill radii R_H, where:

$$R_H = \frac{a_1 + a_2}{2}\left(\frac{M_1 + M_2}{3M_\star}\right)^{1/3}, \tag{1.22}$$

and a_1, a_2 are the semi-major axes of the orbits of the objects with masses M_1, M_2, and $M_\star$ is the mass of the star.

1.2.3.3 The Need for an Additional Growth Process

In the classic view of planet formation (Wetherill 1992; Lissauer 1987, 1993), the processes of runaway growth and oligarchic growth convert most of the planetesimals mass into a few massive objects: the protoplanets (sometimes called *planetary embryos*). However, this picture does not survive close scrutiny.

In the Solar system, two categories of protoplanets formed within the few Myr lifetime of the gas component of the protoplanetary disk (see Fig. 1.2). In the outer system, a few planets of multiple Earth masses formed and were massive enough to be able to gravitationally capture a substantial mass of H and He from the disk and become the observed giant planets, from Jupiter to Neptune. In the inner disk, instead, the protoplanets only reached a mass of the order of the mass of Mars and eventually formed the terrestrial planets after the disappearance of the gas (see Sect. 1.3.3.1). Thus, the protoplanets in the outer part of the disk were 10-100 times more massive of those in the inner disk. This huge mass ratio is even more surprising if one considers that the orbital periods, which set the natural clock for all dynamical processes including accretion, are ten times longer in the outer disk.

The snowline represents a divide between the inner and the outer disk. The surface density of solid material is expected to increase beyond the snowline due to the availability of water ice (Hayashi 1981). However, this density-increase is only of a factor of $\sim$2 (Lodders 2003), which is insufficient to explain the huge mass ratio between protoplanets in the outer and inner parts of the disc (Morbidelli et al. 2015).

In addition, whereas in the inner disk oligarchic growth can continue until most of the planetesimals have been accreted by protoplanets, the situation is much less favorable in the outer disc. There, when the protoplanets become sufficiently massive (about 1 Earth mass), they tend to scatter the planetesimals away, rather than accrete them. In doing this, they clear their neighboring regions, which in turn limits their own growth (Levison et al. 2010). In fact, scattering dominates over growth when the ratio $V_{\rm esc}^2/2V_{\rm orb}^2 > 1$, where $V_{\rm esc}$ is the escape velocity from the surface of the protoplanet and $V_{\rm orb}$ is its orbital speed (so that $\sqrt{2}V_{\rm orb}$ is the escape velocity from the stellar potential well from the orbit of the protoplanet). This ratio is much larger in the outer disc than in the inner disc because $V_{\rm orb}^2 \propto 1/a$, where a is the orbital semi-major axis.

Consequently, understanding the formation of the multi-Earth-mass cores of the giant planets and their huge mass ratio with the protoplanets in the inner Solar System is a major problem of the runaway/oligarchic growth models, and it has prompted the elaboration of a new planet growth paradigm, named *pebble accretion*.

1.2.3.4 Pebble Accretion

Let's take a step back to what seems to be most promising planetesimal formation model: that of self-gravitating clumps of small particles (hereafter called pebbles even though in the inner disc they are expected to be at most mm-size, so that

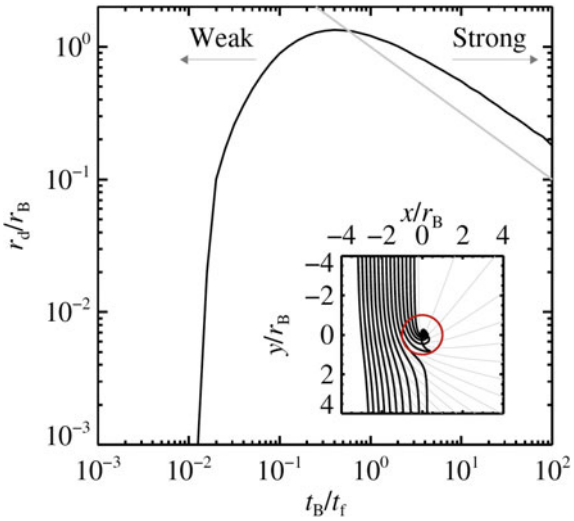

Fig. 1.8 Efficiency of pebble accretion. The outer plot shows the accretion radius r_d, normalized to the Bondi radius r_B, as a function of t_B/t_f, where t_f is the friction time and t_B is the time required to cross the Bondi radius at the encounter velocity $v_{\rm rel}$. The smaller is the pebble the larger is t_B/t_f. The inset shows pebble trajectories (black curves) with $t_B/t_f = 1$, which can be compared with those of objects with $t_B/t_f \to 0$ (grey curves). Clearly the accretion radius for the former is much larger. A circle of Bondi radius is plotted in red. Figure courtesy of M. Lambrechts, from Lambrechts and Johansen (2012)

grains would be a more appropriate term). Once a planetesimal forms, it remains embedded in the disk of gas and pebbles and it can keep growing by accreting individual pebbles. This process was first envisioned by Ormel and Klahr (2010) and then studied in detailed by Lambrechts and Johansen (2012, 2014) (see also Johansen and Lambrechts, 2017). To avoid confusion, we call below the accreting body a *protoplanet* and we denote the accreted body as a pebble or a planetesimal, depending on whether it feels strong gas drag.

Pebble accretion is more efficient than planetesimal accretion for two reasons. First, the accretion cross-section for a protoplanet-pebble encounter is much larger than for a protoplanet-planetesimal encounter. As seen above, in a protoplanet-planetesimal encounter the accretion cross-section is $\pi R^2 F_g$, where R is the physical size of the protoplanet and F_g is the gravitational focusing factor. But in a protoplanet-pebble encounter it can be as large as πr_d^2, where r_d is the distance at which the protoplanet can deflect the trajectories of the incoming objects. This is because, as soon as the pebble's trajectory starts to be deflected, its relative velocity with the gas increases and gas-drag becomes very strong. Thus, the pebble's trajectory spirals towards the protoplanet. This is shown in the inlet of Fig. 1.8, whereas the outer panel of the figure shows the value of r_d as a function of the pebble's friction time, normalized to the Bondi radius $r_B = GM/v_{\rm rel}^2$ ($v_{\rm rel}$ being the velocity of the pebble relative to the protoplanet, typically of order ηv_K).

The second reason that pebble accretion is more efficient than planetesimal accretion is that pebbles drift in the disk. Thus, the orbital neighborhood of the protoplanet cannot become empty. Even if the protoplanet accretes all the pebbles in its vicinity, the local population of pebbles is renewed by particles drifting inward from larger distances. This does not happen for planetesimals because their radial drift in the disk is negligible.

Provided that the mass-flux of pebbles through the disk is large enough, pebble accretion can grow protoplanets from about a Moon-mass up to multiple Earth-masses, i.e. to form the giant planets cores within the disc's lifetime (Lambrechts and Johansen 2012, 2014). The large mass ratio between protoplanets in the outer vs. inner parts of the disc can be explained by remembering that icy pebbles can be relatively large (a few centimeters in size), whereas in the inner disc the pebble's size is limited to sub-millimeter by the bouncing silicate barrier (chondrule-size particles) and by taking into account that pebble accretion is more efficient for large pebbles than for chondrule-size particles (Morbidelli et al. 2015).

For all these reasons, while some factors remain unknown (particularly the pebble flux and its evolution during the disk lifetime), pebble accretion is now considered to the dominant process of planet formation.

An important point is that pebble accretion cannot continue indefinitely. When a planet grows massive enough it starts opening a gap in the disk. This eventually creates a pressure bump at the outer edge of the gap which stops the flux of pebbles. The mass at which this happens is called *pebble isolation mass* (Morbidelli et al. 2012; Lambrechts et al. 2014) and depends on disk's viscosity and scale height (Bitsch et al. 2018). Once a planet reaches the pebble isolation mass, it stops accreting pebbles. Given that it blocks the inward pebble flux, this means that all protoplanets on interior orbits are starved of pebbles, regardless of their masses. Turbulent diffusion can allow some pebbles to pass through the pressure bump (Weber et al. 2018), particularly the smallest ones, because the effects of diffusion are proportional to $\sqrt{\alpha/\tau_s}$.

1.2.4 Orbital Migration of Planets

Once a massive body forms in the disk, it perturbs the distribution of the gas in which it is embedded. We generically denote the perturbing body as a *planet*. In this section we consider planets smaller than a few tens of Earth masses. The case of giant planets will be discussed in the next section.

Analytic and numerical studies have shown that a planet generates a spiral density wave in the disk, as shown in Fig. 1.9 (Goldreich and Tremaine 1979, 1980; Lin and Papaloizou 1979; Ward 1986; Tanaka et al. 2002). The exterior wave trails the planet. The gravitational attraction that the wave exerts on the planet produces a negative torque that slows the planet down. The interior wave leads the planet and exerts a positive torque. The net effect on the planet depends on the balance between these two torques of opposite signs. It was shown by Ward (1986) that for axis-symmetric disks with any power-law radial density profiles, the negative torque exerted by the wave

Fig. 1.9 The spiral density wave launched by a planet in the gas disk. The color brightness is proportional to the gas surface density. Courtesy of F. Masset

in the outer disk wins. This is because a power-law disk is in slight sub-keplerian rotation, so that the gravitational interaction of the planet with a disk's ring located at $a_p + \delta a$ (a_p being the orbital radius of the planet) is stronger than with the ring located at $a_p - \delta a$, given that the relative velocity with the former is smaller. As a consequence of this imbalance, the planet must lose angular momentum and its orbit shrinks: the planet migrates towards the central star. This process is called *Type-I migration*. The planet migration speed is:

$$\frac{\mathrm{d}a}{\mathrm{d}t} \propto M_p \Sigma_g \left(\frac{a}{H}\right)^2, \tag{1.23}$$

where a is the orbital radius of the planet (here assumed to be on a circular orbit), M_p is its mass, Σ_g is the surface density of the gas disk and H is its height at the distance a from the central star. A precise migration formula, function of the power-law index of the density and temperature radial profiles, can be found in Paardekooper et al. (2010, 2011). The planet-disk interaction also damps the planet's orbital eccentricity and inclination if these are initially non-zero. These damping timescales are a factor $(H/a)^2$ smaller than the migration timescale (Tanaka and Ward 2004; Cresswell et al. 2007).

Precise calculations show that an Earth-mass body at 1 au, in a Minimum Mass Solar Nebula ($\Sigma_g = 1700$ g/cm^2) with scale height $H/a = 5\%$, migrates into the star in 200,000 yr. For different planets or different disks, the migration time can be scaled using the relationship reported in Eq. (1.23). So, Lunar- to Mars-mass protoplanets are only mildly affected by Type-I migration because their migration timescales exceed the few Myr lifetime of the gas disk. Conversely, for more massive

planets, migration should be substantial and should bring them close to the star before that the disk disappears.

Planet-disk interactions through the spiral density wave are only part of the story. An important interaction occurs along the planet's orbit due to fluid elements that are forced to do horseshoe-like librations in a frame corotating with the planet. Along these librations, as a fluid element passes from inside the planet's orbit to outside, it receives a positive angular momentum kick and exerts an equivalent but negative kick onto the planet. The opposite happens when a fluid element passes from outside of the planet's orbit to inside. It can be proven (Masset et al. 2006) that, if the radial surface density gradient at the planet's location is proportional to $1/r^{3/2}$ (i.e. the *vortensity* of the disk is constant with radius), the positive and negative kicks cancel out perfectly, and there is no net effect on the planet. But for different radial profiles, there is a net torque on the planet, named the *vortensity-driven corotation torque* (Paardekooper et al. 2010, 2011). If the disk's profile is shallower than $1/r^{3/2}$ this corotation torque is positive and it slows down migration relative to the rate from Eq. (1.23). Moreover, if the disk's radial surface density gradient is positive and sufficiently steep, the corotation torque (positive) can exceed the (negative) torque exerted by the wave and reverse migration (Masset et al. 2006). This implies the existence of a location in the disk—typically near the density maximum—where migration stops, dubbed *planet trap* (Lyra et al. 2010). Positive surface density gradients could exist at the inner edge of the protoplanetary disk, where the disk is truncated by the stellar magnetic torque (Chang et al. 2010), or at transition from the MRI-active to the MRI-inactive parts of the disk (Flock et al. 2017, 2019)—also very close to the central star—or at the inner edge of each ring observed in MHD simulations (see bottom panel of Fig. 1.4). Therefore, there can be several *planet traps* in the disk (Hasegawa and Pudritz 2012; Baillié et al. 2015).

The corotation region can also exert a positive torque on the planet in a region of the disk where the radial temperature gradient is steeper that $1/r$ (Paardekooper and Mellema 2006). This torque is called *entropy-driven corotation torque* (Paardekooper et al. 2010, 2011). Steep temperature gradients exist behind the "bumps" of the disk's aspect ratio that are generated by opacity transitions (Bitsch et al. 2015a). However, because the disk evolves over time towards a passive disk, with a temperature gradient shallower than $1/r$, the outward migration regions generated by the entropy-driven corotation torque exist only temporarily (Bitsch et al. 2015a).

Other torques can act on the planet and affect its migration in specific cases. If the viscosity of the disk is very small, *dynamical torques* are produced as a feedback of planet migration (Paardekooper 2014; Pierens 2015; Pierens and Raymond 2016). The feedback is negative, i.e. it acts to decelerate the migration, if the disk's surface density profile is shallower than $1/r^{3/2}$ and migration is inwards, or if the profile is steeper than $1/r^{3/2}$ and migration is outwards. In the opposite cases, the dynamical torque accelerates the migration.

Low-viscosity disks are also prone to a number of instabilities generating vortices when submitted to the perturbation of a planet. As a result, the migration of the planet can become stochastic, due to the interaction with these variable density structures (McNally et al. 2019).

As it approaches the planet gas is compressed then decompressed so that its temperature first increases then decreases. Because hot gas loses energy by irradiation, the situation is not symmetric and the gas is colder (i.e. denser) after the conjunction with the planet than it was before conjunction. This generates a negative torque (Lega et al. 2014). On the other hand, if a planet is accreting solids, gravitational energy is released as heat. This source of heat modifies the density of the gas in the vicinity of the planet. In some conditions, this *heating torque* can exceed the previous effect, so that the net effect is positive and can even overcome the negative torque exerted by the wave (Benítez-Llambay et al. 2015). This torque, however, also enhances the orbital eccentricity of the planet (Eklund and Masset 2017), which in turn reduces its accretion rate. Thus some self-regulated regime can be achieved (Masset 2017).

Finally, even the steady-state dust distribution can be perturbed by the presence of the planet, acquiring asymmetries that can exert torques on the planet (Benítez-Llambay and Pessah 2018).

To summarize, although the migration of a small-mass planet is typically inward and fast, there can be locations in the disk where migration is halted, as well as a number of temporary mechanisms that can reduce or enhance the migration rate. Therefore, the actual migration of a planet must be investigated in a case-by-case basis and requires a realistic modeling of the disk, given that its density and temperature gradients, opacity, viscosity and dust distribution play a key role. Unfortunately, so far our limited theoretical and observational knowledge of disks hampers our ability to model planet migration quantitatively.

1.2.5 Gas Accretion and Giant Planet Migration

A massive planet immersed in a gas disk can attract gas by gravity and build up an atmosphere. To distinguish between the solid part of the planet from its atmosphere, we will call the formed the *core*.

The closed set of equations that govern the distribution of gas in the atmosphere are:

$$\frac{\mathrm{d}P}{\mathrm{d}r} = \frac{GM(r)\rho(r)}{r}, \tag{1.24}$$

where $\rho(r)$ is the density of the gas at a distance r from the center of the planet, which describes hydrostatic equilibrium (gravity balanced by the internal pressure gradient);

$$\frac{\mathrm{d}M}{\mathrm{d}r} = 4\pi r^2 \rho(r), \tag{1.25}$$

which describes the planet's mass-radius relationship $M(r)$ from $M(r_c) = M_c$, where r_c is the radius of the core and M_c is its mass;

$$\frac{\mathrm{d}T}{\mathrm{d}r} = -\frac{3\kappa L\rho}{64\pi\sigma r^2 T^3}, \tag{1.26}$$

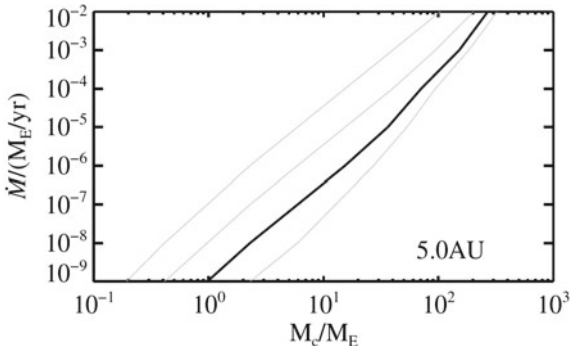

Fig. 1.10 The value of $M_{\rm crit}$ (on the horizontal axis) as a function of core's accretion rate (on the vertical axis), for different values of the opacity—increasing from left to right. The atmosphere can be in hydrostatic equilibrium only if $M_c < M_{\rm crit}$. Figure courtesy of M. Lambrechts, from Lambrechts and Johansen (2014)

where σ is Boltzmann's constant, κ the gas opacity and $L \propto M_c \dot{M}_c / r_c$ is the luminosity of the core, due to the release of the gravitational energy delivered by the accretion of solids at a rate $\dot{M}_c$;

$$P = \frac{\mathcal{R}}{\mu \rho T}, \tag{1.27}$$

which is the equation of state, here for a perfect gas ($\mathcal{R}$ being the perfect gas constant and μ the molecular weight).

One can attempt to solve this set of equations using boundary condition $\rho(r_b) = \rho_0$ and $T(r_b) = T_0$, where ρ_0 and T_0 are the disk's values for gas density and temperature, respectively, and r_b is the disk-planet boundary, typically the Bondi radius $r_b = 2GM/c_s^2$ (c_s being the sound speed). A solution exists only for $M_c < M_{\rm crit}(\kappa, L)$ where $M_{\rm crit}(\kappa, L)$ is a threshold value depending on opacity and luminosity (and disk's properties), as shown in Fig. 1.10 (Piso and Youdin 2014; Lambrechts and Johansen 2014).

$M_{\rm crit}$ tends to zero as the core's accretion rate tends to zero. If $L = 0$, no hydrostatic solution can exist. Recall from the previous section that when a planet reaches the pebble isolation mass the accretion pebbles effectively stops (Morbidelli et al. 2012; Bitsch et al. 2018). This drastically changes the value of L and hence $M_{\rm crit}$. If the atmosphere of the planet was in hydrostatic equilibrium up to that point, it may be out of equilibrium. As a rule of thumb, when M_c approaches $M_{\rm crit}$ the mass of the atmosphere in hydrostatic equilibrium approaches that of the core. This triggers runaway gas accretion (Lambrechts and Johansen 2014).

When the atmosphere is no longer in hydrostatic equilibrium, it contracts under the effect of gravity. The compression of gas releases energy, so the atmosphere can only contract on the Kelvin-Helmoltz timescale, which is effectively the atmosphere's cooling timescale through irradiation. As the atmosphere contracts, new gas can be captured within the Bondi radius r_b. This increases the mass of the atmosphere and hence the gravity of the full planet. This triggers a positive feedback on the accretion

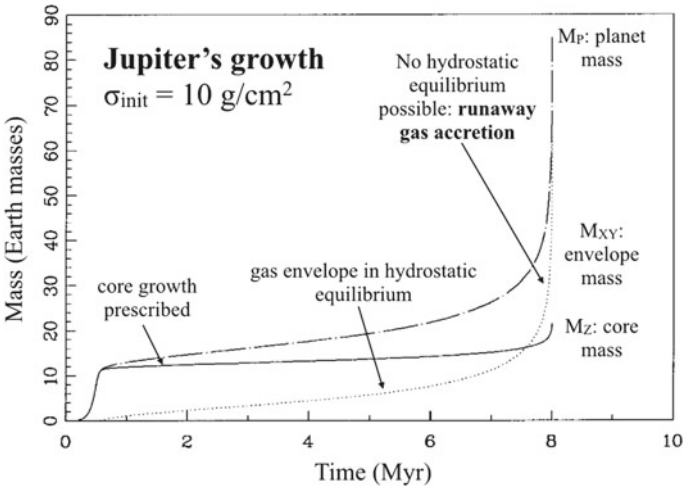

Fig. 1.11 Runaway growth of a giant planet near Jupiter's orbital radius. The solid curve shows the mass of the solid core, the dotted curve the mass of the atmosphere and the dashed curve the total mass of the planet. Here the accretion of solids onto the core is prescribed according to a now obsolete planetesimal accretion model. The approximate boundary in time between the hydrostatic regime and the runaway regime is at ∼7.5 Myr. While the runaway gas accretion regime is not in hydrostatic equilibrium it can be modeled as a series of equilibrium states. Adapted from Pollack et al. (1996)

rate, so that the mass of the planet's atmosphere increases exponentially with time (see Fig. 1.11) (Pollack et al. 1996; Hubickyj et al. 2005; Lissauer et al. 2009) .

A number of studies have modeled atmospheric accretion during the runaway phase (Ikoma et al. 2000; Coleman et al. 2017; Lambrechts et al. 2019b) using different approaches. All have confirmed the runaway gas accretion with a mass-doubling timescales for Jupiter-mass planets of order 10^4-10^5 yr in a MMSN disk. This raises the question of why Saturn-mass exoplanets outnumber Jupiter-mass ones, which drastically outnumber super-Jupiters (Butler et al. 2006; Udry et al. 2007). One possibility is that giant planets enter in their runaway phase late, as the disk is disappearing (Pollack et al. 1996; Bitsch et al. 2015b). Given that the mass doubling timescale in the runaway phase is so much shorter than the disk's lifetime, this appears to be a surprising coincidence. The other possibility is that the growth of a planet is limited by the ability of the disk to transport gas radially. We know from observations, however, that the gas accretion rate onto the central star is typically of the order of $10^{-8}\ M_\odot$/yr (Hartmann et al. 1998), which means that a Jupiter-mass of gas passes through the orbit of a giant planet in only 10^5 yr, again much shorter than the disk's lifetime. Perhaps the study of giant planet growth in low-viscosity disks dominated by winds can bring a solution to the problem, given the different geometry and mechanism of transport for the accreting gas relative to a classic, viscous disk.

1.2.5.1 Gap Opening and Type-II Migration

As we have seen in Sect. 1.2.4, a planet embedded in a disk exerts a positive torque on the outer part of the disk and a negative torque on the inner part. The torque is proportional to the planet's mass. If the planet is small, its torque is easily overcome by the viscous torque that the annuli of the disk exert on each other. The global surface density profile of the disk is not changed and only the spiral density wave appears. But if the planet is massive enough the torque it exerts on the disk overwhelms the disk's viscous torque. In this case, the planet effectively pushes gas away from its orbit: outer gas outwards and inner gas inwards. A gap opens in the gas distribution around the orbit of the planet.

As gas is removed, the gap becomes deeper and wider. But as the gradients of the disk's surface density distribution become steeper at the edges of the gap, the disk's viscous torque is enhanced. In fact, the viscous torque acting on elementary rings can be computed by differentiation of Eq. (1.3) to give:

$$\delta T_\nu = -\frac{3}{2}\nu\Omega\left[\frac{r}{\Sigma}\frac{\mathrm{d}\Sigma}{\mathrm{d}r} + \frac{1}{2}\right](2\pi r\Sigma). \tag{1.28}$$

Once the density gradient becomes steep enough, the viscous torque balances the torque that the planet exerts on the same annulus of the disk (Varnière et al. 2004).

The depth of a gap—defined as the ratio between the surface density of the disk perturbed by the planet Σ_p and the original value Σ_u—is (Kanagawa et al. 2018):

$$\frac{\Sigma_p}{\Sigma_u} = \frac{1}{1+0.04K}, \tag{1.29}$$

where

$$K = \left(\frac{M_p}{M_\star}\right)^2 \left(\frac{H}{r}\right)^{-5} \alpha^{-1} \tag{1.30}$$

and M_p, $M_\star$ are the masses of the planet and the star, respectively, the aspect ratio of the disk H/r is taken at the planet's location, and as usual $\alpha = \nu/(H^2\Omega)$. This formula holds up to $K \sim 10^4$ (see Fig. 11 in Kanagawa et al. 2018). However, it cannot hold indefinitely, in particular in the limit of low α. This is because, if the density gradients at the edges of the gap become too steep, the rotational properties of the gas change so much under the effect of the pressure gradient that the specific angular momentum of the disk $r^2\Omega(r)$ is no-longer a growing function of r (Kanagawa et al. 2015). When this happens the disk becomes Rayleigh unstable and develops local turbulence, in turn enhancing the local viscosity. This effectively limits the steepness of the gap "walls" and the depth of the gap. Because the pressure gradient is also proportional to $(H/r)^2$, this narrative implies that, in the limit of vanishing viscosity, the denser the disk the shallower the gap. Thus, a gap opening criterion—i.e. the minimal mass of a planet to cause a depletion of 90% of the gas in the gap—must depend not only on viscosity but also on the disk's aspect ratio. An

often-quoted criterion is the following:

$$\frac{3}{4}\frac{H}{R_H} + \frac{50}{qR_e} < 1, \tag{1.31}$$

where $q = M_p/M_\star$, $R_H = (q/3)^{1/3}$ and $R_e = r_p^2\Omega_p/\nu$ (Crida et al. 2006).

The formation of a gap profoundly changes a planet's migration. This migration mode has been dubbed *Type-II migration*. The gap must migrate along with the planet. In particular, as the planet moves inwards, the disk has to refill the portion of the gap "left behind" by the planet's radial motion. Because the radial velocity of the gas in a viscous unperturbed disk is $v_r = -(3/2)\nu/r$, this was the expected migration speed of the planet, independent of the planet's mass and disk's scale aspect ratio (Ward 1997).

However, the planet's migration rate is not so simple (Duffell et al. 2014; Dürmann and Kley 2015). It depends on the ratio between the disk's density and the mass of the planet, exemplified by the dimensionless ratio $r_p^2\Sigma/M_p$ (see Fig. 1.12), and also on the disk's aspect ratio. Depending on these quantities, the radial velocity of the planet can be smaller or larger than the "idealized" Type-II migration speed of $-(3/2)\nu/r$.

It is easy to understand that a planet's migration speed is slower than the idealized speed for the case of a low disk mass. A light disk obviously cannot push a heavy planet. This is the inertial limit: the planet is an obstacle to the flow of the gas. But how can a planet migrate faster than the radial speed of the gas? In principle the gas should remain behind and the planet, losing contact from the outer disk, should feel a weaker negative torque, eventually slowing down its migration until it moves at the same speed of the gas. The explanation given by Duffell et al. (2014) and Dürmann and Kley (2015) was that, as the planet migrates inwards, the gas from the inner disk can pass through the gap, refilling the left-behind part of the gap. In this way, the planet does not have to wait for the gas to drift-in at viscous speed. But the passage of gas through the gap is insignificant if the gap is significantly wider than the planet's horseshoe region (Robert et al. 2018), which is the case for massive planets in low-viscosity disks. In that case, as the planet moves inwards, the gap must be refilled from the outer disk. However, the steep density gradient at the edge of the gap enhances the viscous torque, as discussed above, so that the gas radial speed can be several times faster than $-(3/2)\nu/r$. This explains why the planet can exceed the idealized Type-II migration rate. Nevertheless, the migration rate of the planet must linearly proportional to the viscosity of the disk (Robert et al. 2018).

The dependence of the migration rate of giant planets on disk's viscosity opens the possibility that, in low-viscosity disks, the migration timescale can exceed the disk's lifetime. This would be convenient to explain why most giant planets are warm/cold Jupiters and not hot Jupiters[3] (Butler et al. 2006; Udry et al. 2007). However, recall

[3] We define a hot Jupiter as a giant planet within 0.1 au from its star and warm/cold Jupiters as those that are beyond 0.5 au. Very few giant planets fall between 0.1 and 0.5 au so the exact values of these boundaries are not important. Debiased observations suggest that hot Jupiters are about 1/10th or less as abundant as warm/cold Jupiters (Fernandes et al. 2019; Wittenmyer et al. 2016, 2020).

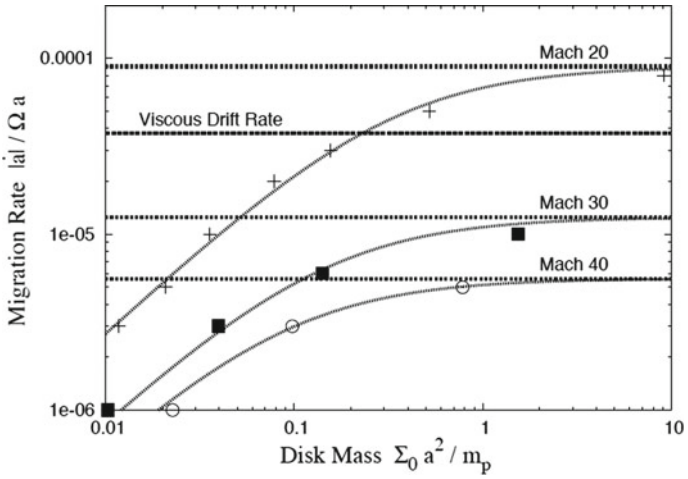

Fig. 1.12 The migration rate as a function of the ratio $r_p^2\Sigma/M_p$ for a giant planet in a disk with $\alpha = 3 \times 10^{-3}$, for three different disk's aspect ratios. Notice that the migration rate can be smaller or larger than the viscous drift rate of the gas, i.e. the idealized Type-II migration speed. Figure courtesy of P. C. Duffell, from From Duffell et al. (2014)

from Sect. 1.2.1.1 that low-viscosity disks cannot explain the accretion rates observed for the central stars. If viscosity is low, there must be some additional mechanism for the radial transport of gas, possibly induced by angular momentum removal in disk winds. The migration rate of giant planets in these kind of disks has not yet been studied.

1.2.6 Resonance Trapping During Planet Migration

Numerical simulations show that multiple planets migrating in a disk have the tendency to lock into mutual mean motion resonance, where the period ratio is very close to the ratio of integer numbers (Terquem and Papaloizou 2007; Pierens and Nelson 2008; Izidoro et al. 2017). Typically, these numbers differ by just one such that the period ratios are 2:1, 3:2, 4:3 etc. These are called *first-order* resonances.

To understand this propensity to form resonant chains we need to dive into the complex world of dynamical planet-planet interactions. To stay simple, we will consider the planar three body problem, where two planets orbit a star on coplanar orbits. This is the simplest example of dynamics of a planetary system, yet it already captures most of the complexities of real systems. The best mathematicians made huge efforts to find an analytic solution of this problem, until Poincaré (1892) demonstrated that this was impossible. A general analytic solution does not exist. The system can exhibit chaotic behavior (Henon and Heiles 1964). Yet, some description

can be provided, such as for instance for the dynamics of resonant planets with small libration amplitude, which is that of interest to understand the formation of resonant chains. This is what we attempt to do in this section.

To study the three body problem, the most effective approach is to use the Hamiltonian formalism. A system of first-order differential equations

$$\frac{\mathrm{d}\mathbf{x}}{\mathrm{d}t} = \mathbf{f}(\mathbf{x}, \mathbf{y}), \quad \frac{\mathrm{d}\mathbf{y}}{\mathrm{d}t} = \mathbf{g}(\mathbf{x}, \mathbf{y}) \tag{1.32}$$

is said to be in Hamiltonian forms, if there exists a scalar function $\mathcal{H}(\mathbf{x}, \mathbf{y})$ such as

$$f_i(\mathbf{x}, \mathbf{y}) = \frac{\partial \mathcal{H}}{\partial y_i}, \quad g_i(\mathbf{x}, \mathbf{y}) = -\frac{\partial \mathcal{H}}{\partial x_i}, \tag{1.33}$$

for each component $i = 1, \ldots, N$ of the vectors $\mathbf{x}, \mathbf{y}, \mathbf{f}, \mathbf{g}$. The function $\mathcal{H}$ is called the *Hamiltonian* of the problem; $\mathbf{x}$ is called the vector of *coordinates* and $\mathbf{y}$ the vector of *momenta*. If H is periodic on $\mathbf{x}$, the coordinates are also called *angles* and the momenta *actions*.

An important property of Hamiltonian dynamics is that $\mathcal{H}$ is constant over the flow $\mathbf{x}(t), \mathbf{y}(t)$ that is solution of the equations of motion. This means that, in the special case where $\mathcal{H}$ is a function of only one component of $\mathbf{x}$, namely $\mathcal{H} \equiv \mathcal{H}(x_1, \mathbf{y})$, the evolution of the system can be easily computed: $y_2, \ldots, y_N$ are constant of motion from (1.32) and (1.33); the motion of x_1, y_1 can be obtained from the level curve of $\mathcal{H}(x_1, y_1, y_2, \ldots, y_N) = \mathcal{H}(\mathbf{x}(0), \mathbf{y}(0))$, which is a 1D curve in a 2D x_1, y_1 space (called *phase space*). In this case, the problem is integrable (i.e. the solution is provided with analytic functions of time).

In studying a problem written in Hamiltonian form, a typical goal is to find a transformation of variables $\mathbf{x} \to \mathbf{x}', \mathbf{y} \to \mathbf{y}'$ that transforms the Hamiltonian function into one that is independent of $x_2', \ldots, x_N'$. However, only transformations that preserve the form of Hamilton equations (Eqs. 1.32 and 1.33), called *canonical transformations*, are allowed. There are many forms of canonical transformations. In this section we will use only linear transformations $\mathbf{x}' = A\mathbf{x}, \mathbf{y}' = B\mathbf{y}$ where A, B are $N \times N$ matrices. It can be proven that the transformation is canonical if and only if

$$B = \left[A^{-1}\right]^T. \tag{1.34}$$

In general, it is not possible to find a canonical transformation that makes the Hamiltonian independent of $N - 1$ coordinates. Then, a goal in *perturbation theory* is to find a canonical transformation that turns $\mathcal{H}(\mathbf{x}, \mathbf{y})$ into

$$\mathcal{H}'(\mathbf{x}', \mathbf{y}') = \mathcal{H}_0'(x_1', \mathbf{y}') + \epsilon \mathcal{H}_1'(\mathbf{x}', \mathbf{y}'). \tag{1.35}$$

In this case $\mathcal{H}_0'$ is called the *integrable approximation* and $\mathcal{H}_1'$ the *perturbation*. The latter can be neglected if one is interested in the dynamics up to a time $t < 1/\epsilon$. Depending on the goal in terms of accuracy, ϵ has to be sufficiently small.

After this broad and shallow introduction to Hamiltonian dynamics, let's turn to the planar three-body problem. The problem admits a Hamiltonian description, with Hamiltonian function:

$$\mathcal{H} = \sum_{j=1,2} \frac{\|\mathbf{p}_j\|^2}{2\mu_j} - \frac{G(M_\star + m_j)\mu_j}{\|\mathbf{r}_j\|} + \frac{\mathbf{p}_1.\mathbf{p}_2}{M_\star} - \frac{Gm_1m_2}{\|\Delta\|}, \tag{1.36}$$

where $\mathbf{r}_j$ is the *heliocentric* position vector of planet j of reduced mass $\mu_j = m_j M_\star/(m_j + M_\star)$, $\mathbf{p}_j = m_j \mathbf{v}_j$, with $\mathbf{v}_j$ being the *barycentric* velocity vector (not a typo!: positions and velocities have to be taken in different reference frames if one wants a Hamiltonian description of the problem; Poincaré 1897) and $\mathbf{\Delta} = \mathbf{r}_1 - \mathbf{r}_2$.

Using the canonical Delaunay variables:

$$\begin{aligned} \Lambda_j &= \mu_j \sqrt{G(M_\star + m_j)a_j}, \quad \lambda_j = M_j + \varpi_j \\ \Gamma_j &= \Lambda_j(1 - \sqrt{1 - e_j^2}), \qquad \gamma_j = -\varpi_j \end{aligned}$$

where a_j, e_j are the semi major axes and eccentricities, ϖ_j are the perihelion longitudes, M_j the mean anomalies and G is the gravitational constant, the Hamiltonian (Eq. 1.36) becomes:

$$\mathcal{H} = -G^2 \sum_{j=1,2} \frac{\mu_j^3 (M_\star + m_j)^2}{2\Lambda_j^2} + \mathcal{H}_1(\Lambda_{1,2}, \Gamma_{1,2}, \lambda_{1,2}, \gamma_{1,2}). \tag{1.37}$$

The first term in the r.h.s. of Eq. (1.37), denoted $\mathcal{K}$ hereafter, taken alone, is an integrable Hamiltonian, but the flow that it describes is trivially that of two uncoupled Keplerian motions: the actions $\Lambda_{1,2}$, $\Gamma_{1,2}$ are constant, the longitude of perihelia $\gamma_{1,2}$ are constants, and only the mean longitudes $\lambda_{1,2}$ move with constant frequency $G^2\mu_j^3(M_\star + m_j)^2/\Lambda_j^3 = \sqrt{G(M_\star + m_j)/a_j^3}$. So, this kind of integrable approximation of the full Hamiltonian is not sufficient for our purposes and we need to find a better one.

To this end, we expand $\mathcal{H}_1$ in power series of $\sqrt{\Gamma_j} \sim \sqrt{\Lambda_j/2}e_j$ and in Fourier series of the angles λ_j, γ_j. The general form is therefore

$$\begin{aligned} \mathcal{H}_1 = \sum_{l_1,l_2,k_1,k_2,j_1,j_2} & c_{l_1,l_2,k_1,k_2,j_1,j_2}(\Lambda_1, \Lambda_2)\Gamma_1^{j_1/2}\Gamma_2^{j_2/2}\cos(k_1\lambda_1 + k_2\lambda_2 + l_1\gamma_1, l_2\gamma_2) \\ & + s_{l_1,l_2,k_1,k_2,j_1,j_2}(\Lambda_1, \Lambda_2)\Gamma_1^{j_1/2}\Gamma_2^{j_2/2}\sin(k_1\lambda_1 + k_2\lambda_2 + l_1\gamma_1, l_2\gamma_2) \end{aligned} \tag{1.38}$$

The so-called *D'Alembert rules* give us information on which terms of this series can have non-zero coefficients, namely:

- only the c coefficients can be non-zero, because the Hamiltonian must be invariant for a change of sign of all angles (measuring angles clockwise or counter-clockwise is arbitrary), so that the Fourier expansion can contain only cos terms;

- only the $c_{l_1,l_2,k_1,k_2,j_1,j_2}$ coefficients with $k_1 + k_2 - l_1 - l_2 = 0$ can be non-zero, because the Hamiltonian has to be invariant by a rotation of the reference frame, namely increasing all angles by an arbitrary phase δ_0 (remember that $\gamma = -\varpi$, so if all orbital angles are increased by δ_0, γ is decreased by δ_0);
- only the $c_{l_1,l_2,k_1,k_2,j_1,j_2}$ coefficients with $j_1 = |l_1| + 2n$ and $j_2 = |l_2| + 2i$ (with n and i non-negative integer numbers) can be non-zero. This is because the Hamiltonian is not singular for circular orbits (i.e. $\Gamma_1 = 0$ and/or $\Gamma_2 = 0$) so that it has become a polynomial expression in the canonical variables $p_1 = \sqrt{2\Gamma_1}\cos\gamma_1$, $q_1 = \sqrt{2\Gamma_1}\sin\gamma_1$, $p_2 = \sqrt{2\Gamma_2}\cos\gamma_2$, $q_2 = \sqrt{2\Gamma_2}\sin\gamma_2$.

If we are interested in two planets near a mean motion resonance where $P_2 \sim k/(k-1)P_1$, where P_1 and P_2 are the orbital periods and k is a positive integer number, the angle $k\lambda_2 - (k-1)\lambda_1$ will have an almost null time-derivative (as one can see remembering that $\dot{\lambda} = 2\pi/P$ and using the relationship between the orbital periods written above). Thus, it is a slow angle, whereas both λ_1 and λ_2 are fast angles, as it is their difference. To highlight this difference in timescales, let us define new angles:

$$\delta\lambda = \lambda_1 - \lambda_2, \quad \theta = k\lambda_2 - (k-1)\lambda_1. \tag{1.39}$$

Using the rule (1.34), this linear transformation of the angles can be made canonical by changing the actions as:

$$\Delta\lambda = k\Lambda_1 + (k-1)\Lambda_2, \quad \Theta = \Lambda_1 + \Lambda_2, \tag{1.40}$$

so that $(\Delta\lambda, \delta\lambda)$ and (Θ, θ) are pairs of canonical action-angle variables.

Since we are interested in the long-term evolution of the dynamics, we can average the Hamiltonian over $\delta\lambda$, which means that the averaged Hamiltonian will be independent of this angle and, consequently, $\Delta\lambda$ will be a constant of motion. Because the units of semi-major axis are arbitrary, one can always chose them so that $\Delta\lambda = 1$. In other words, changing the values of $\Delta\lambda$ does not change the dynamics; it simply changes the unit of measure of the semi major axes.

Using the D'Alembert rules described above, the function in Eq. (1.38) takes the form

$$\mathcal{H}_1 = \sum_{m,n,i>0,j>0} d_{m,n,i,j}(\Theta, \Delta\lambda)\Gamma_1^{|n-m|/2+j}\Gamma_2^{|m|/2+i}\cos[n(\theta+\gamma_1) + m(\gamma_2 - \gamma_1)], \tag{1.41}$$

where the coefficients $d_{m,n,i,j}$ come from the original coefficients $c_{l_1,l_2,k_1,k_2,j_1,j_2}$ through a simple index algebra that follows trivially from the redefinition of the angles (Eq. 1.39).

Because there are only two possible combinations of angles in the harmonics of Eq. (1.41), it is convenient to identify each of them with a single angle, namely:

$$\psi_1 = \theta + \gamma_1 \quad \delta\gamma = \gamma_2 - \gamma_1, \quad \gamma_2' = \gamma_2\,. \tag{1.42}$$

Again, using the rule (Eq. 1.34) this linear transformation of the angles can be made canonical by changing the actions as:

$$\Psi_1 = \Theta, \quad \Psi_2 = \Theta - \Gamma_1, \quad \mathcal{L} = \Gamma_1 + \Gamma_2 - \Theta\,. \tag{1.43}$$

Now, the Hamiltonian $\mathcal{K} + \mathcal{H}_1$ depends only on the angles ψ_1 and $\delta\gamma$, and $\mathcal{L}$ is a new constant of motion (related to the angular momentum of the system).

This Hamiltonian is still not integrable, because it depends on two angles. An integrable approximation (dependent on only one angle) can be obtained if one retains in Eq. (1.41) only the terms linear in the planets' eccentricities, i.e. proportional to $\sqrt{\Gamma_{1,2}}$, and doing some cumbersome change of variables (Sessin and Ferraz-Mello 1984; Batygin and Morbidelli 2013). In this case one can then trace global dynamical diagrams by plotting the level curves of the Hamiltonian (see for instance Fig. 3 in Batygin and Morbidelli 2013). However, even in the general non-integrable case one can look for the stable equilibrium points in $(\Psi_1, \psi_1, \Psi_2, \delta\gamma)$ as a function of $\mathcal{L}$ (recall that $\Delta\lambda$ can be fixed to unity). The locus of equilibrium points, once transformed back into the original orbital elements, describes a curve in $e_2, a_2/a_1$ or, equivalently, $e_1, a_2/a_1$, like that shown in Fig. 1.13. Note that on the curve $a_2/a_1 \to \infty$ as $e_1 \to 0$, $e_2 \to 0$. This feature comes from the fact that, from Hamilton's equations $\dot{\gamma}_{1,2} = \partial\mathcal{H}/\partial\Gamma_{1,2}$ applied to (1.41), one has $\dot{\gamma}_{1,2} \propto \Gamma_{1,2}^{-1/2}$, i.e. $\dot{\gamma}_{1,2} \to \infty$ as $\Gamma_{1,2} \propto e_{1,2}^2 \to 0$. Thus, to have the equilibrium $\dot{\psi}_1 = 0$ the value of $\dot{\theta}$ has to diverge, which means that a_2/a_1 has to diverge as well.

This feature of the curve of equilibrium points is the key to understand resonant capture. If the planets are far from resonance (i.e. a_2/a_1 is much larger than the resonant ratio assuming Keplerian motion; a 3:2 resonance being located at $a_2/a_1 = 1.3103$ in Fig. 1.13), the protoplanetary disk exerts damping forces on their eccentricities, so that the planet's orbits are basically circular. This means, from the shape of the curve of equilibrium points, that the planets will be on the equilibrium. As migration proceeds and a_2 approaches a_1 (this is the case if the outer planet migrates faster towards to the star, which happens in Type-I migration if it is more massive or if the inner planet is blocked at a planet trap), the ratio a_2/a_1 decreases. If this happens slowly compared to the libration period around the equilibrium point, the dynamical evolution has to react *adiabatically* (Neishtadt 1984). This means that the amplitude of libration around the equilibrium point has to be conserved. Because initially the planets have vanishing amplitude of libration (their eccentricities are basically null as those characterizing the equilibrium point), this means that the planets have to evolve from one equilibrium point to the other, i.e. they have to follow the curve traced in Fig. 1.13. As a_2/a_1 asymptotically approaches the Keplerian resonant value, the eccentricities of the two planets increase.

If the convergent migration is too fast, the adiabatic condition is broken. The amplitude of libration is not conserved. The planets can jump off resonance and continue to approach each other more closely. But, because the libration frequency of a resonance $P_2 \sim k/(k-1)\,P_1$ increases with k, eventually the planets will find a resonance with k large enough and libration frequencies fast enough that the adiabatic

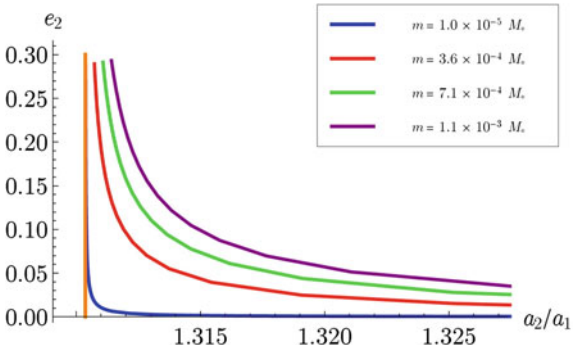

Fig. 1.13 The locus of equilibrium points for the 3:2 mean motion resonance in the plane e_2 versus a_2/a_1, for different planetary masses (here assumed to be equal to each other) in different colors. The vertical orange line shows the location of the resonance in the Keplerian approximation (the same a_2/a_1 for any eccentricity because the orbital frequencies depends only on semi major axes). Adapted from Pichierri et al. (2018)

condition is satisfied. Then, they will be trapped in resonance. In essence, the faster is the convergent migration, the higher the index k of the resonance in which the planets will be trapped. But trapping always occurs, eventually. These arguments apply for each pair of neighboring planets in a multi-planet system. This is why the formation of configurations in resonant chains is a typical outcome of planet migration.

If the adiabatic condition is satisfied, is resonant trapping stable? Fig. 1.13 suggests that the eccentricities of the planets should grow indefinitely. But in reality the disk exerts eccentricity damping, so that the eccentricities grow until an equilibrium is established between the eccentricity damping from the disk and the resonant conversion of convergent migration into eccentricity pumping. A precise formula to compute this equilibrium in a variety of configurations (damping exerted on both planets or only on one, inner planet at a planet-trap or not etc.) can be found in the appendix of Pichierri et al. (2018). The equilibrium eccentricity is typically of order $(H/r)^2$, where (H/r) is the aspect ratio of the protoplanetary disk.

There is a complication. For the adiabatic principle to be applied, the dissipative forces have to act on the parameters of the Hamiltonian, not on the dynamical variables. This is the case for migration. The change in semi-major axis ratio changes the otherwise constant of motion $\mathcal{L}$, i.e. a parameter of the Hamiltonian. But the eccentricity damping affects $\Gamma_{1,2}$, i.e. dynamical variables. Then, the equilibrium point can become a focus, which means that the dynamical evolution spirals around it. The spiral can be inward if the focus is stable (which means that any initial amplitude of libration would shrink to 0) or outwards if the focus is unstable (which means that the amplitude of libration grows indefinitely, even if it is initially arbitrarily small). This unstable evolution, first pointed out by Goldreich and Schlichting (2014), is called *overstability*.

Figure 1.14 shows a summary of the most detailed investigation of the stability/overstability of a resonance in presence of eccentricity damping (Deck and Baty-

gin 2015). If the eccentricity damping is proportional to the planetary masses (as in the case where both planets are embedded in the disk), for the 3:2 and higher-k resonances the resonant configuration is stable whenever $m_1 > m_2$. In the opposite case, the stability/overstability depends on the total mass ratio $\epsilon_p = (m_1 + m_2)/M_\star$. There is a limit value of the ratio m_1/m_2 below which the system is overstable, and this ratio decreases with increasing ϵ_p (Fig. 1.14a). For the 2:1 resonance the situation is qualitatively similar, but the planets can be overstable even if $m_1/m_2 > 1$ if ϵ_p is small enough (Fig. 1.14b). On the other hand, if there is no eccentricity damping on the inner planet ($\tau_{e_1} \to \infty$, which happens if the inner planet has been pushed into a disk's cavity), the resonant configuration is always stable for any m_1/m_2 ratio.

Even if resonant planets are not in the overstable regime, they may be unstable because of other processes. Due to their proximity and eccentric orbits they may approach each other too much over their resonant trajectories and be destabilized by a close-encounter (Pichierri et al. 2018). There can also be subtle secondary resonances between a combination of the libration frequencies and the synodic frequency $\dot{\lambda}_1 - \dot{\lambda}_2$. These secondary resonances cannot be described with the averaged Hamiltonian (Eq. 1.41) because the terms in $\lambda_1 - \lambda_2$ have been removed by the averaging procedure. But they can be studied following a more precise and convoluted approach. As the number of planets in a resonant chain increases, the number of libration frequencies increases as well and therefore a richer set of combined frequencies is possible. This explains, at least at the qualitative level, why long resonant chains are more fragile than short chains, as observed in numerical simulations (Matsumoto et al. 2012; Cossou et al. 2013). The long-term evolution of multi-planet resonant chains remains nevertheless an active area of research in celestial mechanics.

1.3 Global Models of Planet Formation

Building global models of planet formation is akin to putting together a puzzle. We have a vague picture of what the puzzle should look like (i.e., from exoplanet demographics) but observational biases cloud our view. Moreover, the puzzle pieces—the planet formation mechanisms—often change in number and in shape. The puzzle-builders must constantly have an eye both on the evolution of the big picture and on the set of viable puzzle pieces. One must not hesitate to discard a model when it no longer serves.

We will describe our current best global models for the origin of super-Earth systems (Sect. 1.3.1), giant planet systems (Sect. 1.3.2) and our own Solar System (Sect. 1.3.3). Then we will look at how water may be delivered to rocky planets (Sect. 1.3.4).

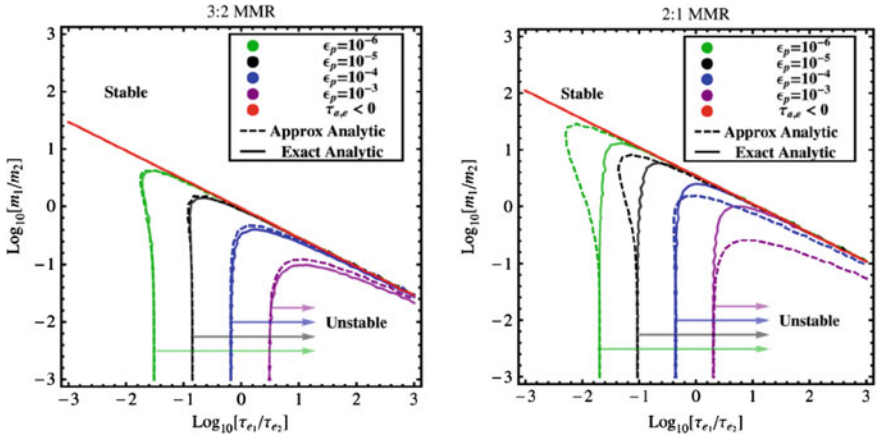

Fig. 1.14 Each plot shows the region of the parameter plane τ_{e_1}/τ_{e_2} and m_1/m_2, where $\tau_{e_{1,2}}$ is the damping timescale of the eccentricity of planets 1 and 2, respectively, with masses m_1 and m_2, for different planetary masses $\epsilon_p = (m_1 + m_2)/M_\star$. The left plot is for the 3:2 resonance, the right plot for the 2:1 resonance. For a planet of mass m at semi-major axis a the eccentricity damping timescale is $\tau_e \propto (H/a)^4/(m\Sigma\sqrt{a})$, where Σ is the surface density of the disk and H/a its aspect ratio. Thus, if the disk has a constant aspect ratio and $\Sigma \propto 1/\sqrt{a}$ the system should place on the dashed diagonal line (i.e. $m_1/m_2 = tau_{e_1}/tau_{e_2}$). This shows, for instance, that a 3:2 system is stable if $m_1 < m_2$. If instead the inner planet is in a low-density region (i.e. a disk's cavity), $\tau_{e_1} \to \infty$ and therefore the system is stable for all mass ratios. Adapted from Deck and Batygin (2015)

1.3.1 Origin of Close-in Super-Earths

The key properties of super-Earth systems that must be matched by any formation model can be very simply summarized as follows (we refer the reader to Chap. 3 for detailed reviews):

- A large fraction (roughly one third to one half) of stars have close-in super-Earths (with periods shorter than 100 days; Fressin et al. 2013; Mulders et al. 2018), but many (perhaps most) of them do not.
- Most super-Earth systems only have a single planet detected in transit, whereas a fraction of systems is found with many planets in transit (Lissauer et al. 2011; Fang and Margot 2012; Tremaine and Dong 2012).
- In multi-planet systems, pairs of neighboring super-Earths are rarely found to be in mean motion resonance (Lissauer et al. 2011; Fabrycky et al. 2014).
- The masses of super-Earths extend from Earth to Neptune, with a preference for a few $M_\oplus$ (Weiss et al. 2013; Marcy et al. 2014; Wolfgang et al. 2016; Chen and Kipping 2017).

Models for the formation of super-Earths were developed before they were even discovered (Raymond et al. 2008a). While certain models have been refined in recent years, only a single new model has been developed.

In-situ accretion is the most intuitive and simplest model for super-Earth formation, yet it has a fatal flaw. That model proposes that super-Earths simply accreted from local material very close to their stars in a similar fashion to the classical model of terrestrial planet formation in the Solar System (see Sect. 1.3.3.1 below). In-situ accretion was proposed in 2008 (Raymond et al. 2008a) and discarded because the masses implied in the innermost parts of disks seemed prohibitively large. In 2013 this idea was revisited by Chiang and Laughlin (2013), who used the population of known super-Earths to generate a "minimum-mass extrasolar nebula" representing a possible precursor disk that would have formed the population of super-Earths. The high masses inferred in inner disks conflicts with measurements, but those measurements are only of the outermost parts of disks (Williams and Cieza 2011). While it is possible to imagine that inner disks can pile up material, there is a simply-understood timescale problem. With very high densities in the inner disk, the growth timescale for super-Earths is extremely fast (Lissauer and Stevenson 2007; Raymond et al. 2007b; Raymond and Cossou 2014; Inamdar and Schlichting 2015; Schlichting 2014; Ogihara et al. 2015). In fact, the growth timescales are so fast and the requisite disks so massive that migration is simply unavoidable (Ogihara et al. 2015). Even aerodynamic drag is strong enough to cause rapid orbital drift (Inamdar and Schlichting 2015). Thus, we cannot consider the planets to have formed in-situ because they must have migrated and their final orbits cannot represent their starting ones. Nonetheless, it has been shown that if the right conditions were to arise, with the requisite amount of solid material close to the star, accretion should indeed produce planetary systems similar to the observed super-Earths (Hansen and Murray 2012, 2013; Dawson et al. 2015, 2016; Moriarty and Ballard 2016; Lee et al. 2014; Lee and Chiang 2016, 2017).

A number of the first processes to be explored for forming super-Earths relied on giant planets. For example, migrating giant planets can shepherd material interior to their orbits and stimulate the growth of super-Earths (Zhou et al. 2005; Fogg and Nelson 2005, 2007; Raymond et al. 2006b; Mandell et al. 2007). Moving secular resonances driven by giant planet interactions can do the same (Zhou et al. 2005). However, these models have been ruled out as the main formation pathways for super-Earths, because most super-Earth systems do not appear to have an associated giant planet (although testing the correlation between super-Earths and outer gas giants is an active area of study, e.g. Zhu and Wu 2018; Barbato et al. 2018; Bryan et al. 2019).

The migration model has proven quite successful model in reproducing the observed population of super-Earths (Terquem and Papaloizou 2007; Ogihara and Ida 2009; McNeil and Nelson 2010; Ida and Lin 2010; Cossou et al. 2014; Izidoro et al. 2017, 2019; Raymond et al. 2018b; Carrera et al. 2018). In that model, large planetary embryos grow throughout the disk and migrate inward, driven by the gaseous disk (Fig. 1.15 shows an example of a simulation of the migration model). It is natural to think that embryos would form first past the snow line, where pebble accretion is thought to be more efficient (see Sect. 1.2.3 and Morbidelli et al. 2015). However, it is also possible that in some disks large embryos can form very close to their stars. This might occur if inward-drifting pebbles are concentrated at a pressure bump, perhaps

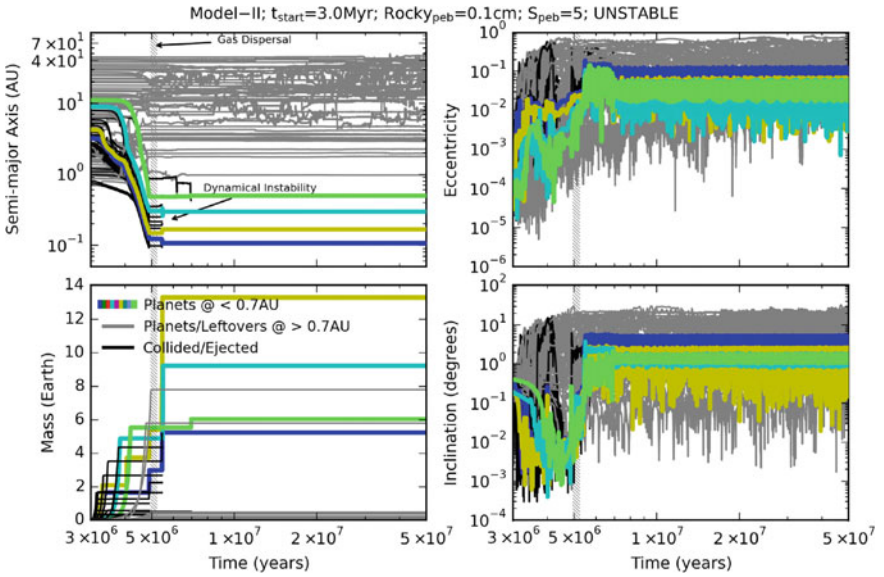

Fig. 1.15 Evolution of a simulation of the *breaking the chains* migration model for the origin of close-in super-Earths. The panels show the evolution of a population of ∼lunar-mass planetary embryos that grow by accreting pebbles, migrate inward and form a resonant chain anchored at the inner edge of the disk. The resonant chain is destabilized shortly after the dissipation of the gaseous disk, leading to a late phase of scattering and collisions that spreads out the planets and increases their eccentricities and inclinations. Figure courtesy of A. Izidoro, from Izidoro et al. (2019)

associated with the inner edge of a dead zone[4] (Chatterjee et al. 2014, 2015). While the migration rate and direction depends on the disk model (Lyra et al. 2010; Kretke and Lin 2012; Bitsch et al. 2013, 2014), inward migration is generally favored. The inner edge of the disk creates a strong positive torque (Flock et al. 2019) that acts to trap any inward-migrating embryo (Masset et al. 2006). This leads to a convergence of bodies near the disk's inner edge. Convergent migration leads to resonant trapping (see Sect. 1.2.6) and tends to produce planets in long chains of resonances. Of course, the observed super-Earths are not found in resonance. However, most resonant chains become dynamically unstable as the gaseous disk dissipates. This leads to a phase of giant collisions between embryos that is quite similar to that simulated by studies that ignored the migration phase and invoked a large population of embryos in a dissipating gaseous disk (Hansen and Murray 2012, 2013; Dawson et al. 2015). The instability phase leads to scattering among embryos, breaks the resonant chains, and causes systems to spread out and become dynamically excited. A small fraction of resonant chains remain stable after the disk dissipates; these may represent iconic

[4] This idea forms the basis of a model of super-Earth formation sometimes called *inside-out planet formation* (Boley and Ford 2013; Chatterjee et al. 2014, 2015; Hu et al. 2016, 2018). That model invokes the direct formation of super-Earths from pebbles at pressure bumps in the inner disk.

systems such as Trappist-1 (Gillon et al. 2017; Luger et al. 2017) and Kepler-223 (Mills et al. 2016).

Simulations of the migration model have shown that the surviving systems quantitatively match the population of observed super-Earths as long as more than 90% of resonant chains become unstable (Izidoro et al. 2017, 2019). When run through a simulated observing pipeline, the significant dynamical excitation of the surviving systems implies large enough inclinations such that most viewing geometries can only see a single planet in transit. This solves the so-called Kepler dichotomy problem (Johansen et al. 2012; Fang and Margot 2012) and implies that all super-Earth systems are inherently multiple. The period ratio distribution of simulated systems matches observations, again taking observational biases into account (Izidoro et al. 2017, 2019; Mulders et al. 2019).

Yet questions remain. If super-Earth formation is as efficient as in simulations, why don't all stars have them? One possibility is that when an outer gas giant planet forms, it blocks the inward migration of large embryos and those instead become ice giants (Izidoro et al. 2015a, b). This implies an anti-correlation between the presence of outer gas giants and systems with many super-Earths, and it remains unclear if such an anti-correlation exists (Bryan et al. 2019; Zhu and Wu 2018; Barbato et al. 2018). The fraction of stars with gas giants appears to be far less than the fraction of stars without super-Earths, which makes it difficult to imagine gas giants being the main cause. Is it possible, instead, that outer ice giants or super-Earths are the culprit? Probably not. While their occurrence rate is high (Gould et al. 2010; Suzuki et al. 2016b), outer ice giants cannot efficiently block the inward migration of other planets and are generally too low-mass to block the pebble flux (Morbidelli et al. 2012; Lambrechts and Johansen 2014; Bitsch et al. 2018). Perhaps, instead, many disks are subdivided into radial zones (Johansen et al. 2009). Pebbles trapped within a given zone may not be able to drift past the zone boundary such that the pebble flux in certain regions of the disk would remain too low for planets to grow fast enough for long-range migration (Lambrechts et al. 2019a). Such a scenario would also be compatible with the ringed structures seen in many ALMA disks (Andrews et al. 2018).

The compositions of super-Earths may also provide a constraint for formation models. It naively seems that the migration model should produce very volatile-rich super-Earths because the main source of mass is beyond the snow line, where the efficiency of pebble accretion is higher (Morbidelli et al. 2015; Izidoro et al. 2019; Bitsch et al. 2019a, b). This need not be true in 100% of cases, as inward-migrating icy embryos can in some cases stimulate the growth of inner, purely rocky planets (Raymond et al. 2018b). However, most super-Earths in the migration model should be ice-rich (Izidoro et al. 2019). It is unclear whether this is consistent with the observed distribution of bulk densities of super-Earths. While it has been claimed that most super-Earths appear to be "rocky" (Owen and Wu 2013, 2017; Lopez 2017; Jin and Mordasini 2018), measurement uncertainties preclude any clear determination of the compositions of super-Earths (Dorn et al. 2015, 2018). In addition, "rocky" planets may in some context include water contents up to ∼20% by mass (Gupta and Schlichting 2019). For context, that is similar to the approximate water contents

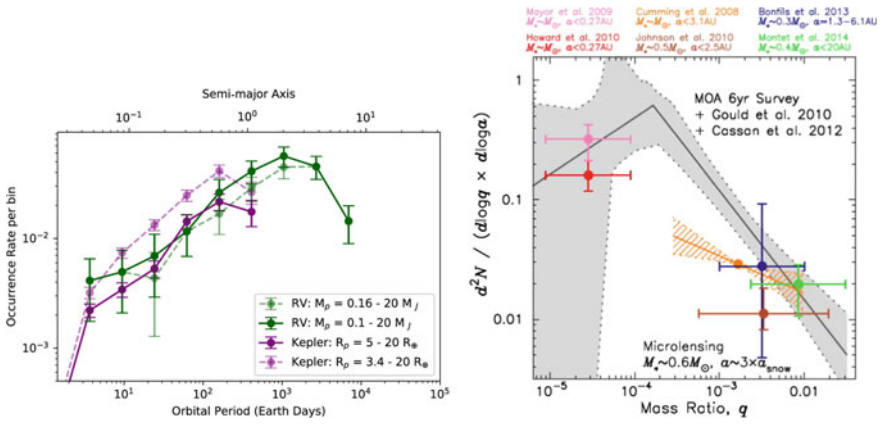

Fig. 1.16 Mass and orbital radius distributions of giant exoplanets. *Left-hand panel:* The frequency of giant planets as a function of orbital distance from radial velocity surveys (green) and the Kepler transit statistics (purple). Figure courtesy of R. B. Fernandes, from Fernandes et al. (2019). *Right-hand panel:* The occurrence rate of giant planets as a function of planet-to-star mass ratio q. The different symbols correspond to different radial velocity studies whereas the black line and grey regions are the results from microlensing surveys. Figure courtesy of T. K. Suzuki, from Suzuki et al. (2016a)

of comet 67P (Pätzold et al. 2019), Pluto, and the most water-rich meteorites known (thought to originate from the outer Solar System; Alexander 2019a; 2019b). Finally, short-lived radionuclides such as Al-26 may efficiently dry out some super-Earths (Lichtenberg et al. 2019). The rocky versus icy nature of super-Earths remains an important outstanding issue.

The fact that super-Earths seem to ubiquitously have large radii consistent with atmospheres of a few percent H/He by mass (Weiss and Marcy 2014; Wolfgang et al. 2016; Fulton et al. 2017; Fulton and Petigura 2018) confirm that these planets formed during the gaseous disk phase and certainly by a process quite different than the formation of our own terrestrial planets. Formation models are starting to be coupled to models of atmospheric accretion and loss (Inamdar and Schlichting 2015; Ginzburg et al. 2016; Carrera et al. 2018). However, given the complexities in these processes (Lambrechts and Lega 2017) this remains an ongoing challenge.

1.3.2 Giant Exoplanets: Formation and Dynamics

Drawing from numerous radial velocity, transit and microlensing surveys for exoplanets, the essential constraints on giant planet formation (further reviewed in Chaps. 3 and 4) are:

- Gas giants exist around roughly 10% of Sun-like stars (Cumming et al. 2008; Mayor et al. 2011; Winn and Fabrycky 2015; Foreman-Mackey et al. 2016; Suzuki

et al. 2016b; Fernandes et al. 2019) and are more/less common around more/less massive stars (Lovis and Mayor 2007; Johnson et al. 2007; Clanton and Gaudi 2014, 2016).
- Most gas giants are on relatively wide orbits past 0.5–1 au (Butler et al. 2006; Udry et al. 2007; Mayor et al. 2011; Rowan et al. 2016; Wittenmyer et al. 2016, 2020).
- Gas giant exoplanets tend to have much higher eccentricities than Jupiter and Saturn, following a broad eccentricity distribution with a median of ∼0.25 (Butler et al. 2006; Udry and Santos 2007; Wright et al. 2009; Bonomo et al. 2017).
- There is a strong correlation between a star's metallicity and the probability that it hosts a gas giant planet (Gonzalez et al. 1997; Santos et al. 2001; Fischer and Valenti 2005), especially among hot Jupiters and gas giants with eccentric orbits (Dawson and Murray-Clay 2013).

There exist two categories of formation models for giant planets (Boley 2009; Helled et al. 2014). The first is a top-down, collapse scenario in which a localized instability in a protoplanetary disk can lead to the direct formation of one or more giant planets. The second is the bottom-up, core accretion scenario (which we argue below should really be called the *core-migration-accretion* scenario). In recent years the core accretion model has become the dominant one, yet it is plausible that some systems may be explained by the disk instability model.

Disk Instability

The disk instability scenario (Boss 1997, 1998, 2000; Mayer et al. 2002, 2007) invokes a localized region of the disk that becomes gravitationally unstable. This is usually quantified with the Toomre Q criterion (Toomre 1964):

$$\frac{c_s\,\Omega}{\pi\,G\,\Sigma} < Q_{\rm crit} \approx 1, \tag{1.44}$$

where c_s is the sound speed, Ω is the local orbital frequency, G is the gravitational constant, and Σ is the local surface density of the disk. Simulations show that in disks that have $Q \lesssim 1$, fragmentation does indeed occur and Jupiter-mass clumps form quickly (Boss 1998; Mayer et al. 2007; Boley et al. 2010). To become true gas giants, these clumps must cool quickly to avoid being sheared apart by the Keplerian flow.

It is generally thought that only the outermost parts of massive disks are able to attain the criteria needed for instability (Meru and Bate 2011; Armitage 2011; Kimura and Tsuribe 2012). The very distant, massive planets such as those of the HR8799 system (Marois et al. 2008, 2010) may perhaps be explained by disk instability, as other mechanism struggle to form such massive planets so far away from their stars. However, it is not clear whether disk instability can produce Jupiter-like planets (although the giant planet orbiting the low-mass star GJ 3512 is a very good candidate; Morales et al. 2019). Planets or clumps that form very far out would also migrate inward rapidly (Baruteau et al. 2011) and it is unclear whether they would survive. In the *tidal downsizing model*, gravitational instability forms clumps in the outer

parts of disks that migrate inward but are often disrupted to act as the seeds of much smaller planets (Nayakshin et al. 2015).

Core-*Migration*-Accretion

The bottom-up, core accretion scenario forms the basis of the current paradigm of giant planet formation. In its standard form the core-accretion model essentially represents a combination of processes summarized in Sect. 1.2.3 (growth of protoplanets) and 2.5 (gas accretion). As we shall see, another important process (orbital migration—described in Sect. 1.2.4) must be included.

Since its inception, the canonical picture has suffered setbacks related to core growth, migration, and gas accretion (see Sect. 1.2.3). Early models that invoked planetesimals as the building blocks of large cores could not explain the rapid growth of the $\sim$10 $M_{\oplus}$ cores needed to trigger rapid gas accretion (Levison and Stewart 2001; Thommes et al. 2003; Rafikov 2004; Chambers 2006a; Levison et al. 2010). Even in the most optimistic scenarios, planetesimal accretion was simply too slow. In recent years it has been shown that pebble accretion is far more efficient and can indeed—given that there is a sufficiently massive and drawn-out supply of pebbles (Johansen and Lambrechts 2017; Bitsch et al. 2019a)—explain the rapid growth of giant planet cores (Ormel and Klahr 2010; Lambrechts and Johansen 2012, 2014). It has also been shown that gas accretion is actually not halted, and only modestly slowed down, by the generation of a gap in the disk (D'Angelo et al. 2003; Uribe et al. 2013).

Migration remains a giant issue for the core accretion model, so much so that the model itself could plausibly be renamed the core-*migration*-accretion model. It is not so much a problem as an added dimension. The mass scale at which gas accretion becomes an important phenomenon is similar to that at which migration becomes important. Thus, planets that are undergoing gas accretion must necessarily be migrating at the same time. Growth tracks of planets must include both radial and mass growth.

Figure 1.17 shows the growth tracks of four different simulated planets. Starting from $\sim$lunar-mass cores, each planet's growth is initially determined simply by the flux of pebbles across its orbit (Lambrechts and Johansen 2014; Ida et al. 2016). Once each planet reaches several Earth masses, it starts to migrate inward. At the same time it starts to slowly accrete gas. Above the pebble isolation mass (defined in Sect. 1.2.3), pebble accretion is stopped but migration and gas accretion continue. The two inner planets in the simulation grew fast enough to undergo rapid gas accretion and become gas giants, whereas the two outer planets did not accrete enough gas before the disk dispersed and thus ended up as ice giants.

Figure 1.17 leads to a naive-sounding but surprisingly profound question: *Why is Jupiter at 5 au?* In the model from Fig. 1.17, any core that started within roughly 10 au ended up as a hot Jupiter. Likewise, in order to finish at 5 au a core needed to start at 15–20 au (see also Bitsch et al. 2015a; Ndugu et al. 2018). How, then did our own Jupiter avoid this fate? There are currently four possible solutions. First, perhaps Jupiter's core simply did form at 15–20 au (Bitsch et al. 2015b). While this is hard to rule out, it seems unlikely because most material that originated interior to Jupiter's orbit would have remained interior to Jupiter's final orbit (Raymond and

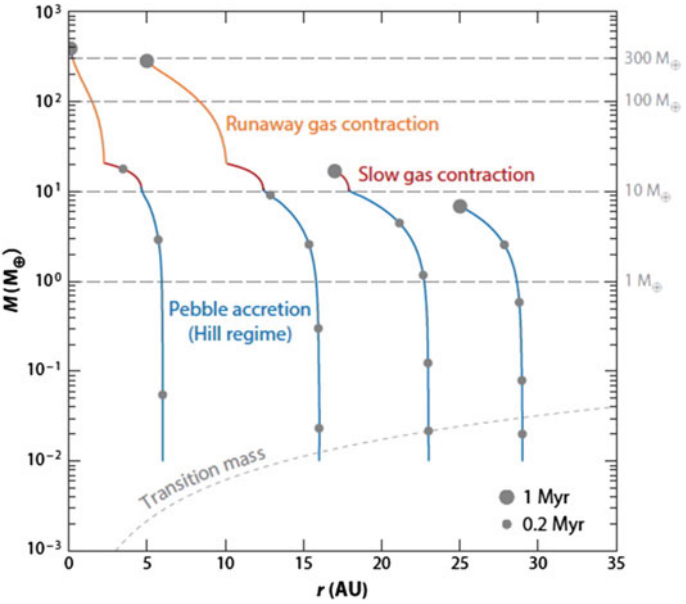

Fig. 1.17 Growth tracks for four different types of planets from simulations that include pebble accretion and migration and gas accretion. The leftmost planet grows fast enough to migrate a long distance and become a hot Jupiter. The second planet from the left starts as a core at ∼15 au and ends up as a Jupiter-like planet at 5 au. The two planets on the right are ice giant analogs that never undergo rapid gas accretion. In this case the pebble isolation mass—the mass above which the pebble flux is blocked and pebble accretion shut off (Lambrechts et al. 2014; Bitsch et al. 2018)—was fixed at 10 $M_\oplus$. Each small dot denotes a time interval of 0.2 Myr along the growth tracks and each large dot a time interval of 1 Myr. Figure courtesy of A. Johansen, from Johansen and Lambrechts (2017)

Izidoro 2017a; Pirani et al. 2019). This would therefore require that only a few Earth masses of material formed in the entire Solar System interior to 15-20 au. Second, perhaps Jupiter's migration was much slower than that shown in Fig. 1.17. That could be the case if the disk's viscosity was much lower than generally assumed, which is consistent with new disk models (see Sect. 1.2.1). Third, perhaps Jupiter's migration was halted because the inner gas disk was evaporated away by energetic radiation from the active young Sun (Alexander and Pascucci 2012). Indeed, disks are thought to disperse by being photo-evaporated by their central stars (Alexander et al. 2014), and this may be a consequence. Fourth, perhaps Jupiter's migration was held back by Saturn. Hydrodynamical simulations show that, while a Jupiter-mass planet on its own migrates inward, the Jupiter-Saturn pair can avoid rapid inward migration and sometimes even migrate outward (Masset and Snellgrove 2001; Morbidelli et al. 2007; Pierens and Nelson 2008; Zhang and Zhou 2010; Pierens and Raymond 2011; Pierens et al. 2014). This forms the basis of the Grand Tack model of Solar System formation, which we will discuss in detail in Sect. 1.3.3.2. However, that model's

potential fatal flaw is that avoiding inward migration requires that Jupiter and Saturn maintain a specific mass ratio of roughly 3-to-1 (Masset and Snellgrove 2001) and it is uncertain whether that ratio can be maintained in the face of gas accretion.

Despite these uncertainties, the core accretion model can match a number of features of the known exoplanet population (Ida et al. 2004; Mordasini et al. 2009; Ndugu et al. 2018), including the observed giant planet-metallicity correlation (Fischer and Valenti 2005) and the much higher abundance of Neptune-mass compared with Jupiter-mass planets (Butler et al. 2006; Udry et al. 2007; Suzuki et al. 2016b).

Unstable Giant Planet Systems and the Exoplanet Eccentricity Distribution

Gas giant exoplanets are often found on non-circular orbits. This is surprising because, as we saw in Sect. 1.2, planets form in disks and so on orbits similar to the disks' streamlines, which are all circular and coplanar. The broad eccentricity of giant planets was for years a subject of broad speculation (for a historical discussion and a comprehensive list of proposed mechanisms, see Ford and Rasio, 2008). The most likely culprit is a mechanism often referred to as *planet-planet scattering* (Rasio and Ford 1996; Weidenschilling and Marzari 1996; Lin and Ida 1997). The planet-planet scattering model proposes that the giant exoplanets formed in systems with many planets and that those that we see are the survivors of dynamical instabilities. Instabilities lead to orbit crossing, followed by a phase of gravitational scattering that usually concludes when one or more planets are ejected from the system entirely, typically leaving the surviving planets with eccentric orbits (Marzari and Weidenschilling 2002; Adams and Laughlin 2003; Montesinos et al. 2005; Chatterjee et al. 2008; Jurić and Tremaine 2008; Nagasawa et al. 2008; Raymond et al. 2008b, 2009a, 2010, 2011, 2012; Beaugé and Nesvorný 2012).

Whereas instabilities among systems of rocky planets tend to lead to collisions, among systems of giant planets they lead to scattering and ejection. This can be understood by simply considering the conditions required for a planet to be able to give a strong enough gravitational kick to eject another object. The Safronov number Θ is simply the ratio of the escape speed from a planet's surface to the escape speed from the star at that orbital radius. It is defined as:

$$\Theta^2 = \left(\frac{G\,m_p}{R_p}\right)\left(\frac{a_p}{G\,M_\star}\right) = \frac{m_p}{M_\star}\frac{a_p}{R_p}, \tag{1.45}$$

where m_p and $M_\star$ are the planet and star mass, respectively, a_p is the planet's orbital radius, and R_p its physical radius. When $\Theta < 1$ collisions are (statistically-speaking) favored over ejection, and when $\Theta > 1$ ejection is favored. Scattering and ejection are therefore favored for massive planets far from their stars. It is interesting to note that Θ is defined in the same way as the gravitational focusing factor F_G from Eq. (1.17) in Sect. 1.2.2, which described the gravitational cross section of a growing protoplanet such that $F_G = 1 + (V_{\rm esc}/V_{\rm rel})^2$. Here, in the context of scattering, the dynamics are the same but in reverse. While the gravitational focusing factor F_G describes from how far away can a planet accrete another object, Θ is a measure of how far a planet can launch another object.

The planet-planet scattering model matches the observed eccentricity distribution of giant exoplanets (Adams and Laughlin 2003; Jurić and Tremaine 2008; Chatterjee et al. 2008; Raymond et al. 2009a, 2010). The only requirement is that a large fraction of systems have undergone instabilities. In simulations performed to date, at least 75%—and probably more likely 90–95%—of giant planets systems must have undergone planet-planet scattering in their past (Jurić and Tremaine 2008; Raymond et al. 2010, 2011). Scattering can even explain the highest-eccentricity giant exoplanets (Carrera et al. 2019).

There is an anti-correlation between giant exoplanet masses and eccentricities. More massive planets are observed to have higher eccentricities (Jones et al. 2006; Ribas and Miralda-Escudé 2007; Wright et al. 2008). This is the opposite of what one would expect from planet-planet scattering. Given that scattering is a process of equipartition of energy, one would naturally expect the low-mass planets to end up with high eccentricities and the high-mass planets with low-eccentricities. This is indeed what is seen in simulations of unstable systems starting with a dispersion of different planet masses. The solution to this conundrum may be quite simply that massive planets form in systems with many, roughly equal-mass planets (Raymond et al. 2010; Ida et al. 2013). In that case, the most massive planets do indeed end up on the most eccentric orbits, as observed.

A *Breaking the Chains* Scenario for Giant Planets

The evolution of giant planet systems may well parallel that of super-Earths. As we saw in Sect. 1.3.1, the prevailing model for super-Earth formation—called *breaking the chains* (Izidoro et al. 2017)—involves migration into resonant chains followed by instability. Could this same evolutionary pathway apply to giant planet systems (Fig. 1.18)?

The answer appears to be yes. Giant planets may indeed follow a *breaking the chains*-style evolution that is similar, but not identical, to that of super-Earth systems.

Survival of resonances after the gaseous disk phase may be somewhat more common for giant planet systems. Only a few dozen giant planets are known to be found in resonance (e.g., the GJ876 resonant chain of giant planets; Rivera et al. 2010). Yet it is possible that many more resonant pairs of giant planets are hiding in plain site. The radial velocity signatures of resonant planets can mimic those of a single eccentric planet (Anglada-Escudé et al. 2010) and it is possible that up to 25% of the current sample of eccentric planets are actually pairs of resonant planets (Boisvert et al. 2018). The PDS 70 protoplanetary disk may host a pair of young giant planets in resonance (Bae et al. 2019), and other disk signatures may require multi-resonant planets to explain them (Dodson-Robinson and Salyk 2011). When multiple giant planets form within a given disk it may thus slow and limit migration. This contrasts with the case of super-Earths, which migrate all the way to the disk's inner edge.

Instabilities appear to be ubiquitous among both super-Earths and giant exoplanets. As discussed above, the eccentricities of giant exoplanets are easily matched if most systems are survivors of instability. Instabilities may be triggered by the dispersal of the gaseous disk (Matsumura et al. 2010), chaotic diffusion within the giant

planets' orbits (Marzari and Weidenschilling 2002; Batygin and Morbidelli 2015), or external perturbations, e.g. from wide binary stars (Kaib et al. 2013).

Connection with Rocky Planets and Debris Disks

When giant planets go unstable they affect their entire system. Given their large masses and the high eccentricities they reach during the scattering phase, giant planets can wreak havoc on their inner and outer systems. Giant planet scattering systematically disrupts inner rocky planet systems (Veras and Armitage 2005, 2006; Matsumura et al. 2013; Carrera et al. 2016) or their building blocks (Raymond et al. 2011, 2012), usually by driving inner bodies onto such eccentric orbits that they collide with their host stars (see Fig. 1.19). Scattering also tends to destroy outer planetesimals disks by ejecting planetesimals into interstellar space (Raymond et al. 2011, 2012, 2013; Marzari 2014). Outer planetesimal belts—when they survive and contain enough mass to self-excite to a moderate degree—evolve collisionally to produce cold dust observed as debris disks (Wyatt 2008; Krivov 2010; Matthews et al. 2014; Hughes et al. 2018).

Raymond et al. (2011, 2012) proposed that, by influencing both the inner and outer parts of their systems, giant planets induce a correlation between rocky inner planets and debris disks. Hints of a correlation have been found (Wyatt 2012) but more data are needed. It has also been suggested that giant planets—especially those on very eccentric orbits—should anti-correlate with the presence of debris disks. While there may be a tendency for debris disks to be less dense in systems with eccentric giant planets (Bryden et al. 2009), no strong correlation or anti-correlation between giant planets and debris disks has been observed to date (Moro-Martín et al. 2007, 2015).

Nonetheless, connections between planetary system architecture and the presence and characteristics of dust remains an active area of study.

1.3.3 Solar System Formation

The standard timeline of Solar System formation proceeds as follows. Time zero is generally taken as the formation of Calcium- and Aluminum-rich Inclusions, or CAIs. CAIs are the oldest known inclusions in chondritic meteorites aged to be 4.568 Gyr old (Amelin et al. 2002; Bouvier and Wadhwa 2010; Connelly et al. 2012). Radioactive ages of iron meteorites suggest that their parent bodies—several hundred to a thousand-km scale planetary embryos—were fully formed within 1 Myr after CAIs (Halliday and Kleine 2006; Kruijer et al. 2014; Schiller et al. 2015). There are two isotopically distinct types of meteorites: the so-called carbonaceous and non-carbonaceous groups (Warren 2011). There is a broad distribution in the ages of both types of meteorites, whose overlap indicate that these very different types of meteorites accreted simultaneously (Amelin et al. 2002; Warren 2011; Kruijer et al. 2017). Chondrules—the primitive, mm-scale building blocks of chondritic meteorites—are found at the size scale at which objects drift rapidly through the disk due to aerodynamic drag (Weidenschilling 1977b; Lambrechts and Johansen

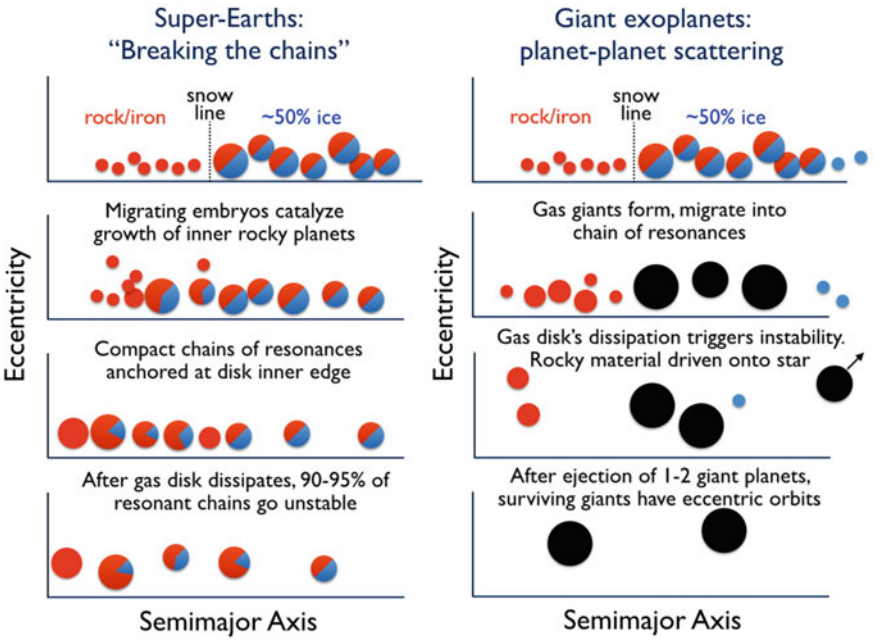

Fig. 1.18 Cartoon comparison of the evolution of super-Earth and giant planets systems. The same general processes could very well causing both populations to follow *breaking the chains*-like pathways (Raymond et al. 2018d)

2012; Johansen et al. 2015). The separation of the two different types of chondritic meteorites is interpreted as indicating that two isotopically-distinct reservoirs were kept spatially segregated, perhaps by the rapid growth of a large planetary embryo to the pebble isolation mass (Budde et al. 2016; Kruijer et al. 2017). This may thus constrain the timing of the growth of Jupiter's core to have been very rapid, reaching the critical mass to block the pebble flux (of $\sim$10$-$20 $M_{\oplus}$; Bitsch et al., 2018) within 1–1.5 Myr after CAIs (Kruijer et al. 2017).

The gaseous disk probably lasted for roughly 5 Myr. Gaseous disks around other stars are observed to dissipate on a few Myr timescale (see Fig. 1.2). The oldest chondritic meteorites are the CB chondrites, which formed roughly 5 Myr after CAIs albeit perhaps in the absence of gas (Kita et al. 2005; Krot et al. 2005; Johnson et al. 2015). Given that gas is thought to be needed for planetesimal formation (Johansen et al. 2014), this implies 5 Myr as an upper limit on the gas disk lifetime (at least in some regions).

Hafnium-Tungsten measurements of Martian meteorites indicate that Mars' formation was basically finished within 5–10 Myr (Nimmo and Kleine 2007; Dauphas and Pourmand 2011), meaning that it grew very little after the disk had dispersed. In contrast, Hf/W measurements indicate that Earth's last differentiation event—generally thought to have been the Moon-forming impact—did not take place until $\sim$100 Myr after CAIs (Touboul et al. 2007; Kleine et al. 2009). However, uncertain-

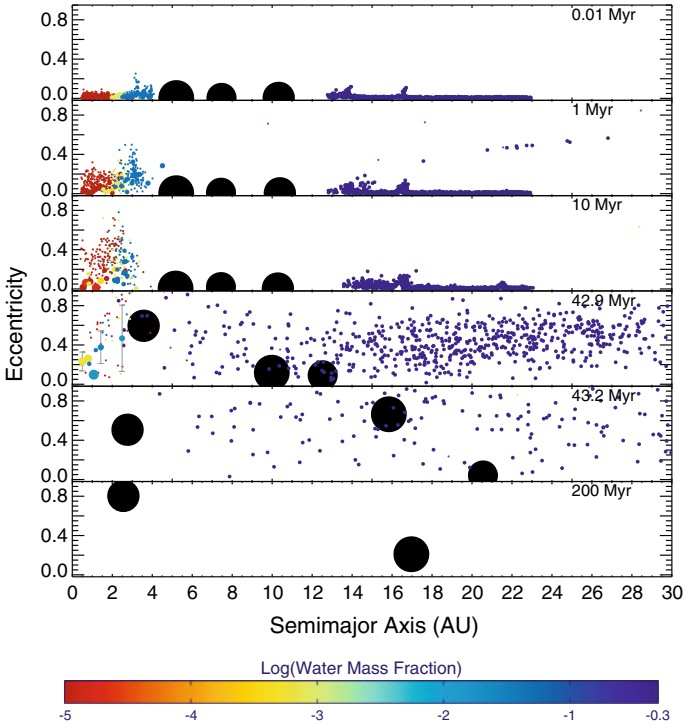

Fig. 1.19 Evolution of a simulation in which a system of gas giant went unstable, resulting in the destruction of both an inner system of growing terrestrial planets (that were driven into collisions with the central star) and an outer disk of ice-rich planetesimals (that was ejected into interstellar space; see Raymond et al. (2018a, c). From Raymond et al. (2012)

ties in the degree of equilibration of the Hf/W isotopic system during giant impacts make it hard to determine a more accurate timeframe (Fischer and Nimmo 2018).

Highly-siderophile ("iron-loving") elements should in principle be sequestered in the core during differentiation events. Thus, any highly-siderophile elements in the terrestrial mantle and crust should in principle have been delivered *after* the Moon-forming impact (Kimura et al. 1974). Simulations show that there is a clear anti-correlation between the timing of the last giant impact on Earth and the mass in planetesimals delivered after the last giant impact (Jacobson et al. 2014). The total amount of highly-siderophile elements can therefore constrain the timing of the impact. Assuming a chondritic composition, Earth accreted the last ~0.5% of its mass as a veneer after the Moon-forming impact (Morbidelli and Wood 2015). This implies that the Moon-forming impact took place roughly 100 Myr after CAIs (Jacobson et al. 2014), consistent with the Hf/W chronometer.

The Solar System's giant planets are thought to have undergone an instability. The so-called *Nice model* showed that the giant planets' current orbital configuration (Tsiganis et al. 2005; Nesvorný and Morbidelli 2012)—as well as the orbital

properties of Jupiter's Trojans (Morbidelli et al. 2005; Nesvorný et al. 2013), the irregular satellites (Nesvorný et al. 2014), and the Kuiper belt (Levison et al. 2008; Nesvorný 2015)—could be explained by a dynamical instability in the giant planets' orbits (Nesvorný 2018b). The instability is generally thought to have been triggered by interactions between the giant planets and a remnant planetesimal disk, essentially the primordial Kuiper belt (Gomes et al. 2005; Morbidelli et al. 2007; Levison et al. 2011; Quarles and Kaib 2019), although a self-driven instability is also possible (Raymond et al. 2010; de Sousa et al. 2020). The instability was first proposed to explain the so-called terminal lunar cataclysm, i.e. an abrupt increase in the flux of projectiles hitting the Moon roughly 500 Myr after CAIs (Tera et al. 1974; Gomes et al. 2005; Morbidelli et al. 2012). However, newer analyses suggest that no terminal lunar cataclysm ever took place (Chapman et al. 2007; Boehnke and Harrison 2016; Zellner 2017; Morbidelli et al. 2018; Hartmann 2019), and that the instability may have taken place anytime in the first ∼100 Myr after CAIs (Morbidelli et al. 2018; Nesvorný et al. 2018; Mojzsis et al. 2019).

Over the past decade, global models of Solar System formation have been revolutionized (see Fig. 1.20). Decades-old models that assumed local growth of the planets (i.e., the so-called *classical model*; Weidenschilli 1977a; Wetherill 1978, 1992; Chambers and Wetherill 1998; Chambers 2001; Raymond et al. 2004, 2009b; 2014; O'Brien et al. 2006) have been supplanted with models that explain the distribution of the planets and small body belts by invoking processes such as long-range migration of the giant planets (the *Grand Tack* model; Walsh et al. 2011; Raymond and Morbidelli 2014; Brasser et al. 2016), non-uniform planetesimal formation within the disk (the *Low-mass Asteroid belt* model; Hansen 2009; Izidoro et al. 2015c; Drążkowska et al. 2016; Raymond and Izidoro 2017b) and an early instability among the giant planets' orbits (the *Early Instability* model; Clement et al., 2018, 2019a, b). Pebble accretion has been proposed to play an important role during the terrestrial planets' growth (Levison et al. 2015), the importance of which may be constrained by isotopic measurements of different types of meteorites as well as Earth samples (Warren 2011; Kruijer et al. 2017; Schiller et al. 2018; Budde et al. 2019).

Here we first describe the classical model and then the other competing models. We then compare the predictions of different models.

1.3.3.1 The Classical Model

The classical model of terrestrial planet formation makes two dramatically simplifying assumptions. First, it assumes that the planets formed roughly in place. This implies that one can reconstruct the approximate mass distribution of the protoplanetary disk by simply spreading the planets' masses out in concentric annuli (the so-called 'minimum-mass solar nebula' model; Weidenschilling 1977a; Hayashi 1981; Davis 2005). Second, it assumes that giant- and terrestrial planet formation can be treated separately. Thus, one can study the influence of the giant planets' orbits on terrestrial planet formation after the gas disk had dispersed without the need to consider their earlier effects.

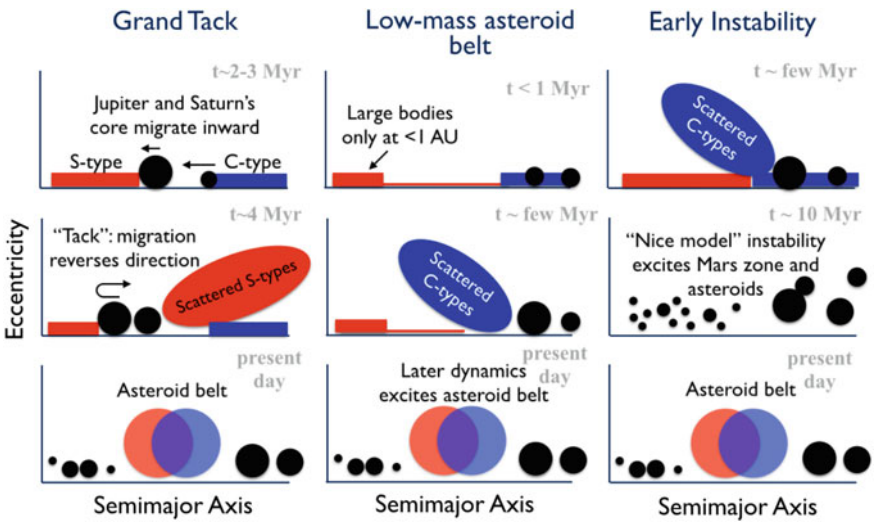

Fig. 1.20 Cartoon comparison between three plausible models for Solar System formation described in Sects. 3.3.2, 3.3.3, and 3.3.4. From Raymond et al. (2018d)

Figure 1.21 shows a simulation of the classical model of terrestrial planet formation (from Raymond et al. 2006a). In this case Jupiter is included on a supposed pre-instability orbital configuration, on a near-circular orbit. The terrestrial disk is initially composed of roughly 2000 planetary embryos with masses between that of Ceres and the Moon. Accretion is driven from the inside-out by gravitational self-stirring and from the outside-in by secular and resonant forcing from Jupiter. There is a long chaotic phase of growth that involves many giant impacts between planetary embryos (see e.g. Agnor et al. 1999; Kokubo and Ida 2007; Quintana et al. 2016). The planets grow on a timescale of 10−100 Myr. Remnant planetesimals are cleared out on a longer timeframe. There is sufficient radial mixing during growth for water-rich material from past 2.5 au to have been delivered to the growing Earth (see extensive discussion of the origin of Earth's water in Sect. 1.3.4).

The classical model has a fatal flaw: it systematically produces Mars analogs that are far more massive than the real Mars (Wetherill 1991). This can be seen in the simulation from Fig. 1.21, which formed passable Venus and Earth analog, but a Mars analog roughly as massive as Earth. The true problem is not Mars' absolute mass but the large Earth/Mars mass ratio. The classical model tends to produce systems in which neighboring planets have comparable masses rather than the ∼9:1 Earth/Mars ratio (Raymond et al. 2006a; O'Brien et al. 2006; Raymond et al. 2009b; Morishima et al. 2008, 2010; Fischer and Ciesla 2014; Kaib and Cowan 2015). Classical model simulations tend to have two other problems related to the asteroid belt: large embryos are often stranded in the belt (Raymond et al. 2009b), and they do not match the belt's eccentricity and inclination distributions (Izidoro et al. 2015c).

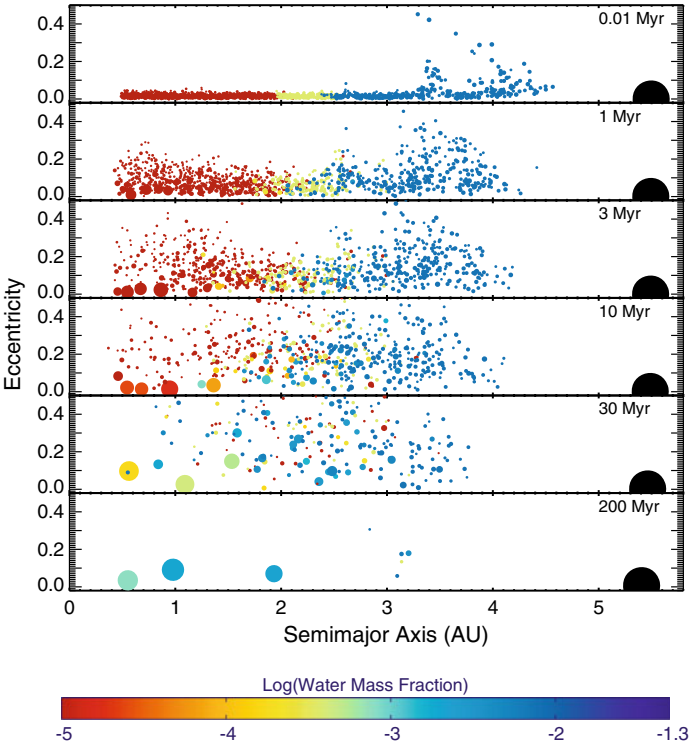

Fig. 1.21 Simulation of the classical model of terrestrial planet formation (Raymond et al. 2006a). The size of each planetary embryo scales with its mass m as $m^{1/3}$. Colors represent the water contents, initially calibrated to match the water contents of current orbital radii of different populations of primitive asteroids (Gradie and Tedesco 1982; Raymond et al. 2004). Jupiter is the large black circle

The building blocks of the terrestrial planets were roughly Mars-mass and thus the inner Solar System may only have contained roughly two dozen embryos (Morbidelli et al. 2012). One may wonder how often a small Mars arises because, by chance, it avoided any late giant impacts. Fischer and Ciesla (2014) showed that this happens in a few percent of simulations. However, when one takes the asteroid belt constraints into consideration the success rate of the classical model in matching the inner Solar System drops by orders of magnitude (Izidoro et al. 2015c).

The 'small Mars' problem—first pointed out by Wetherill (1991) and re-emphasized by Raymond et al. (2009b)—is thus the Achilles heel of the classical model. It prompted the development of alternate models, whose goal was to explain how two neighboring planets could have such different masses.

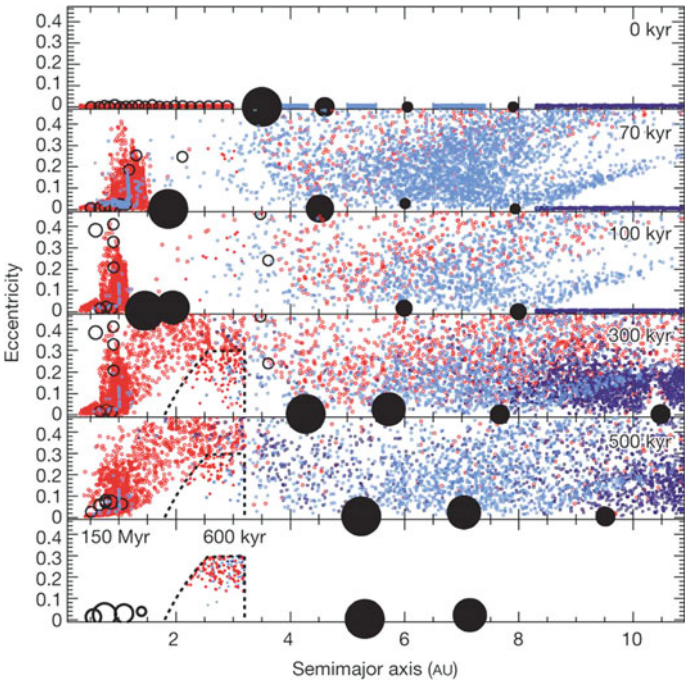

Fig. 1.22 Evolution of the Grand Tack model (Walsh et al. 2011). The giant planets' migration (black symbols) sculpts the distribution of rocky bodies in the inner Solar System. Here Jupiter migrated inward, then Saturn migrated inward, and then the two planets migrated back out. The red dots indicate presumably dry, S-type planetesimals that formed interior to Jupiter's orbit, whereas the blue dots represent planetesimals originally between and beyond the giant planets' orbits. Rocky planetary embryos are shown as empty circles. The bottom three panels include dashed contours of the present-day main asteroid belt

1.3.3.2 The Grand Tack Model

The Grand Tack model (Walsh et al. 2011) proposed that Jupiter's migration during the gaseous disk phase was responsible for depleting Mars' feeding zone. The Grand Tack is based on hydrodynamical simulations of orbital migration (see Sect. 2.4 and 2.5 for more details). Simulations show the giant planets carve annular gaps in the disk (Lin and Papaloizou 1986; Ward 1997; Crida et al. 2006). A single planet usually migrates inward on a timescale that is related to the disk's viscous timescale (D'Angelo et al. 2003; Dürmann and Kley 2015). Multiple planets often migrate convergently and become trapped in mean-motion resonances (Snellgrove et al. 2001; Lee and Peale 2002), often sharing a common gap. When the inner planet is two to four times more massive than the outer one and both planets are in the gap-opening regime, gas piles up in the inner disk and a toque imbalance causes the two planets to migrate *outward* (Masset and Snellgrove 2001; Morbidelli et al.

2007; Pierens and Nelson 2008; Zhang and Zhou 2010; Pierens and Raymond 2011; Pierens et al. 2014).

The Grand Tack model proposes that Jupiter formed first and migrated inward. Saturn formed more slowly, migrated inward and caught up to Jupiter. The two planets became locked in resonance and migrated outward together until either the disk dissipated or certain conditions slowed their migration (e.g., if the disk was flared such that Saturn dropped below the gap-opening limit in the outer disk).

The evolution of the Grand Tack model is shown in Fig. 1.22. If Jupiter's inward migration reached 1.5−2 au then the inner disk would have been truncated at ∼1 au, depleting Mars' feeding zone but not Earth's (Walsh et al. 2011; Brasser et al. 2016). The terrestrial planets in simulations provide a good match to the real ones (Walsh et al. 2011; Jacobson and Morbidelli 2014; Brasser et al. 2016).

The asteroid belt is severely depleted by Jupiter's migration but is not completely emptied (Walsh et al. 2011, 2012). The S-types were scattered outward by Jupiter's inward migration, then back inward by Jupiter's outward migration, with an efficiency of implantation of ∼0.1%. The C-types were scattered inward by Jupiter and Saturn's outward migration. The final belt provides a reasonable match to the real one—particularly when evolved over Gyr timescales (Deienno et al. 2016). It is worth noting, however, that the initial conditions in Fig. 1.22 neglect additional (possibly much more important) phases of implantation that took place during Jupiter and Saturn's rapid gas accretion (Raymond and Izidoro 2017a).

The Grand Tack's potential Achilles heel is the mechanism of outward migration itself (see discussion in Raymond and Morbidelli 2014). The most stringent constraint on outward migration is that it requires a relatively limited range of mass ratios between Jupiter and Saturn (roughly between a ratio of 2:1 and 4:1; Masset and Snellgrove 2001). It remains to be seen whether long-range outward migration remains viable when gas accretion is consistently taken into account, as the gas giants' mass ratio should be continuously changing during this phase. There may also be geochemical constraints related to the speed of accretion in the Grand Tack model (Zube et al. 2019).

1.3.3.3 The Low-Mass Asteroid Belt Model

The Low-Mass Asteroid belt model makes the assumption that Mars' small mass is a consequence of a primordial mass deficit between Earth and Jupiter's present-day orbits. Gas disks are generally expected to have smooth radial distributions, but this is not the case for dust. Dust drifts within disks and ALMA images show that dust rings are common in protoplanetary disks (ALMA Partnership 2015; Andrews et al. 2018). Given that planetesimal formation via the streaming instability is sensitive to the local conditions (Simon et al. 2016; Yang et al. 2017), dust rings may be expected to produce rings of planetesimals. One model of dust drift and coagulation, combined with the conditions needed to trigger the streaming instability, showed that planetesimals may indeed form rings (Drążkowska et al. 2016).

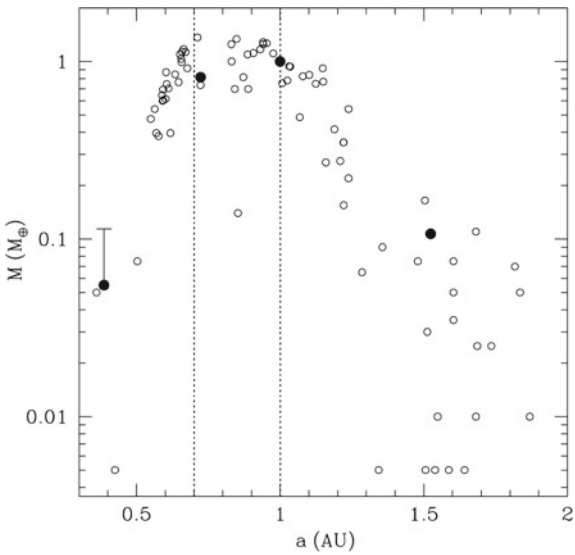

Fig. 1.23 Distribution of simulated terrestrial planets formed assuming that all of the terrestrial planets' mass was initially found in a narrow annulus between the orbits of Venus and Earth (denoted by the dashed vertical lines). The open circles show simulated planets and the solid ones are the real planets. From Hansen (2009)

Since the 1990s it was known that if an edge existed in the initial distribution of planetary embryos or planetesimals, any planet that formed beyond that edge would be much less massive than the planets that formed within the main disk (Wetherill 1992, 1996; Chambers and Wetherill 1998; Agnor et al. 1999; Chambers 2001). However, it was Hansen (2009) who proposed that such an edge might really have existed in the early Solar System. Indeed, he showed that the terrestrial planets can be matched if they formed from a narrow annulus of rocky material between the orbits of Venus and Earth (see Fig. 1.23). In this model the large Earth/Mars mass ratio is a simple consequence of the depletion of material past Earth's orbit, and the small Mercury/Venus mass ratio is a consequence of the analogous depletion interior to Venus' orbit.

The most extreme incarnation of the Low-mass asteroid belt model proposes that no planetesimals formed between the orbits of Earth and Jupiter (Hansen 2009; Raymond and Izidoro 2017b), but the model is also consistent with planetesimal forming in the belt, just at a reduced efficiency. Yet, even an empty primordial asteroid belt would have been dynamically re-filled with objects originating across the Solar System. Rapid gas accretion onto Jupiter and later Saturn destabilizes the orbits of nearby planetesimals, many of which are gravitationally scattered in all directions. Under the action of gas drag, a fraction of planetesimals are trapped on stable, low-eccentricity orbits, preferentially in the asteroid belt (Raymond and Izidoro 2017a), and some are scattered past the asteroid belt to the terrestrial planet region itself (see Fig. 1.27 and Sect. 1.3.4). On a longer timescale, the growing terrestrial planets scatter remnant planetesimals outward, a small fraction of which are trapped in the main belt, preferentially in the inner parts (Raymond and Izidoro 2017b).

The main uncertainty in the Low-mass asteroid belt are the initial conditions. When disk models, dust growth and drift, disk observations and interpretation (including studies of ALMA-detected disks), and meteorite constraints (including the broad age distribution of non-carbonaceous chondrites, which indicate many different planetesimal formation events; Kruijer et al. 2017) are all accounted for, will it be a reasonable assumption that the terrestrial planets could have formed from a narrow ring of planetesimals?

1.3.3.4 The Early Instability Model

It has been demonstrated numerically that dynamical instabilities among giant planets cause severe damage to the small bodies in their same systems (see Fig. 1.19). The Solar System's giant planets are thought to have undergone an instability, albeit a much less violent one than the typical instability incurred by giant exoplanet systems. Nonetheless, the Solar System's instability is violent enough that, if they were fully-formed at the time, the terrestrial planets would have had a very low probability of survival (Kaib and Chambers 2016). Yet the timing of the instability is uncertain, and it could have happened anytime in the first 100 million years of Solar System evolution (Morbidelli et al. 2018; Mojzsis et al. 2019). One may then wonder whether a very early instability could have played a role in shaping the distribution of the terrestrial planets.

The Early Instability model, conceived and developed by Clement et al. (2018, 2019a, b), is built on the premise that the giant planets' instability took place within roughly 10 Myr of the dissipation of the gaseous disk. The evolution of one realization of the model is shown in Fig. 1.24. The early evolution of the Early Instability model is identical to that in the classical model. The giant planets' dynamical instability—triggered after 10 Myr in the simulation from Fig. 1.24—strongly excites the orbits of inner Solar System objects extending through the asteroid belt in to Mars' feeding zone (Deienno et al. 2018; Clement et al. 2019b). The belt is strongly depleted and dynamically excited, and Mars' growth is effectively stunted. In a fraction of simulations no Mars forms at all (Clement et al. 2018)! The growth of Earth and Venus are largely unperturbed and qualitatively similar to the classical model.

The instability itself is stochastic in nature. Matching the instability statistically requires a large number of numerical realizations, which produce a spectrum of Solar Systems with different properties. Such simulations have more constraints than many because they include all of the planets and not just the terrestrial planets. One remarkable feature of the Early Instability model is that systems that provide the best match to the outer Solar System are the same ones that provide the best match to the terrestrial planets (Clement et al. 2018, 2019a, b).

The main uncertainty in the Early Instability model is simply the timing of the instability. Mars' formation was largely complete within 5–10 Myr (Nimmo and Kleine 2007; Dauphas and Pourmand 2011), shortly after the disappearance of the gaseous disk. To affect terrestrial planet formation, the giant planets must therefore have gone unstable within perhaps 5 Myr of the disk's dispersal. This would also

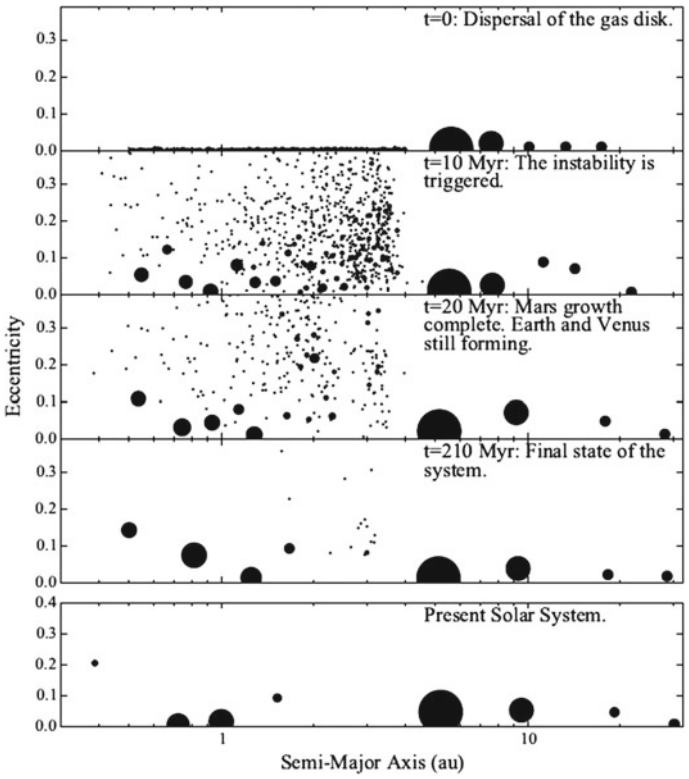

Fig. 1.24 Evolution of the Early Instability model. In this case the giant planets' instability was triggered 10 Myr after the dissipation of the disk. The instability strongly excited the orbits of growing planetesimals and planetary embryos in the asteroid belt and Mars' feeding zone. Mars' growth was stunted, but Earth and Venus continued to accrete for ∼100 Myr. The final system has a large Earth/Mars mass ratio and an overall planetary system architecture similar to the actual Solar System (shown at bottom for comparison). Figure courtesy of M. S. Clement, from Clement et al. (2018)

imply a cometary bombardment in the inner Solar System that was coincident with the late phases of terrestrial planet growth. While such a bombardment would deliver only a very small amount of mass to Earth (Morbidelli et al. 2000; Gomes et al. 2005), it would provide a large component of Earth's noble gases (Marty et al. 2016). The Xe isotopic compositions of the mantle and atmosphere are different (Mukhopadhyay 2012; Caracausi et al. 2016), and it has been suggested that a comet-delivered component contributed to the atmospheric Xe budget but not to the mantle Xe (Marty et al. 2017). It remains to be understood whether or not this implies that the bulk of Earth accreted with little cometary influx, which would constrain the timing of cometary delivery and presumably of the instability itself.

1.3.3.5 Other Models

It is worth noting that the three scenarios outlined above as alternatives to the classical model are not the only ones that have been proposed. For example, it was suggested that sweeping secular resonances during the dissipation of the gaseous disk could have depleted and excited the asteroid belt and generated an edge in the terrestrial planets' mass distribution (Nagasawa et al. 2005; Thommes et al. 2008; Bromley and Kenyon 2017). The main uncertainty in that model is whether a non-zero eccentricity of Jupiter can realistically be maintained during the gas dissipation phase.

It has also been suggested that pebble accretion may have played a role in terrestrial planet formation (Levison et al. 2015; Chambers et al. 2016). Isotopic analyses of meteorites may help to constrain the degree to which carbonaceous pebbles from the outer Solar System contributed to the growth of the terrestrial planets (Schiller et al. 2018; Budde et al. 2019). In general, the formation of Earth-mass planets within the disk lifetime poses a problem because, given that the gas disk is required for pebble accretion, such planets should grow fast enough to migrate inward and become super-Earths (Lambrechts et al. 2019a).

1.3.4 Origin of Water on Earth and Rocky Exoplanets

We now turn our attention to the origin of planets' water. Cosmochemical tracers such as isotopic ratios can be used to constrain the potential sources of Earth's water (see, e.g., Morbidelli et al. 2000; Marty 2012). While bulk density measurements of solid exoplanets can in principle be used to trace water contents (Valencia et al. 2007; Sotin et al. 2007; Fortney et al. 2007; Seager et al. 2007), in practice it is extremely challenging (Adams et al. 2008; Selsis et al. 2007; Dorn et al. 2015). There have been a few recent reviews on the origins of Earth's water in dynamical and cosmochemical context (O'Brien et al. 2018; McCubbin and Barnes 2019; Meech and Raymond 2019).

Earth is our benchmark for water. While it appears blue from space, all of Earth's oceans only add up to $\sim 2.5 \times 10^{-4}\, M_\oplus$ of water. This is generally referred to as one "ocean" of water. The water budget of Earth's interior is quite uncertain. Different studies infer different quantities of water trapped in hydrated silicates, with overall budgets between roughly one and ten oceans (Hirschmann 2006; Mottl et al. 2007; Marty 2012; Halliday 2013). Earth's core may be very dry (Badro et al. 2014) or may contain fifty or more oceans of water (Nomura et al. 2014). While papers often quote Earth as being roughly one part in a thousand water by mass, it is important to be aware of the uncertainty.

Figure 1.25 shows the D/H ratios for a number of Solar System objects (for a compilation of references to the D/H measurements, see Morbidelli et al. 2000; Marty and Yokochi 2006; Alexander et al. 2012, 2018). The Sun and gas-dominated planets have D/H ratios roughly six times lower than Earth's. This is interpreted as the isotopic composition of the gaseous protoplanetary disk. Carbonaceous chondrite

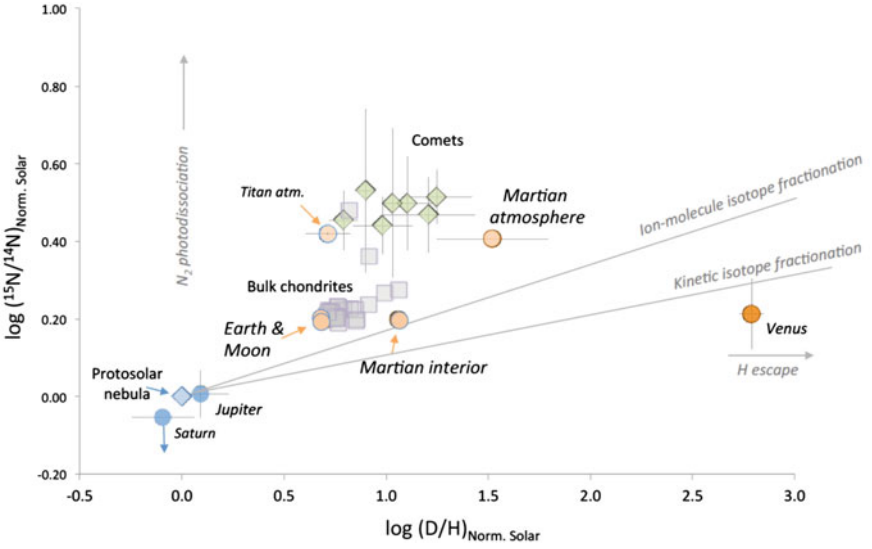

Fig. 1.25 Measured $^{15/14}$N isotope ratios vs. D/H ratios of Solar System objects. Arrows indicate how different processes would affect an object's evolution in this isotope space. Figure courtesy of B. Marty, from Marty et al. (2016)

meteorites have similar D/H values to Earth. Most measured comets have higher D/H values than Earth, although two recently-measured Jupiter-family comets (Hartogh et al. 2011; Lis et al. 2013) and one Oort cloud comet (Biver et al. 2016) have Earth-like D/H ratios. In contrast, ESA's Rosetta mission measured the D/H ratio of comet 67P/C-G to be more than three times the terrestrial value. A recent result (Sosa and Fernández 2011; Lis et al. 2019) found that very active comets tended to have Earth-like D/H whereas less active ones have higher D/H. One interpretation is that comets' original water was Earth-like and loss processes during outgassing have fractionated the surviving D/H. If true, that would mean render the D/H ratio useless as a discriminant between comets and carbonaceous sources of water. One must then resort to dynamical constraints or perhaps to other isotopic systems.

Figure 1.25 naively would suggest carbonaceous chondrite-like objects as the source of Earth's water and Nitrogen. Yet, even if Earth's water were delivered by carbonaceous objects, that is only a part of the story. A complete model must explain the full evolution of our planetary system and, in the context of Earth's water, ask: where did the water-bearing objects themselves originate?

We can break down the various models for water delivery into six rough scenarios that we outline below. Two of these models invoke local sources of water whereas the others propose that Earth's water was delivered from farther out in the disk. For a comprehensive review of these models, see Meech and Raymond (2019).

Adsorption of Water Vapor Onto Silicate Grains

In a simple picture of the structure of disks, water should exist as a solid past the snow line and as a vapor closer-in. If water vapor was indeed present where silicate grains were coalescing to form the terrestrial planets, then "in-gassing" may have attached hydrogen molecules to silicate grains (Stimpfl et al. 2006; Muralidharan et al. 2008; Asaduzzaman et al. 2014; Sharp 2017; D'Angelo et al. 2019). This process is called adsorption. The mechanism can in principle have seeded Earth with a few oceans of water, albeit without taking any water loss processes into account, such as ^{26}Al-driven heating (Grimm and McSween 1993; Monteux et al. 2018) or impact-related losses (Genda and Abe 2005; Svetsov 2007). Yet at face value it should have seeded Earth with nebular water, which has a D/H ratio six times smaller than Earth's. It also cannot explain the abundance of other volatiles such as C, N and the noble gases, which would then require an alternate source containing little hydrogen. Finally, it begs the question of why the Enstatite chondrites—meteorites that provide the closest chemical match to Earth's bulk composition (Dauphas 2017)—appear to have formed without any water.

Oxidation of H-Rich Primordial Envelope

As planetary embryos grow, they gravitationally accrete H-rich envelopes if they are more massive than a few tenths of Earth's mass (Ikoma et al. 2000; Lambrechts and Lega 2017). This hydrogen could have chemically reacted with Earth's surface magma ocean and generated water by hydrating silicates (Ikoma and Genda 2006). Given that the D/H ratio of nebular gas was many times smaller than Earth's water, this model, like the previous one, predicts that Earth's initial D/H ratio was small. In this case, however, it is possible to envision that Earth's D/H changed in time. The loss of a thick hydrogen envelope would certainly entail mass fractionation, and for a certain range of parameters Earth's final D/H ratio can be matched even though its water was acquired from gas (Genda and Ikoma 2008). However, the collateral effects of this presumed atmospheric loss have not been quantified, and appear to be at odds with other constraints, such as the abundance of ^{129}Xe from the decay of ^{129}I (Marty et al. 2016). In addition, it seems quite a coincidence for Earth to match carbonaceous chondrites in multiple isotopic systems as a result of such loss processes, which would affect different molecules differently.

Pebble "Snow"

Planets beyond the snow line accrete water as a solid. It is simply a building block. Yet the snow line is a moving target. As the disk evolves and cools, the snow line generally moves inward (Sasselov and Lecar 2000; Lecar et al. 2006; Martin and Livio 2012). A planet on a static orbit would see the snow line sweep past it. Such a planet would start off in the rocky part of the disk but, once the snow line passed interior to its orbit, would find itself outside the snow line, in the presumably icy part of the disk (see Fig. 1.26).

As the snow line sweeps inward, new ice does not come from the condensation of water vapor. This is because the speed at which gas moves through the disk is far

faster than the motion of the snow line itself (Morbidelli et al. 2016). Thus, the gas just interior to the snow line is dry. Rather, ice at the snow line comes from pebbles and dust that drift inward through the disk. The source of these drifting pebbles is thought to move outward as an analogous wave of dust coagulation and growth sweeps radially out through the disk (Birnstiel et al. 2012; Lambrechts et al. 2014; Birnstiel et al. 2016; Ida et al. 2016). If anything blocks the inward flow of pebbles—such as a growing giant planet core (Lambrechts and Johansen 2014; Bitsch et al. 2018)—the snow line will continue to move inward but it will not bring any ice along with it (Morbidelli et al. 2016). The source of water will also drop if the outward-sweeping growth front producing pebbles reaches the outer edge of the disk (Ida et al. 2019).

In the Solar System there is evidence that the pebble-sized building blocks carbonaceous and noncarbonaceous were segregated as of 1–1.5 Myr after CAIs (Budde et al. 2016; Kruijer et al. 2017). This would suggest that carbonaceous pebbles did not deliver Earth's water, as their widespread presence in the inner Solar System would presumably have produced a category of meteorites intermediate in isotopic composition between the carbonaceous and noncarbonaceous. The Enstatite chondrites, which formed near the end of the disk's lifetime and are the closest chemical match to Earth, are dry (Alexander et al. 2018).

Nonetheless, pebble snow may be a key mechanism in delivering water to rocky exoplanets (see below).

Wide Feeding Zone

A planet's feeding zone is simply the radial distribution of its constituents. In the classical model, the terrestrial planets formed from a broad disk of planetary embryos extending from Venus' orbit out to Jupiter's. For example, in the simulation from Fig. 1.21, each of the three surviving terrestrial planets accreted material from a broad swath of the disk. Given that the constituent planetesimals should have a radial gradient in composition based on the local temperature (Dodson-Robinson et al. 2009), this implies that volatiles are naturally incorporated into growing planets if the planets' feeding zones extend out far enough (Morbidelli et al. 2000; Raymond et al. 2004, 2007a).

The planets' broad feeding zones—in concert with the isotopic match between Earth's water and that of carbonaceous chondrites—led to the scenario that Earth's water was delivered by primordial carbonaceous planetesimals or planetary embryos (Morbidelli et al. 2000; Raymond et al. 2004, 2007a). However, this idea was built on the classical model. As the classical model crumbled under the weight of the small Mars problem (see Sect. 1.3.3) the idea that Earth's water was a result of its broad feeding zone no longer made sense. The Early Instability model (Clement et al. 2018, 2019a, b) starts from essentially the same initial conditions as the classical model and presents a viable solution to the small Mars problem all the while delivering water to Earth by the same mechanism. However, like the classical model (Raymond et al. 2009b), the Early Instability may only adequately deliver water to Earth in simulations that fail to match Mars' small mass (Clement and Rubie, personal communication). The Early Instability model acknowledges that in order

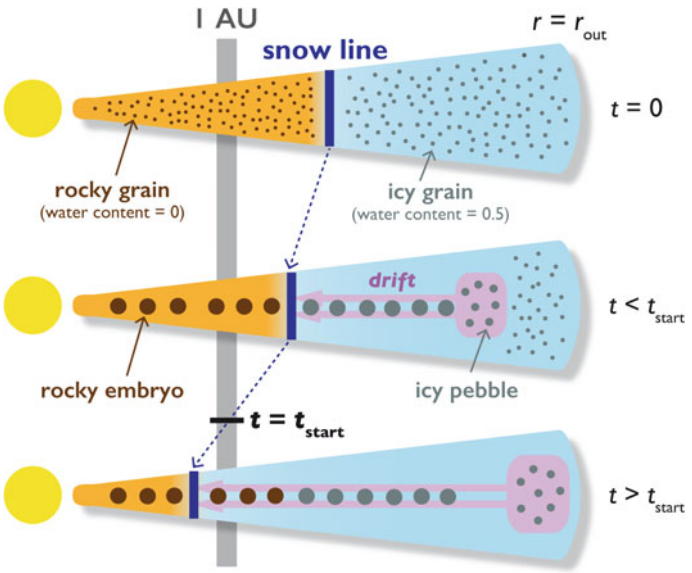

Fig. 1.26 The *pebble snow* model (Oka et al. 2011; Sato et al. 2016; Ida et al. 2019). Rocky planetary embryos grow from rocky grains interior to the snow line. As the disk cools, the snow line sweeps inward and ice-rich pebbles from the outer parts of the disk deliver water to the terrestrial planet region. Figure courtesy of T. Sato, from Sato et al. (2016)

to understand in the first place the existence of water-rich asteroids intermixed with water-poor asteroids in the asteroid belt, which may have been the result of the growth and/or migration of the giant planets. That leads us to the next scenario.

External Pollution

The orbits of leftover planetesimals are strongly perturbed by the growth and migration of the giant planets. The phase of rapid gas accretion is particularly dramatic. The mass of the giant planets can increase from $\sim 10-20\ M_\oplus$ up to hundreds of Earth masses on a $\sim 10^5$ year timescale (Pollack et al. 1996; Ida et al. 2004). This rapid gas accretion destabilizes the orbits of any nearby planetesimals that managed to avoid being accreted. Many planetesimals undergo close gravitational encounters with the growing planet and are scattered in all directions. Under the action of gas drag, many planetesimals are trapped interior to the giant planet's orbit (Raymond and Izidoro 2017a; Ronnet et al. 2018). This happens when a planetesimal on an eccentric orbit that crosses the giant planet's orbit at apocenter undergoes sufficient orbital energy loss due to gas drag to drop its apocenter away from the giant planet, releasing it from the gas giant's dynamical clutches.

Figure 1.27 shows this process in action. Jupiter's growth triggers a pulse of planetesimal scattering, and a second is triggered when Saturn forms. The outcomes of these pulses can vary because the disk itself changes in time as it both slowly dissipates and, more importantly, is sculpted by the giant planets.

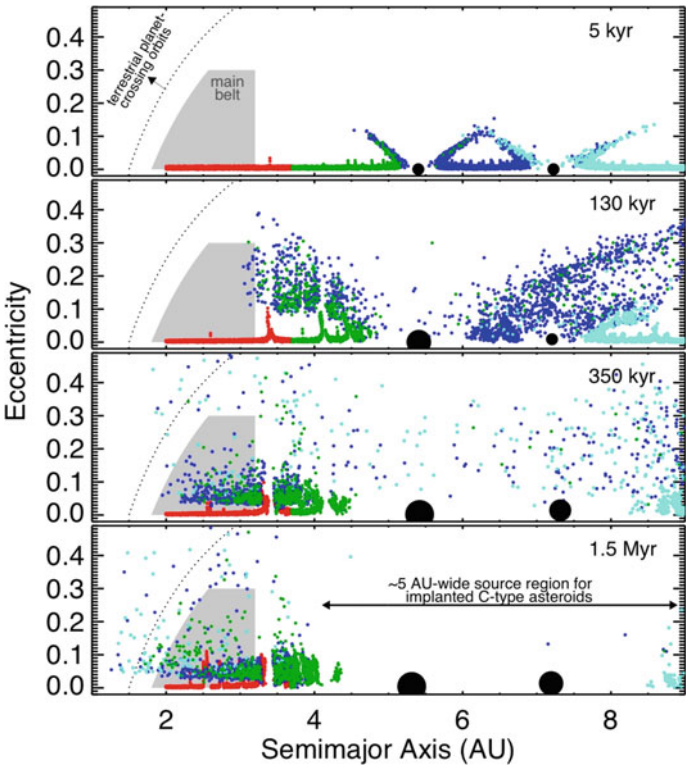

Fig. 1.27 Scattering of ten thousand planetesimals driven by the growth of Jupiter (from 100 – 200 kyr) and Saturn (from 300 – 400 kyr). Planetesimals from the Jupiter-Saturn region end up polluting the inner Solar System *en masse*. Some are trapped in the outer parts of the main asteroid belt (shaded) and some are scattered past the belt to the terrestrial planet region (above the dashed line). And even so, this example shows the minimum expected impact of the giant planets' growth, as it assumed the giant planets to have formed on low-eccentricity, non-migrating orbits in 3:2 resonance. Planetesimal colors correspond simply to each object's starting location. There is an underlying gaseous disk in the simulation, whose structure and overall density evolve in time in a consistent way. In this example, planetesimals were assumed to be 100 km in diameter for the gas drag calculation. From Raymond and Izidoro (2017a)

The relative number of planetesimals that are trapped in the main asteroid belt (providing an orbital match to the C-types) vs. those that are scattered *past* the asteroid belt to the terrestrial planets (to deliver water) varies as a function of the strength of gas drag (Raymond and Izidoro 2017a). When gas drag is strong—i.e., for a massive inner gas disk or smaller planetesimals—scattered planetesimals are rapidly decoupled from Jupiter and are generally trapped in the outer parts of the main belt. When gas drag is weak—for a low-density inner disk or large planetesimals—it takes a large number of orbits for gas drag to decouple planetesimals' orbits from Jupiter. Planetesimals are more frequently scattered farther inward to pollute the terrestrial planet-forming region and to deliver water.

A similar mechanism is driven by giant planet migration. In the Grand Tack model, Jupiter and Saturn's outward migration scatters a large number of planetesimals inward (Walsh et al. 2011, 2012; see Fig. 1.22). Given that the giant planets are migrating away, scattered planetesimals are more easily decoupled from the giant planets. The distribution of scattered planetesimals that survive on orbits interior to the giant planets' have a much weaker size dependence than for those that were scattered during the giant planets' growth and for which gas drag played a central role. The dependence on the gas surface density is also much weaker.

Both migration and growth can thus generate populations of terrestrial planet-crossing planetesimals that originated beyond Jupiter. Given their distant origins these planetesimals tend to have high-eccentricity orbits, but simulations show that they are nonetheless accreted by the terrestrial planets on a geochemically consistent timescale and in sufficient quantity to easily deliver Earth's water budget (O'Brien et al. 2014). In addition, they naturally match the compositions of carbonaceous meteorites.

In the wide feeding zone model, the C-type asteroids represented the distant, mother source of Earth's water. In the pollution model, Earth's water was delivered from the same parent population as the objects that were implanted into the asteroid belt as C-types. Thus, Earth's water and C-type asteroids are brother and sister.

At present, the pollution scenario is the leading model to explain the origin of Earth's water. It matches the amount and chemical signature of Earth's water, and naturally fits within different models of Solar System formation.

Inward Migration

Earth-mass planets migrate relatively rapidly in protplanetary disks (see Sects. 1.2.2 and 1.3.1). Given that large embryos are thought to form fastest past the snow line (Lambrechts and Johansen 2014; Morbidelli et al. 2015), this implies that many inward-migrating planets or cores should be water-rich (Bitsch et al. 2019b). Indeed, the migration model for super-Earth formation predicts that most should be water-rich (Raymond et al. 2018b; Izidoro et al. 2019). Inward-migrating gas giants can shepherd material interior to their orbits and trigger the formation of very water-rich terrestrial planets (Raymond et al. 2006b; Mandell et al. 2007).

A number of lines of evidence point to the terrestrial planets having formed from ∼Mars-mass planetary embryos (Morbidelli et al. 2012). This is below the mass threshold for large-scale migration (Ward 1997), and so we do not think that Earth accreted any water from inward-migrating embryos.

However, migration may prove a central water delivery mechanism in other systems (see below).

Extrapolation to Exoplanets

Let us now very simply extrapolate these six water delivery (or water production) mechanisms to exoplanet systems. Most of these mechanisms can account for Earth's water budget with perhaps an order of magnitude variation.

We propose that the water contents of rocky planets are likely to have a bimodal distribution. Migration is the key player. If embryos grew large enough and underwent

long-range migration then they must invariably pollute the terrestrial planet-forming region (Izidoro et al. 2014). This should lead to elevated water contents of ∼10% by mass. However, if migration was not involved, then the other mechanisms discussed can still deliver an Earth-like or higher water budget. Gas giants are rare enough around Sun-like and low-mass stars that they probably do not play the central role in water delivery in general terms (although they likely dominate in their own systems). Pebble snow can in principle deliver tens to hundreds of oceans, but requires a clear path between the outward-sweeping icy pebble front and the rocky planet zone that is unencumbered by pressure bumps, including those produced by growing planets (which are themselves growing by consuming icy pebbles).

If migration is indeed the key, then one might predict an observational marker between the action of migration and the planets' water and other volatile contents. Such an observational test is beyond current capabilities but may be imaginable in the coming decade or two.

1.4 The Future of Planet Formation Studies

We conclude this broad-sweeping review with our vision for the future of planet formation. We cannot pretend to have a coherent view of all of the theoretical and empirical challenges that will push the field forward. Nonetheless, we proceed by highlighting three action items: a key bottleneck for planet formation models, one particularly promising path forward, and a call for connection.

A Key Bottleneck for Planet Formation

We consider the central bottleneck in planet formation to be understanding the underlying structure of protoplanetary disks (see Sect. 2.1 and discussion in Morbidelli and Raymond, 2016). Disks are the birthplace of planets. Their underlying structure controls how dust grows and drifts, where dust or pebbles pile up to become sufficiently concentrated to form planetesimals, as well as how fast and in what direction planets migrate. Simple viscous disk models do not match observations and have been supplanted by models that include effects such as ambipolar diffusion and wind-driven angular momentum loss. ALMA observations of disks (Andrews et al. 2018) provide ever more stringent constraints on such models, yet to date there is no underlying model that matches the population of disk observations. Of course, interactions with other stars during the embedded cluster phase leads to a diversity of disk properties, but with statistically described distributions (Bate 2018). We encourage future work to develop comprehensive, trustworthy disk models.

Coupling Dynamical and Chemical Models

One key path forward for understanding the early evolution of the Solar System is coupling dynamical and accretion models with cosmochemical constraints. Some constraints are already being used by current models. For example, the D/H ratio—especially when combined with the $^{15/14}$N ratio (Marty and Yokochi 2006; Marty

et al. 2016)—appears to be a powerful tracer of Earth's water. Isotope systems such as Hf/W already provide strong constraints on the timing of planetary accretion. Some formation models also incorporate simple chemical models (Rubie et al. 2015). Yet, there remain many connections to be made between dynamical models and cosmochemistry.

A Call to Connect Different Constraints and Models

We conclude this chapter with a call to create as many connections as possible. This is a large variety of disciplines linked together to create the field of planet formation. These include observations of protoplanetary disks and debris disks, exoplanet studies, meteorite analysis, planetary surfaces (e.g., crater modeling), orbital dynamics, gasdynamics, small body studies, and a variety of different types of numerical modeling. We encourage the reader to strive to make connections between their specialty and others. Many of the most interesting dynamical models come from connections between subdisciplines. For example, the idea of the Solar System's instability (the *Nice model* Tsiganis et al., 2005; Gomes et al., 2005; Nesvorný, 2018b) was born from a dynamical model to explain the now-defunct terminal lunar cataclysm. The *Grand Tack* model of Solar System formation (Walsh et al. 2011) was inspired by numerical studies of planet migration designed to explain the origin of hot Jupiters (Lin et al. 1996). Giant exoplanets orbiting stars with wide companions have more eccentric orbits than giant exoplanets around single stars; this is a result of Oort cloud comet-like oscillations in the orbits of wide binary stars (Kaib et al. 2013).

Connecting the dots in new ways is essential to moving the field of planet formation forward.

Acknowledgements We are grateful to the Agence Nationale pour la Recherche, who sponsored our research from 2014-2018 (project *MOJO*).

References

Abod, C.P., Simon, J.B., Li, R., et al.: Astrophys. J. **883**, 192 (2019)
Absil, O., Defrère, D., Coudé du Foresto, V., et al.: Astron. Astrophys. **555**, A104 (2019)
Adams, E.R., Seager, S., Elkins-Tanton, L.: Astrophys. J. **673**, 1160 (2008)
Adams, F.C., Hollenbach, D., Laughlin, G., Gorti, U.: Astrophys. J. **611**, 360 (2004)
Adams, F.C., Laughlin, G.: Icarus **163**, 290 (2003)
Agnor, C.B., Canup, R.M., Levison, H.F.: Icarus **142**, 219 (1999)
Alexander, C.M.O.: Geochemica Cosmochemica Acta **254**, 246 (2019a)
Alexander, C.M.O.: Geochemica Cosmochemica Acta **254**, 277 (2019b)
Alexander, C.M.O., Bowden, R., Fogel, M.L., et al.: Science **337**, 721 (2012)
Alexander, C.M.O., McKeegan, K.D., Altwegg, K.: Space Sci. Rev. **214**, 36 (2018)
Alexander, R., Pascucci, I., Andrews, S., Armitage, P., Cieza, L.: Protostars Planets VI, p. 475 (2014)
Alexander, R.D., Armitage, P.J.: Astrophysi. J. Lett. **639**, L83 (2006)
Alexander, R.D., Pascucci, I.: Monthly Not. Roy. Astronom. Soc. **422**, L82 (2012)
ALMA Partnership, Brogan, C.L., Pérez, L.M., Hunter, T.R., et al.: Astrophys. J. Lett. **808**, L3 (2015)

Amelin, Y., Krot, A.N., Hutcheon, I.D., Ulyanov, A.A.: Science **297**, 1678 (2002)
Andrews, S.M., Huang, J., Pérez, L.M., et al.: Astrophys. J. Lett. **869**, L41 (2018)
Andrews, S.M., Williams, J.P.: Astrophys. J. **631**, 1134 (2005)
Andrews, S.M., Williams, J.P.: Astrophys. J. **671**, 1800 (2007a)
Andrews, S.M., Williams, J.P.: Astrophys. J. **659**, 705 (2007b)
Andrews, S.M., Wilner, D.J., Hughes, A.M., et al.: Astrophys. J. **700**, 1502 (2009)
Andrews, S.M., Wilner, D.J., Hughes, A.M., et al.: Astrophys. J. **723**, 1241 (2010)
Andrews, S.M., Wilner, D.J., Zhu, Z., et al.: Astrophys. J. Lett. **820**, L40 (2016)
Anglada-Escudé, G., López-Morales, M., Chambers, J.E.: Astrophys. J. **709**, 168 (2010)
Anglada-Escudé, G., Tuomi, M., Gerlach, E., et al.: Astron. Astrophys. **556**, A126 (2013)
Armitage, P.J.: Annu. Rev. Astron. Astrophys. **49**, 195 (2011)
Armitage, P.J., Eisner, J.A., Simon, J.B.: Astrophys. J. Lett. **828**, L2 (2016)
Asaduzzaman, A.M., Zega, T.J., Laref, S., et al.: Earth Planet. Sci. Lett. **408**, 355 (2014)
Badro, J., Cote, A., Brodholt, J.: PNAS **132**, 94 (2014)
Bae, J., Zhu, Z., Baruteau, C., et al.: Astrophys. J. Lett. **884**, L41 (2019)
Bai, X.N.: Astrophys. J. **821**, 80 (2016)
Bai, X.N.: Astrophys. J. **845**, 75 (2017)
Bai, X.N., Stone, J.M.: Astrophys. J. **769**, 76 (2013)
Baillié, K., Charnoz, S., Pantin, E.: Astron. Astrophys. **577**, A65 (2015)
Balbus, S.A., Hawley, J.F.: Revi. Mod. Phys. **70**, 1 (1998)
Barbato, D., Sozzetti, A., Desidera, S., et al.: Astron. Astrophys. **615**, A175 (2018)
Barenfeld, S.A., Carpenter, J.M., Sargent, A.I., et al.: Astrophys. J. **851**, 85 (2017)
Baruteau, C., Meru, F., Paardekooper, S.J.: Monthly Not. Roy. Astron. Soc. **416**, 1971 (2011)
Batalha, N.M., Rowe, J.F., Bryson, S.T., et al.: Astrophys. J. Supple. Ser. **204**, 24 (2013)
Bate, M.R.: Monthly Not. Roy. Astron. Soc. **475**, 5618 (2018)
Batygin, K., Morbidelli, A.: Astron. Astrophys. **556**, A28 (2013)
Batygin, K., Morbidelli, A., Holman, M.J.: Astrophys. J. **799**, 120 (2015)
Beaugé, C., Nesvorný, D.: Astrophys. J. **751**, 119 (2012)
Bell, K.R., Lin, D.N.C.: Astrophys. J. **427**, 987 (1994)
Benítez-Llambay, P., Masset, F., Koenigsberger, G., Szulágyi, J.: Nature **520**, 63 (2015)
Benítez-Llambay, P., Pessah, M.E.: Astrophys. J. Lett. **855**, L28 (2018)
Béthune, W., Lesur, G., Ferreira, J.: Astron. Astrophys. **600**, A75 (2017)
Birnstiel, T., Fang, M., Johansen, A.: Space Sci. Rev. **205**, 41 (2016)
Birnstiel, T., Klahr, H., Ercolano, B.: Astron. Astrophys. **539**, A148 (2012)
Bitsch, B., Crida, A., Morbidelli, A., et al.: Astron. Astrophys. **549**, A124 (2013)
Bitsch, B., Morbidelli, A., Lega, E., Crida, A.: Astron. Astrophys. **564**, A135 (2014)
Bitsch, B., Johansen, A., Lambrechts, M., Morbidelli, A.: Astron. Astrophys. **575**, A28 (2015a)
Bitsch, B., Lambrechts, M., Johansen, A.: Astron. Astrophys. **582**, A112 (2015b)
Bitsch, B., Morbidelli, A., Johansen, A., et al.: Astron. Astrophys. **612**, A30 (2018)
Bitsch, B., Izidoro, A., Johansen, A., et al.: Astron. Astrophys. **623**, A88 (2019a)
Bitsch, B., Raymond, S.N., Izidoro, A.: Astron. Astrophys. **624**, A109 (2019b)
Biver, N., Moreno, R., Bockelée-Morvan, D., et al.: Astron. Astrophys. **589**, A78 (2016)
Blum, J., Wurm, G.: Annu. Rev. Astron. Astrophys. **46**, 21 (2008)
Boehnke, P., Harrison, T.M.: Proc. Natl. Acad. Sci. **113**, 10802 (2016)
Boisvert, J.H., Nelson, B.E., Steffen, J.H.: Monthly Not. Roy. Astron. Soc. **480**, 2846 (2018)
Boley, A.C.: Astrophys. J. Lett. **695**, L53 (2009)
Boley, A.C., Ford, E.B.: arXiv:1306.0566 (2013)
Boley, A.C., Hayfield, T., Mayer, L., Durisen, R.H.: Icarus **207**, 509 (2010)
Bonomo, A.S., Desidera, S., Benatti, S., et al.: Astron. Astrophys. **602**, A107 (2010)
Boss, A.P.: Science **276**, 1836 (1997)
Boss, A.P.: Astrophys. J. **503**, 923 (1998)
Boss, A.P.: Astrophys. J. Lett. **536**, L101 (2000)
Bouvier, A., Wadhwa, M.: Nat. Geosci. **3**, 637 (2010)

Bowler, B.P., Nielsen, E.L.: Occurrence rates from direct imaging surveys. In: Deeg, H., Belmonte, J. (eds.) Handbook of Exoplanets. Springer, Cham (2018)
Brasser, R., Matsumura, S., Ida, S., et al.: Astrophys. J. **821**, 75 (2016)
Briceño, C., Vivas, A.K., Calvet, N., et al.: Science **291**, 93 (2001)
Bromley, B.C., Kenyon, S.J.: Astron. J. **153**, 216 (2017)
Bryan, M.L., Knutson, H.A., Lee, E.J., et al.: Astron. J. **157**, 52 (2019)
Bryden, G., Beichman, C.A., Carpenter, J.M., et al.: Astrophys. J. **705**, 1226 (2009)
Bryden, G., Beichman, C.A., Trilling, D.E., et al.: Astrophys. J. **636**, 1098 (2006)
Budde, G., Burkhardt, C., Brennecka, G.A., et al.: Earth Planet. Sci. Lett. **454**, 293 (2016)
Budde, G., Burkhardt, C., Kleine, T.: Nat. Astron. **3**, 736 (2019)
Butler, R.P., Wright, J.T., Marcy, G.W., et al.: Astrophys. J. **646**, 505 (2006)
Campante, T.L., Barclay, T., Swift, J.J., et al.: Astrophys. J. **799**, 170 (2015)
Caracausi, A., Avice, G., Burnard, P.G., et al.: Nature **533**, 82 (2016)
Carpenter, J.M., Bouwman, J., Mamajek, E.E., et al.: Astrophys. J. Suppl. Ser. **181**, 197 (2009)
Carrera, D., Johansen, A., Davies, M.B.: Astron. Astrophys. **579**, A43 (2015)
Carrera, D., Davies, M.B., Johansen, A.: Monthly Not. Roy. Astron. Soc. **463**, 3226 (2016)
Carrera, D., Gorti, U., Johansen, A., Davies, M.B.: Astrophys. J. **839**, 16 (2017)
Carrera, D., Ford, E.B., Izidoro, A., et al.: Astrophys. J. **866**, 104 (2018)
Carrera, D., Raymond, S.N., Davies, M.B.: Astron. Astrophys. **629**, L7 (2019)
Cassan, A., Kubas, D., Beaulieu, J.P.: Nature, **481**, 167 (2012)
Chambers, J.E.: Icarus **152**, 205 (2001)
Chambers, J.E.: Icarus **180**, 496 (2006a)
Chambers, J.E.: Astrophys. J. **879**, 98 (2006b)
Chambers, J.E., Wetherill, G.W.: Icarus **136**, 304 (1998)
Chambers, K.C., Magnier, E.A., Metcalfe, N.: arxiv:1612.05560
Chandrasekhar, S.: Astrophys. J. **97**, 255 (1943)
Chang, S.H., Gu, P.G., Bodenheimer, P.H.: Astrophys. J. **708**, 1692 (2010)
Chapman, C.R., Cohen, B.A., Grinspoon, D.H.: Icarus **189**, 233 (2007)
Chatterjee, S., Ford, E.B., Matsumura, S., Rasio, F.A.: Astrophys. J. **686**, 580 (2008)
Chatterjee, S., Tan, J.C.: Astrophys. J. **780**, 53 (2014)
Chatterjee, S., Tan, J.C.: Astrophys. J. Lett. **798**, L32 (2015)
Chen, J., Kipping, D.: Astrophys. J. **834**, 17 (2017)
Chiang, E., Laughlin, G.: Monthly Not. Roy. Astron. Soc. **431**, 3444 (2013)
Chiang, E., Youdin, A.N.: Annu. Rev. Earth Planet. Sci. **38**, 493 (2010)
Chiang, E.I., Goldreich, P.: Astrophys. J. **490**, 368 (1997)
Clanton, C., Gaudi, B.S.: Astrophys. J. **791**, 91 (2014)
Clanton, C., Gaudi, B.S.: Astrophys. J. **819**, 125 (2016)
Clement, M.S., Kaib, N.A., Raymond, S.N., Walsh, K.J.: Icarus **311**, 340 (2018)
Clement, M.S., Kaib, N.A., Raymond, S.N., et al.: Icarus **321**, 778 (2019a)
Clement, M.S., Raymond, S.N., Kaib, N.A.: Astron. J. **157**, 38 (2019b)
Coleman, G.A.L., Papaloizou, J.C.B., Nelson, R.P.: Monthly Not. Roy. Astron. Soc. **470**, 3206 (2017)
Connelly, J.N., Amelin, Y., Krot, A.N., Bizzarro, M.: Astrophys. J. Lett. **675**, L121 (2008)
Connelly, J.N., Bizzarro, M., Krot, A.N., et al.: Science **338**, 651 (2012)
Cossou, C., Raymond, S.N., Pierens, A.: Astron. Astrophys. **553**, L2 (2013)
Cossou, C., Raymond, S.N., Hersant, F., Pierens, A.: Astron. Astrophys. **569**, A56 (2014)
Cresswell, P., Dirksen, G., Kley, W., Nelson, R.P.: Astron. Astrophys. **473**, 329 (2007)
Crida, A., Morbidelli, A., Masset, F.: Icarus **181**, 587 (2006)
Cumming, A., Butler, R.P., Marcy, G.W.: Proc. Astron. Soc. Pac. **120**, 531 (2008)
D'Angelo, G., Kley, W., Henning, T.: Astrophys. J. **586**, 540 (2003)
D'Angelo, M., Cazaux, S., Kamp, I., et al.: Astron. Astrophys. **622**, A208 (2019)
Dauphas, N.: Nature **541**, 521 (2017)
Dauphas, N., Pourmand, A.: Nature **473**, 489 (2011)

Davis, S.S.: Astrophys. J. Lett. **627**, L153 (2005)
Dawson, R.I., Murray-Clay, R.A.: Astrophys. J. Lett. **767**, L24 (2013)
Dawson, R.I., Chiang, E., Lee, E.J.: Monthly Not. Roy. Astronom. Soc. **453**, 1471 (2015)
Dawson, R.I., Lee, E.J., Chiang, E.: Astrophys. J. **822**, 54 (2016)
de Sousa, R., Morbidelli, A., Raymond, S., et al.: arXiv:1912.10879 (2020)
Deck, K.M., Batygin, K.: Astrophys. J. **810**, 119 (2015)
Deienno, R., Gomes, R.S., Walsh, K.J., et al.: Icarus **272**, 114 (2016)
Deienno, R., Izidoro, A., Morbidelli, A., et al.: Astrophys. J. **864**, 50 (2018)
DeMeo, F.E., Carry, B.: Icarus **226**, 723 (2013)
DeMeo, F.E., Carry, B.: Nature **505**, 629 (2014)
Demory, B.O., Gillon, M., Deming, D., et al.: Astron. Astrophys. **533**, A114 (2011)
Desch, S.J., Turner, N.J.: Astrophys. J. **811**, 156 (2015)
Dodson-Robinson, S.E., Salyk, C.: Astrophys. J. **738**, 131 (2011)
Dodson-Robinson, S.E., Willacy, K., Bodenheimer, P., et al.: Icarus **200**, 672 (2009)
Dong, S., Zhu, Z.: Astrophys. J. **778**, 53 (2013)
Dorn, C., Khan, A., Heng, K., et al.: Astron. Astrophys. **577**, A83 (2015)
Dorn, C., Mosegaard, K., Grimm, S.L., Alibert, Y.: Astrophys. J. **865**, 20 (2018)
Drążkowska, J., Alibert, Y., Moore, B.: Astron. Astrophys., **594**, A105 (2016)
Drążkowska, J., Alibert, Y.: Astron. Astrophys., **608**, A92 (2017)
Drążkowska, J., Dullemond, C.P.: Astron. Astrophys. **614**, A62 (2018)
Duffell, P.C., Haiman, Z., MacFadyen, A.I., et al.: Astrophys. J. Lett. **792**, L10 (2014)
Dullemond, C.P., Birnstiel, T., Huang, J., et al.: Astrophys. J. Lett. **869**, L46 (2018)
Dürmann, C., Kley, W.: Astron. Astrophys. **574**, A52 (2015)
Eisner, J.A., Carpenter, J.M.: Astrophys. J. **598**, 1341 (2003)
Eklund, H., Masset, F.S.: Monthly Not. Roy. Astron. Soc. **469**, 206 (2017)
Ertel, S., Absil, O., Defrère, D., et al.: Astron. Astrophys. **570**, A128 (2014)
Fabrycky, D.C., Lissauer, J.J., Ragozzine, D., et al.: Astrophys. J. **790**, 146 (2014)
Fang, J., Margot, J.L.: Astrophys. J. **761**, 92 (2012)
Fernandes, R.B., Mulders, G.D., Pascucci, I., et al.: Astrophys. J. **874**, 81 (2019)
Fischer, D.A., Valenti, J.: Astrophys. J. **622**, 1102 (2005)
Fischer, D.A., Marcy, G.W., Butler, R.P., et al.: Astrophys. J. **675**, 790 (2008)
Fischer, R.A., Ciesla, F.J.: Earth Planet. Sci. Lett. **392**, 28 (2014)
Fischer, R.A., Nimmo, F.: Earth Planet. Sci. Lett. **499**, 257 (2018)
Flock, M., Fromang, S., Turner, N.J., Benisty, M.: Astrophys. J. **835**, 230 (2017)
Flock, M., Turner, N.J., Mulders, G.D., et al.: Astron. Astrophys. **630**, A147 (2019)
Fogg, M.J., Nelson, R.P.: Astron. Astrophys. **441**, 791 (2005)
Fogg, M.J., Nelson, R.P.: Astron. Astrophys. **461**, 1195 (2007)
Ford, E.B., Lystad, V., Rasio, F.A.: Nature **434**, 873 (2005)
Ford, E.B., Rasio, F.A.: Astrophys. J. **686**, 621 (2008)
Foreman-Mackey, D., Morton, T.D., Hogg, D.W., et al.: Astron. J. **152**, 206 (2016)
Fortney, J.J., Marley, M.S., Barnes, J.W.: Astrophys. J. **659**, 1661 (2007)
Fressin, F., Torres, G., Charbonneau, D., et al.: Astrophys. J. **766**, 81 (2013)
Fulton, B.J., Petigura, E.A.: Astron. J. **156**, 6 (2018)
Fulton, B.J., Petigura, E.A., Howard, A.W., et al.: Astron. J. **154**, 109 (2017)
Genda, H., Abe, Y.: Nature **433**, 842 (2005)
Genda, H., Ikoma, M.: Icarus **194**, 42 (2008)
Gillon, M., Triaud, A.H.M.J., Demory, B.O., et al.: Nature **542**, 456 (2017)
Ginzburg, S., Schlichting, H.E., Sari, R.: Astrophys. J. **825**, 29 (2016)
Goldreich, P., Schlichting, H.E.: Astron. J. **147**, 32 (2014)
Goldreich, P., Tremaine, S.: Astrophys. J. **233**, 857 (1979)
Goldreich, P., Tremaine, S.: Astrophys. J. **241**, 425 (1980)
Gomes, R.S., Morbidelli, A., Levison, H.F.: Icarus **170**, 492 (2004)
Gomes, R., Levison, H.F., Tsiganis, K., Morbidelli, A.: Nature **435**, 466 (2005)

Gonzalez, G.: Monthly Not. Roy. Astron. Soc. **285**, 403 (1997)
Gould, A., Dong, S., Gaudi, B.S., et al.: Astrophys. J. **720**, 1073 (2010)
Gradie, J., Tedesco, E.: Science **216**, 1405 (1982)
Greaves, J.S., Rice, W.K.M.: Monthly Not. Roy. Astron. Soc. **412**, L88 (2011)
Greenberg, R., Hartmann, W.K., Chapman, C.R., et al.: Icarus **35**, 1 (1978)
Gressel, O., Turner, N.J., Nelson, R.P., McNally, C.P.: Astrophys. J. **801**, 84 (2015)
Grimm, R.E., McSween, H.Y.: Science **259**, 653 (1993)
Gupta, A., Schlichting, H.E.: Monthly Not. Roy. Astron. Soc. **487**, 24 (2019)
Hahn, J.M.: The Dynamics of Planetary Systems and Astrophysical Disks. Wiley (2009)
Haisch, K.E., Jr., Lada, E.A., Lada, C.J.: Astrophys. J. Lett. **553**, L153 (2001)
Halliday, A.N.: Geochemica Cosmochemica Acta **105**, 146 (2013)
Halliday, A.N., Kleine, T.: In: Lauretta, D.S., McSween, H.Y. Jr. (eds.) Meteorites and the Early Solar System II, p. 775. University of Arizona Press, Tucson (2006)
Hansen, B.M.S.: Astrophys. J. **703**, 1131 (2009)
Hansen, B.M.S., Murray, N.: Astrophys. J. **751**, 158 (2012)
Hansen, B.M.S., Murray, N.: Astrophys. J. **775**, 53 (2013)
Hartmann, L., Calvet, N., Gullbring, E., D'Alessio, P.: Astrophys. J. **495**, 385 (1998)
Hartmann, W.K.: In: Lunar and Planetary Science Conference, Lunar and Planetary Science Conference, p. 1064 (2019)
Hartogh, P., Lis, D.C., Bockelée-Morvan, D., et al.: Nature **478**, 218 (2011)
Hasegawa, Y., Pudritz, R.E.: Astrophys. J. **760**, 117 (2012)
Hayashi, C.: Prog. Theor. Phys. Suppl. **70**, 35 (1981)
Helled, R., Bodenheimer, P., Podolak, M., et al.: In: Protostars and Planets VI, p. 643 (2014)
Henon, M., Heiles, C.: Astron. J. **69**, 73 (1964)
Hillenbrand, L.A., Carpenter, J.M., Kim, J.S., et al.: Astrophys. J. **677**, 630 (2008)
Hirschmann, M.M.: Annu. Rev. Earth Planet. Sci. **34**, 629 (2006)
Hollenbach, D., Johnstone, D., Lizano, S., Shu, F.: Astrophys. J. **428**, 654 (1994)
Howard, A.W., Marcy, G.W., Johnson, J.A., et al.: Science **330**, 653 (2010)
Howard, A.W., Marcy, G.W., Bryson, S.T., et al.: Astrophys. J. Suppl. Ser. **201**, 15 (2012)
Hu, X., Tan, J.C., Zhu, Z., et al.: Astrophys. J. **857**, 20 (2018)
Hu, X., Zhu, Z., Tan, J.C., Chatterjee, S.: Astrophys. J. **816**, 19 (2016)
Hubickyj, O., Bodenheimer, P., Lissauer, J.J.: Icarus **179**, 415 (2005)
Hughes, A.M., Duchêne, G., Matthews, B.C.: Annu. Revi. Astron. Astrophys. **56**, 541 (2018)
Ida, S., Lin, D.N.C.: Astrophys. J. **604**, 388 (2004)
Ida, S., Lin, D.N.C.: Astrophys. J. **673**, 487 (2008)
Ida, S., Lin, D.N.C.: Astrophys. J. **719**, 810 (2010)
Ida, S., Lin, D.N.C., Nagasawa, M.: Astrophys. J. **775**, 42 (2013)
Ida, S., Guillot, T., Morbidelli, A.: Astron. Astrophys. **591**, A72 (2016)
Ida, S., Guillot, T.: Astron. Astrophys. **596**, L3 (2016)
Ida, S., Yamamura, T., Okuzumi, S.: Astron. Astrophys. **624**, A28 (2019)
Ikoma, M., Genda, H.: Astrophys. J. **648**, 696 (2006)
Ikoma, M., Nakazawa, K., Emori, H.: Astrophys. J. **537**, 1013 (2000)
Inamdar, N.K., Schlichting, H.E.: Monthly Not. Roy. Astron. Soc. **448**, 1751 (2015)
Izidoro, A., Bitsch, B., Raymond, S.N., et al.: arXiv:1902.08772 (2019)
Izidoro, A., Morbidelli, A., Raymond, S.N.: Astrophys. J. **794**, 11 (2014)
Izidoro, A., Raymond, S.N., Morbidelli, A., et al.: Astrophys. J. Lett. **800**, L22 (2015a)
Izidoro, A., Morbidelli, A., Raymond, S.N., et al.: Astron. Astrophys. **582**, A99 (2015b)
Izidoro, A., Raymond, S.N., Morbidelli, A., Winter, O.C.: Monthly Not. Roy. Astron. Soc. **453**, 3619 (2015c)
Izidoro, A., Ogihara, M., Raymond, S.N., et al.: Monthly Not. Roy. Astron. Soc. **470**, 1750 (2017)
Jacobson, S.A., Morbidelli, A.: Philos. Trans. Roy. Soc. Lond. Ser. A **372**, 0174 (2014)
Jacobson, S.A., Morbidelli, A., Raymond, S.N., et al.: Nature, **508**, 84
Jacquet, E., Balbus, S., Latter, H.: Monthly Not. Roy. Astron. Soc. **415**, 3591 (2011)

Jin, S., Mordasini, C.: Astrophys. J. **853**, 163 (2018)
Johansen, A., Youdin, A., Klahr, H.: Astrophys. J. **697**, 1269 (2009)
Johansen, A., Davies, M.B., Church, R.P., Holmelin, V.: Astrophys. J. **758**, 39 (2012)
Johansen, A., Blum, J., Tanaka, H., et al.: Protostars and Planets VI, p. 547 (2014)
Johansen, A., Mac Low, M.M., Lacerda, P., Bizzarro, M.: Sci. Adv. **1**, 1500109 (2015)
Johansen, A., Lambrechts, M.: Ann. Rev. Earth Planet. Sci. **45**, 359 (2017)
Johnson, J.A., Butler, R.P., Marcy, G.W., et al.: Astrophys. J. **670**, 833 (2007)
Johnson, B.C., Walsh, K.J., Minton, D.A., et al.: Sci. Adv. **2**, e1601658 (2016)
Jones, H.R.A., Butler, R.P., Tinney, C.G., et al.: Monthly Not. Roy. Astron. Soc. **369**, 249 (2006)
Jurić, M., Tremaine, S.: Astrophys. J. **686**, 603 (2008)
Kaib, N.A., Chambers, J.E.: Monthly Not. Roy. Astron. Soc. **455**, 3561 (2016)
Kaib, N.A., Cowan, N.B.: Icarus **252**, 161 (2015)
Kaib, N.A., Raymond, S.N., Duncan, M.: Nature **493**, 381 (2013)
Kanagawa, K.D., Tanaka, H., Muto, T., et al.: Monthly Not. Roy. Astron. Soc. **448**, 994 (2015)
Kanagawa, K.D., Tanaka, H., Szuszkiewicz, E.: Astrophys. J. **861**, 140 (2018)
Kataoka, A., Tanaka, H., Okuzumi, S., Wada, K.: Astron. Astrophys. **557**, L4 (2013)
Kerridge, J.F.: Geochemica Cosmochemica Acta **49**, 1707 (1985)
Kimura, K., Lewis, R.S., Anders, E.: Geochemica Cosmochemica Acta **38**, 683 (1974)
Kimura, S.S., Tsuribe, T.: Proc. Astron. Soci. Jpn. **64**, 116 (2012)
Kita, N.T., Huss, G.R., Tachibana, S., et al.: Astron. Soc. Pac. Conf. Ser. **341**, 558 (2005)
Kleine, T., Touboul, M., Bourdon, B., et al.: Geochemica Cosmochemica Acta **73**, 5150 (2009)
Kokubo, E., Ida, S.: Icarus **123**, 180 (1996)
Kokubo, E., Ida, S.: Icarus **131**, 171 (1998)
Kokubo, E., Ida, S.: Icarus **143**, 15 (2000)
Kokubo, E., Ida, S.: Astrophys. J. **671**, 2082 (2007)
Kral, Q., Krivov, A.V., Defrère, D., et al.: Astron. Rev. **13**, 69 (2017)
Krasinsky, G.A., Pitjeva, E.V., Vasilyev, M.V., Yagudina, E.I.: Icarus **158**, 98 (2002)
Kretke, K.A., Lin, D.N.C.: Astrophys. J. **755**, 74 (2012)
Krivov, A.V.: Res. Astron. Astrophys. **10**, 383 (2010)
Krot, A.N., Amelin, Y., Cassen, P., Meibom, A.: Nature **436**, 989 (2005)
Kruijer, T.S., Burkhardt, C., Budde, C., Kleine, T.: PNAS **114**, 6712 (2017)
Kruijer, T.S., Touboul, M., Fischer-Gödde, M., et al.: Science **344**, 1150 (2014)
Kuchynka, P., Folkner, W.M.: Icarus **222**, 243 (2013)
Lambrechts, M., Johansen, A.: Astron. Astrophys. **544**, A32 (2012)
Lambrechts, M., Johansen, A.: Astron. Astrophys. **572**, A107 (2014)
Lambrechts, M., Johansen, A., Morbidelli, A.: Astron. Astrophys. **572**, A35 (2014)
Lambrechts, M., Lega, E.: Astron. Astrophys. **606**, A146 (2017)
Lambrechts, M., Morbidelli, A., Jacobson, S.A., et al.: Astron. Astrophys. **627**, A83 (2019a)
Lambrechts, M., Lega, E., Nelson, R.P., Crida, A., Morbidelli, A.: Astron. Astrophys. **630**, A82 (2019b)
Laplace, P.S.: 1822, Mécanique céleste
Laskar, J.: Astron. Astrophys. **317**, L75 (1997)
Laws, C., Gonzalez, G., Walker, K.M., et al.: Astron. J. **125**, 2664 (2003)
Lecar, M., Podolak, M., Sasselov, D., Chiang, E.: Astrophys. J. **640**, 1115 (2006)
Lee, M.H., Peale, S.J.: Astrophys. J. **567**, 596 (2002)
Lee, E.J., Chiang, E., Ormel, C.W.: Astrophys. J. **797**, 95 (2014)
Lee, E.J., Chiang, E.: Astrophys. J. **817**, 90 (2016)
Lee, E.J., Chiang, E.: Astrophys. J. **842**, 40 (2017)
Lega, E., Crida, A., Bitsch, B., Morbidelli, A.: Monthly Not. Roy. Astron. Soc. **440**, 683 (2014)
Lestrade, J.F., Matthews, B.C., Sibthorpe, B., et al.: Astron. Astrophys. **548**, A86 (2012)
Levison, H.F., Stewart, G.R.: Icarus **153**, 224 (2001)
Levison, H.F., Morbidelli, A., Vanlaerhoven, C., et al.: Icarus **196**, 258 (2008)
Levison, H.F., Thommes, E., Duncan, M.J.: Astron. J. **139**, 1297 (2010)

Levison, H.F., Morbidelli, A., Tsiganis, K., Nesvorný, D., Gomes, R.: Astron. J. **142**, 152 (2011)
Levison, H.F., Kretke, K.A., Walsh, K.J., Bottke, W.F.: Proc. Natl. Acad. Sci. **112**, 14180 (2015)
Lichtenberg, T., Golabek, G.J., Burn, R., et al.: Nat. Astron. **3**, 307 (2019)
Lin, D.N.C., Bodenheimer, P., Richardson, D.C.: Nature **380**, 606 (2019)
Lin, D.N.C., Ida, S.: Astrophys. J. **477**, 781 (1997)
Lin, D.N.C., Papaloizou, J.: Monthly Not. Roy. Astronom. Soc. **186**, 799 (1979)
Lin, D.N.C., Papaloizou, J.: Astrophys. J. **309**, 846 (1986)
Lis, D.C., Biver, N., Bockelée-Morvan, D., et al.: Astrophys. J. Lett. **774**, L3 (2013)
Lis, D.C., Bockelée-Morvan, D., Güsten, R., et al.: Astron. Astrophys. **625**, L5 (2019)
Lissauer, J.J.: Icarus **69**, 249 (1987)
Lissauer, J.J.: Annu. Rev. Astron. Astrophys. **31**, 129 (1993)
Lissauer, J.J., Hubickyj, O., D'Angelo, G., Bodenheimer, P.: Icarus **199**, 338 (2009)
Lissauer, J.J., Ragozzine, D., Fabrycky, D.C., et al.: Astrophys. J. Suppl. Ser. **197**, 8 (2011)
Lissauer, J.J., Stevenson, D.J. Protostars and Planets V, p. 591 (2007)
Lodders, K.: Astrophys. J. **591**, 1220 (2003)
Looney, L.W., Mundy, L.G., Welch, W.J.: Astrophys. J. **592**, 255 (2003)
Lopez, E.D.: Monthly Not. Roy. Astron. Soc. **472**, 245 (2017)
Lovis, C., Mayor, M.: Astron. Astrophys. **472**, 657 (2007)
Luger, R., Sestovic, M., Kruse, E., et al.: Nat. Astron. **1**, 0129 (2017)
Lykawka, P.S., Ito, T.: Astrophys. J. **883**, 130 (2019)
Lynden-Bell, D., Pringle, J.E.: Monthly Not. Roy. Astron. Soc. **168**, 603 (1974)
Lyra, W., Paardekooper, S.J., Mac Low, M.M.: Astrophys. J. Lett. **715**, L68 (2010)
Mamajek, E.E.: Am. Inst. Phys. Conf. Ser. **1158**, 3 (2009)
Manara, C.F., Morbidelli, A., Guillot, T.: Astron. Astrophys. **618**, L3 (2018)
Mandell, A.M., Raymond, S.N., Sigurdsson, S.: Astrophys. J. **660**, 823 (2007)
Marcy, G.W., Butler, R.P., Vogt, S.S., et al.: Astrophys. J. **555**, 418 (2011)
Marcy, G.W., Isaacson, H., Howard, A.W., et al.: Astrophys. J. Suppl. Ser. **210**, 20 (2014)
Marois, C., Macintosh, B., Barman, T., et al.: Science **322**, 1348 (2008)
Marois, C., Zuckerman, B., Konopacky, Q.M., Macintosh, B., Barman, T.: Nature **468**, 1080 (2010)
Marshall, J.P., Moro-Martín, A., Eiroa, C., et al.: Astron. Astrophys. **565**, A15 (2014)
Martin, R.G., Livio, M.: Monthly Not. Roy. Astron. Soc. **425**, L6 (2012)
Martin, R.G., Livio, M.: Astrophys. J. **810**, 105 (2015)
Marty, B.: Earth Planet. Sci. Lett. **313**, 56 (2012)
Marty, B., Altwegg, K., Balsiger, H., et al.: Science **356**, 1069 (2017)
Marty, B., Avice, G., Sano, Y., et al.: Earth Planet. Sci. Lett. **441**, 91 (2016)
Marty, B., Yokochi, R.: Rev. Mineral Geophys. **62**, 421 (2006)
Marzari, F.: Monthly Not. Roy. Astron. Soc. **444**, 1419 (2014)
Marzari, F., Weidenschilling, S.J.: Icarus **156**, 570 (2002)
Masset, F.S.: Monthly Not. Roy. Astron. Soc. **472**, 4204 (2017)
Masset, F.S., Snellgrove, M.: Monthly Not. Roy. Astron. Soc. **320**, L55 (2001)
Masset, F.S., Morbidelli, A., Crida, A., et al.: Astrophys. J. **642**, 478 (2006)
Matsumoto, Y., Nagasawa, M., Ida, S.: Icarus **221**, 624 (2012)
Matsumura, S., Ida, S., Nagasawa, M.: Astrophys. J. **767**, 129 (2013)
Matsumura, S., Thommes, E.W., Chatterjee, S., et al.: Astrophys. J. **714**, 194 (2010)
Matthews, B.C., Krivov, A.V., Wyatt, M.C., et al.: In: Beuther, H., Klessen, R.S., Dullemond, C.P., Henning, T. (eds.) Protostars and Planets VI, p. 521 (2014)
Mayer, L., Lufkin, G., Quinn, T., Wadsley, J.: Astrophys. J. Lett. **661**, L77 (2007)
Mayer, L., Quinn, T., Wadsley, J., Stadel, J.: Science **298**, 1756 (2002)
Mayor, M., Marmier, M., Lovis, C., et al.: arXiv:1109.2497 (2011)
McCubbin, F.M., Barnes, J.J.: Earth Planet. Sci. Lett. **526**, 115771 (2019)
McNally, C.P., Nelson, R.P., Paardekooper, S.J., Benítez-Llambay, P.: Monthly Not. Roy. Astron. Soc. **484**, 728 (2019)
McNeil, D.S., Nelson, R.P.: Monthly Not. Roy. Astron. Soc. **401**, 1691 (2010)

Meech, K., Raymond, S.N.: arXiv:1912.04361 (2019)
Meru, F., Bate, M.R.: Monthly Not. Roy. Astron. Soc. **410**, 559 (2011)
Meyer, M.R., Carpenter, J.M., Mamajek, E.E., et al.: Astrophys. J. Lett. **673**, L181 (2008)
Millholland, S., Wang, S., Laughlin, G.: Astrophys. J. Lett. **849**, L33 (2017)
Mills, S.M., Fabrycky, D.C., Migaszewski, C., et al.: Nature **533**, 509 (2016)
Moeckel, N., Throop, H.B.: Astrophys. J. **707**, 268 (2009)
Mojzsis, S.J., Brasser, R., Kelly, N.M., et al.: Astrophys. J. **881**, 44 (2019)
Montesinos, B., Eiroa, C., Krivov, A.V., et al.: Astron. Astrophys. **593**, A51 (2016)
Monteux, J., Golabek, G.J., Rubie, D.C., Tobie, G., Young, E.D.: Space Sci. Rev. **214**, 39 (2018)
Moorhead, A.V., Adams, F.C.: Icarus **178**, 517 (2005)
Morales, J.C., Mustill, A.J., Ribas, I., et al.: Science **365**, 1441 (2019)
Morbidelli, A., Bitsch, B., Crida, A., et al.: Icarus **267**, 368 (2016)
Morbidelli, A., Chambers, J., Lunine, J.I., et al.: Meteor. Planet. Sci. **35**, 1309 (2000)
Morbidelli, A., Levison, H.F., Tsiganis, K., Gomes, R.: Nature **435**, 462 (2005)
Morbidelli, A., Tsiganis, K., Crida, A., et al.: Astron. J. **134**, 1790 (2007)
Morbidelli, A., Nesvorny, D.: Astron. Astrophys. **546**, A18 (2012)
Morbidelli, A., Lambrechts, M., Jacobson, S., Bitsch, B.: Icarus **258**, 418 (2015)
Morbidelli, A., Nesvorny, D., Laurenz, V., et al.: Icarus **305**, 262 (2018)
Morbidelli, A., Raymond, S.N.: J. Geophys. Res. (Planets) **121**, 1962 (2016)
Morbidelli, A., Wood, B.J.: Washington DC Am. Geophys. Union Geophys. Monogr. Ser. **212**, 71 (2015)
Mordasini, C., Alibert, Y., Benz, W.: Astron. Astrophys. **501**, 1139 (2009)
Mori, S., Bai, X.N., Okuzumi, S.: Astrophys. J. **872**, 98 (2019)
Moriarty, J., Ballard, S.: Astrophys. J. **832**, 34 (2016)
Morishima, R., Schmidt, M.W., Stadel, J., Moore, B.: Astrophys. J. **685**, 1247 (2008)
Morishima, R., Stadel, J., Moore, B.: Icarus **207**, 517 (2010)
Moro-Martín, A., Carpenter, J.M., Meyer, M.R., et al.: Astrophys. J. **658**, 1312 (2007)
Moro-Martín, A., Marshall, J.P., Kennedy, G., et al.: Astrophys. J. **801**, 143 (2015)
Mottl, M., Glazer, B., Kaiser, R., Meech, K.: Chemie der Erde / Geochemistry **67**, 253 (2007)
Mukhopadhyay, S.: Nature **486**, 101 (2012)
Mulders, G.D., Mordasini, C., Pascucci, I., Ciesla, F.J., Emsenhuber, A., Apai, D.: Astrophys. J., **887**, 2 (2019)
Mulders, G.D., Pascucci, I., Apai, D., Ciesla, F.J.: Astron. J. **156**, 24 (2018)
Mundy, L.G., Looney, L.W., Welch, W.J.: Protostars and Planets IV, p. 355 (2000)
Muralidharan, K., Deymier, P., Stimpfl, M., et al.: Icarus **198**, 400 (2008)
Nagasawa, M., Lin, D.N.C., Thommes, E.: Astrophys. J. **635**, 578 (2005)
Nagasawa, M., Ida, S., Bessho, T.: Astrophys. J. **678**, 498 (2008)
Nayakshin, S.: Monthly Not. Roy. Astron. Soc. **454**, 64 (2015)
Ndugu, N., Bitsch, B., Jurua, E.: Monthly Not. Roy. Astron. Soc. **474**, 886 (2018)
Neishtadt, A.: J. App. Math. Mech. **48**, 133 (1984)
Nesvorný, D.: Astron. J. **150**, 73 (2015)
Nesvorný, D., Morbidelli, A.: Astron. J. **144**, 117 (2012)
Nesvorný, D., Youdin, A.N., Richardson, D.C.: Astron. J. **140**, 785 (2010)
Nesvorný, D., Vokrouhlický, D., Morbidelli, A.: Astrophys. J. **768**, 45 (2013)
Nesvorný, D., Vokrouhlický, D., Deienno, R.: Astrophys. J. **784**, 22 (2014)
Nesvorný, D., Vokrouhlický, D., Bottke, W.F., Levison, H.F.: Nat. Astron. **2**, 878 (2018)
Nesvorný, D.: Annu. Rev. Astron. Astrophys. **56**, 137 (2018)
Nesvorný, D., Li, R., Youdin, A.N., et al.: Nat. Astron. **3**, 808 (2019)
Nimmo, F., Kleine, T.: Icarus **191**, 497 (2007)
Noll, K.S., Grundy, W.M., Chiang, E.I., et al.: In: Barucci, M.A., Boehnhardt, H., Cruikshank, D.P., Morbidelli, A. (eds.) The Solar System Beyond Neptune, vol. 592, p. 345. University of Arizona Press, Tucson
Nomura, R., Hirose, K., Uesegi, K., et al.: Science **343**, 522 (2014)

Nyquist, L.E., Kleine, T., Shih, C.Y., Reese, Y.D.: Geochemica Cosmochemica Acta **73**, 5115 (2009)
O'Brien, D.P., Morbidelli, A., Levison, H.F.: Icarus **184**, 39 (2006)
O'Brien, D.P., Walsh, K.J., Morbidelli, A., et al.: Icarus **239**, 74 (2014)
O'Brien, D.P., Izidoro, A., Jacobson, S.A., et al.: Space Sci. Rev. **214**, 47 (2018)
Ogihara, M., Ida, S.: Astrophys. J. **699**, 824 (2009)
Ogihara, M., Morbidelli, A., Guillot, T.: Astron. Astrophys. **578**, A36 (2015)
Ogihara, M., Kokubo, E., Suzuki, T.K., Morbidelli, A.: Astron. Astrophys. **612**, L5 (2018a)
Ogihara, M., Kokubo, E., Suzuki, T.K., Morbidelli, A.: Astron. Astrophys. **615**, A63 (2018b)
Oka, A., Nakamoto, T., Ida, S.: Astrophys. J. **738**, 141 (2011)
Okuzumi, S., Tanaka, H., Kobayashi, H., Wada, K.: Astrophys. J. **752**, 106 (2012)
Ormel, C.W., Klahr, H.H.: Astron. Astrophys. **520**, A43 (2010)
Owen, J.E., Ercolano, B., Clarke, C.J.: Monthly Not. Roy. Astron. Soc. **412**, 13 (2011)
Owen, J.E., Wu, Y.: Astrophys. J. **775**, 105 (2013)
Owen, J.E., Wu, Y.: Astrophys. J. **847**, 29 (2017)
Paardekooper, S.J.: Monthly Not. Roy. Astron. Soc. **444**, 2031 (2014)
Paardekooper, S.J., Baruteau, C., Crida, A., Kley, W.: Monthly Not. Roy. Astron. Soc. **401**, 1950 (2010)
Paardekooper, S.J., Baruteau, C., Kley, W.: Monthly Not. Roy. Astron. Soc. **410**, 293 (2011)
Paardekooper, S.J., Mellema, G.: Astron. Astrophys. **459**, L17 (2006)
Pätzold, M., Andert, T.P., Hahn, M., et al.: Monthly Not. Roy. Astron. Soc. **483**, 2337 (2019)
Petigura, E.A., Howard, A.W., Marcy, G.W.: Proc. Natl. Acad. Sci. **110**, 19273 (2013)
Pfalzner, S., Steinhausen, M., Menten, K.: Astrophys. J. Lett. **793**, L34 (2014)
Pichierri, G., Morbidelli, A., Crida, A.: Celest. Mech. Dyn. Astron. **130**, 54 (2018)
Pierens, A.: Monthly Not. Roy. Astron. Soc. **454**, 2003 (2015)
Pierens, A., Nelson, R.P.: Astron. Astrophys. **482**, 333 (2008)
Pierens, A., Raymond, S.N.: Astron. Astrophys. **533**, A131 (2011)
Pierens, A., Raymond, S.N.: Monthly Not. Roy. Astron. Soc. **462**, 4130 (2016)
Pierens, A., Raymond, S.N., Nesvorny, D., Morbidelli, A.: Astrophys. J. Lett. **795**, L11 (2014)
Pinte, C., Dent, W.R.F., Ménard, F., et al.: Astrophys. J. **816**, 25 (2016)
Pirani, S., Johansen, A., Bitsch, B., et al.: Astron. Astrophys. **623**, A169 (2019)
Piso, A.M.A., Youdin, A.N.: Astrophys. J. **786**, 21 (2014)
Poincaré, H.: Les methodes nouvelles de la mecanique celeste (1892)
Poincaré, H.: Bulletin Astronomique. Serie I **14**, 53 (1897)
Pollack, J.B., Hubickyj, O., Bodenheimer, P., et al.: Icarus **124**, 62 (1996)
Quarles, B., Kaib, N.: Astron. J. **157**, 67 (2019)
Quintana, E.V., Barclay, T., Borucki, W.J., et al.: Astrophys. J. **821**, 126 (2016)
Quintana, E.V., Barclay, T., Raymond, S.N., et al.: Science **344**, 277 (2014)
Rafikov, R.R.: Astron. J. **128**, 1348 (2004)
Rasio, F.A., Ford, E.B.: Science **274**, 954 (1996)
Raymond, S.N., Quinn, T., Lunine, J.I.: Icarus **168**, 1 (2004)
Raymond, S.N., Quinn, T., Lunine, J.I.: Icarus **183**, 265 (2006a)
Raymond, S.N., Mandell, A.M., Sigurdsson, S.: Science **313**, 1413 (2006b)
Raymond, S.N., Quinn, T., Lunine, J.I.: Astrobiology **7**, 66 (2007a)
Raymond, S.N., Scalo, J., Meadows, V.S.: Astrophys. J. **669**, 606 (2007b)
Raymond, S.N., Barnes, R., Mandell, A.M.: Monthly Not. Roy. Astron. Soc. **384**, 663 (2008a)
Raymond, S.N., Barnes, R., Armitage, P.J., Gorelick, N.: Astrophys. J. Lett. **687**, L107 (2008b)
Raymond, S.N., Barnes, R., Veras, D., et al.: Astrophys. J. Lett. **696**, L98 (2009a)
Raymond, S.N., O'Brien, D.P., Morbidelli, A., Kaib, N.A.: Icarus **203**, 644 (2009b)
Raymond, S.N., Armitage, P.J., Gorelick, N.: Astrophys. J. **711**, 772 (2010)
Raymond, S.N., Armitage, P.J., Moro-Martín, A., et al.: Astron. Astrophys. **530**, A62 (2011)
Raymond, S.N., Armitage, P.J., Moro-Martín, A., et al.: Astron. Astrophys. **541**, A11 (2012)
Raymond, S.N., Schlichting, H.E., Hersant, F., Selsis, F.: Icarus **226**, 671 (2013)

Raymond, S.N., Kokubo, E., Morbidelli, A., et al.: Protostars and Planets VI, p. 595 (2014)
Raymond, S.N., Cossou, C.: Monthly Not. Roy. Astron. Soc. **440**, L11 (2014)
Raymond, S.N., Morbidelli, A.: In: Complex Planetary Systems, Proceedings of the International Astronomical Union, IAU Symposium, vol. 310, p. 194 (2014)
Raymond, S.N., Izidoro, A.: Icarus **297**, 134 (2017a)
Raymond, S.N., Izidoro, A.: Sci. Adv. **3**, e1701138 (2017b)
Raymond, S.N., Armitage, P.J., Veras, D., et al.: Monthly Not. Roy. Astron. Soc. **476**, 3031 (2018a)
Raymond, S.N., Boulet, T., Izidoro, A., et al.: Monthly Not. Roy. Astron. Soc. **479**, L81 (2018b)
Raymond, S.N., Armitage, P.J., Veras, D.: Astrophys. J. Lett. **856**, L7 (2018c)
Raymond, S.N., Izidoro, A., Morbidelli, A.: arXiv:1812.01033 (2018d)
Ribas, I., Miralda-Escudé, J.: Astron. Astrophys. **464**, 779 (2007)
Rivera, E.J., Laughlin, G., Butler, R.P., et al.: Astrophys. J. **719**, 890 (2010)
Robert, F., Merlivat, L., Javoy, M.: Meteoritics **12**, 349 (1977)
Robert, C.M.T., Crida, A., Lega, E.: Astron. Astrophys. **617**, A98
Rogers, L.A.: Astrophys. J. **801**, 41 (2015)
Ronnet, T., Mousis, O., Vernazza, P., et al.: Astron. J. **155**, 224 (2018)
Rowan, D., Meschiari, S., Laughlin, G., et al.: Astrophys. J. **817**, 104 (2016)
Rowe, J.F., Bryson, S.T., Marcy, G.W., et al.: Astrophys. J. **784**, 45 (2014)
Rubie, D.C., Jacobson, S.A., Morbidelli, A., et al.: Icarus **248**, 89 (2015)
Safronov, V.S.: Evolution of the Protoplanetary Cloud and Formation of the Earth and Planets. Keter Publishing House (1972)
Santos, N.C., Israelian, G., Mayor, M.: Astron. Astrophys. **373**, 1019 (2001)
Sasselov, D.D., Lecar, M.: Astrophys. J. **528**, 995 (2000)
Sato, T., Okuzumi, S., Ida, S.: Astron. Astrophys. **589**, A15 (2016)
Schäfer, U., Yang, C.C., Johansen, A.: Astron. Astrophys. **597**, A69 (2017)
Schiller, M., Bizzarro, M., Fernandes, V.A.: Nature **555**, 507 (2018)
Schiller, M., Connelly, J.N., Glad, A.C., et al.: Earth Planet. Sci. Lett. **420**, 45 (2015)
Schlichting, H.E.: Astrophys. J. Lett. **795**, L15 (2014)
Schoonenberg, D., Ormel, C.W.: Astron. Astrophys. **602**, A21 (2017)
Seager, S., Kuchner, M., Hier-Majumder, C.A., Militzer, B.: Astrophys. J. **669**, 1279 (2007)
Selsis, F., Chazelas, B., Bordé, P., et al.: Icarus **191**, 453 (2007)
Sessin, W., Ferraz-Mello, S.: Celest. Mech. **32**, 307 (1984)
Shakura, N.I., Sunyaev, R.A.: Astron. Astrophys. **24**, 337 (1973)
Sharp, Z.D.: Chem. Geol. **448**, 137 (2017)
Simon, J.B., Armitage, P.J., Li, R., Youdin, A.N.: Astrophys. J. **822**, 55 (2016)
Simon, J.B., Armitage, P.J., Youdin, A.N., Li, R.: Astrophys. J. Lett. **847**, L12 (2017)
Sinukoff, E., Howard, A.W., Petigura, E.A., et al.: Astron. J. **153**, 70 (2017)
Snellgrove, M.D., Papaloizou, J.C.B., Nelson, R.P.: Astron. Astrophys. **374**, 1092 (2001)
Sosa, A., Fernández, J.A.: Monthly Not. Roy. Astron. Soc. **416**, 767 (2011)
Sotin, C., Grasset, O., Mocquet, A.: Icarus **191**, 337 (2007)
Stimpfl, M., Walker, A.M., Drake, M.J., et al.: J. Crystal Growth **294**, 83 (2006)
Stone, J.M., Ostriker, E.C., Gammie, C.F.: Astrophys. J. Lett. **508**, L99 (1998)
Su, K.Y.L., Rieke, G.H., Stansberry, J.A., et al.: Astrophys. J. **653**, 675 (2006)
Suzuki, T.K., Ogihara, M., Morbidelli, A., et al.: Astron. Astrophys. **596**, A74 (2016a)
Suzuki, D., Bennett, D.P., Sumi, T., et al.: Astrophys. J. **833**, 145 (2016b)
Svetsov, V.V.: Solar Syst. Res. **41**, 28 (2007)
Tanaka, H., Takeuchi, T., Ward, W.R.: Astrophys. J. **565**, 1257 (2002)
Tanaka, H., Ward, W.R.: Astrophys. J. **602**, 388 (2004)
Tera, F., Papanastassiou, D.A., Wasserburg, G.J.: Earth Planet. Sci. Lett. **22**, 1 (1974)
Terquem, C., Papaloizou, J.C.B.: Astrophys. J. **654**, 1110 (2007)
Thommes, E.W., Duncan, M.J., Levison, H.F.: Icarus **161**, 431 (2003)
Thommes, E.W., Matsumura, S., Rasio, F.A.: Science **321**, 814 (2008)
Throop, H.B., Bally, J.: Astron. J. **135**, 2380 (2008)

Tominaga, R.T., Takahashi, S.Z., Inutsuka, S.I.: Astrophys. J. **881**, 53 (2019)
Toomre, A.: Astrophys. J. **139**, 1217 (1964)
Touboul, M., Kleine, T., Bourdon, B., et al.: Nature **450**, 1206 (2007)
Tremaine, S., Dong, S.: Astron. J. **143**, 94 (2012)
Trilling, D.E., Bryden, G., Beichman, C.A., et al.: Astrophys. J. **674**, 1086 (2008)
Tsiganis, K., Gomes, R., Morbidelli, A., Levison, H.F.: Nature **435**, 459 (2005)
Turner, N.J., Fromang, S., Gammie, C., et al.: Protostars and Planets VI, p. 411 (2014)
Udry, S., Bonfils, X., Delfosse, X., et al.: Astron. Astrophys. **469**, L43 (2007)
Udry, S., Santos, N.C.: Annu. Rev. Astron. Astrophys. **45**, 397 (2007)
Uribe, A.L., Klahr, H., Henning, T.: Astrophys. J. **769**, 97 (2013)
Valencia, D., Sasselov, D.D., O'Connell, R.J.: Astrophys. J. **665**, 1413 (2007)
Varnière, P., Quillen, A.C., Frank, A.: Astrophys. J. **612**, 1152 (2004)
Veras, D., Armitage, P.J.: Astrophys. J. Lett. **620**, L111 (2005)
Veras, D., Armitage, P.J.: Astrophys. J. **645**, 1509 (2006)
Villeneuve, J., Chaussidon, M., Libourel, G.: Science **325**, 985 (2009)
Walsh, K.J., Morbidelli, A., Raymond, S.N., et al.: Nature **475**, 206 (2011)
Walsh, K.J., Morbidelli, A., Raymond, S.N., et al.: Meteor. Planet. Sci. **47**, 1941 (2012)
Ward, W.R.: Icarus **67**, 164 (1986)
Ward, W.R.: Icarus **126**, 261 (1997)
Warren, P.H.: Earth Planet. Sci. Lett. **311**, 93 (2011)
Weber, P., Benítez-Llambay, P., Gressel, O., et al.: Astrophys. J. **854**, 153 (2018)
Weidenschilling, S.J.: Astrophys. Space Sci. **51**, 153 (1977a)
Weidenschilling, S.J.: Monthly Not. Roy. Astron. Soc. **180**, 57 (1977b)
Weidenschilling, S.J., Marzari, F.: Nature **384**, 619 (1996)
Weiss, L.M., Marcy, G.W.: Astrophys. J. Lett. **783**, L6 (2014)
Weiss, L.M., Marcy, G.W., Petigura, E.A., et al.: Astron. J. **155**, 48 (2018)
Weiss, L.M., Marcy, G.W., Rowe, J.F., et al.: Astrophys. J. **768**, 14 (2013)
Wetherill, G.W.: In: Gehrels, T. (ed.) IAU Colloq. 52: Protostars and Planets, p. 565 (1978)
Wetherill, G.W.: In: Lunar and Planetary Institute Science Conference Abstracts, Lunar and Planetary Inst. Technical Report, vol. 22, p. 1495 (1991)
Wetherill, G.W.: Icarus **100**, 307 (1992)
Wetherill, G.W.: Icarus **119**, 219 (1996)
Wetherill, G.W., Stewart, G.R.: Icarus **77**, 330 (1989)
Wetherill, G.W., Stewart, G.R.: Icarus **106**, 190 (1993)
Williams, J.P., Cieza, L.A.: Annu. Rev. Astron. Astrophys. **49**, 67 (2011)
Windmark, F., Birnstiel, T., Güttler, C., et al.: Astrono. Astrophy. **540**, A73 (2012)
Winn, J.N., Fabrycky, D.C.: Annu. Rev. Astron. Astrophys. **53**, 409
Wittenmyer, R.A., Butler, R.P., Tinney, C.G., et al.: Astrophys. J. **819**, 28 (2016)
Wittenmyer, R.A., Wang, S., Horner, J., et al.: Monthly Not. Roy. Astron. Soc. **492**, 377 (2020)
Wolfgang, A., Rogers, L.A., Ford, E.B.: Astrophys. J. **825**, 19 (2016)
Wright, J.T., Marcy, G.W., Butler, R.P., et al.: Astrophys. J. Lett. **683**, L63 (2008)
Wright, J.T., Upadhyay, S., Marcy, G.W., et al.: Astrophys. J. **693**, 1084 (2009)
Wright, J.T., Fakhouri, O., Marcy, G.W., et al.: Proc. Astron. Soc. Pac. **123**, 412 (2011)
Wyatt, M.C.: Annu. Rev. Astron. Astrophys. **46**, 339 (2008)
Wyatt, M.C., Kennedy, G., Sibthorpe, B., et al.: Monthly Not. Roy. Astron. Soc. **424**, 1206 (2012)
Yang, C.C., Johansen, A., Carrera, D.: Astron. Astrophys. **606**, A80 (2017)
Youdin, A.N., Goodman, J.: Astrophys. J. **620**, 459 (2005)
Zellner, N.E.B.: Origins Life Evol. Biosphere **47**, 261 (2017)
Zhang, H., Zhou, J.L.: Astrophys. J. **714**, 532 (2010)
Zhang, Q.: Astrophys. J. Lett. **852**, L13 (2018)
Zhou, J.L., Aarseth, S.J., Lin, D.N.C., Nagasawa, M.: Astrophys. J. Lett. **631**, L85 (2005)
Zhu, W., Wu, Y.: Astrophys. J. **156**, 92 (2018)
Zube, N.G., Nimmo, F., Fischer, R.A., Jacobson, S.A.: Earth Planet. Sci. Lett. **522**, 210 (2019)